Structural and Spectroscopical Study of Crystals of 1,3,4-Oxadiazole Derivatives at High Pressure

D I S S E R T A T I O N

zur Erlangung des akademischen Grades
Doctor rerum naturalium
(Dr. rer. nat.)
in der Wissenschaftsdisziplin Festkörperphysik

eingereicht an der
Mathematisch-Naturwissenschaftlichen Fakultät
Universität Potsdam

von
Frau Dipl.-Phys. Olga Franco González
geboren am 21.12.1973 in Valladolid (Spanien)

Gutachter:

1. Prof. Dr. L. Brehmer
2. Prof. Dr. U. Pietsch
3. Prof. Dr. J.A. de Saja

eingereicht am: 15. April 2002
Tag der mündlichen Prüfung: 25. Juli 2002

Acknowledgements

I wish to express my gratitude to Dr. habil. B. Schulz for proposing the interesting topic of this thesis and for the numerous fruitful discussions which guided me during the course of my work.

For giving me the possibility to realize this doctoral thesis at the Dept. of Condensed Matter Physics I am indebted to Prof. L. Brehmer.

Very special thanks are directed to Dr. I. Orgzall for the close collaboration we have kept throughout my stay in Potsdam. His contribution to the outcome of the present investigation has been in many respects vital.

Prof. U. Pietsch and Dr. J. Grenzer of the Dept. of Structural Analysis gave me the opportunity to carry out the X-ray experiments under heating. J. Grenzer's generous availability is thankfully acknowledged.

I would like to thank Dr. W. Regenstein for his kind collaboration in the UV-Vis studies.

Thanks are due to Dr. C. Lathe for the technical support during our high pressure X-ray experiments at HASYLAB (DESY).

Dr. S. Stockhause contributed to the discussion of the investigated crystal structures.

I acknowledge the continued inspiration from Prof. J.A. de Saja (Dept. of Condensed Matter Physics at the University of Valladolid, Spain) during these past years.

The entire staff of the Institute of Condensed Matter Physics provided helpful services and a productive atmosphere.

Finally, I would like to thank Dr. M. Uhlmann for his help in preparing this manuscript.

Contents

Nomenclature

Abbreviation	Meaning	Page
1DPO1	2,5-di(4-nitrophenyl)-1,3,4-oxadiazole	
3DPO3	2,5-di-(4-tolyl)-1,3,4-oxadiazole	
5DPO5	2,5-di-(4-methoxycarbonylphenyl)-1,3,4-oxadiazole	
6DPO6	2,5-di-(4-aminophenyl)-1,3,4-oxadiazole	
6DPO4	2-(4-aminophenyl)-5-(4-methoxyphenyl)-1,3,4-oxadiazole	
7DPO7	2,5-di-(4-dimethylaminophenyl)-1,3,4-oxadiazole	
7PO3	4-(5-methyl-1,3,4-oxadiazole-2yl-)-N,N'-dimethyl-phenylamine	
DPO	2,5-diphenyl-1,3,4-oxadiazole	
DAC	diamond anvil cell	6
DSC	differential scanning calorimetry	9
MEOS	Murnaghan equation of state	26
S_0	electronic ground state (singlet)	57
S_1	electronic first excited state (singlet)	57
TGA	thermo-gravimetric analysis	9

Please note that all substances, except 7PO3, are derivatives of DPO. The nomenclature xDPOy stands for the para-substituted DPO derivative with the substituents R_1=x and R_2=y (cf. fig. 1). The same philosophy was applied for 7PO3. Here PO means that one of the phenyl rings of DPO is missing. The substituents are numbered as follows:

1	NO_2
2	H
3	CH_3
4	OCH_3
5	$COOCH_3$
6	NH_2
7	$N(CH_3)_2$

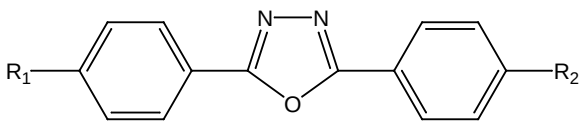

Fig. 1: DPO derivatives.

Symbol	Meaning	Page
α	coefficient of thermal expansion	49
β	monoclinic angle	24
γ_D	Debye-Grüneisen parameter	91
γ_i	mode Grüneisen parameter	91
ΔW	interaction energy	62
ε	dielectric constant	113
θ	diffraction angle	3
θ_D	Debye temperature	89
λ	wavelength	3
a	parameter in Debye's model	88
a, b, c	lattice parameters	13
B	one half of the Davidov splitting factor for crystals with two molecules in the unit cell	62
C	shift due to the interactions with translationally equivalent molecules	62
d	molar density of vibrational states	88
E_{vib}	energy due to the vibration of the crystal	89
E_0	cohesive energy at 0 K	89
E_{e^-}	energy of the electronic gas	89
E_c	energy of an excited state of a crystal	62
E_0	energy of an excited isolated molecule	62
$f(k)$	density of vibrational states	88
F	Helmholtz potential	26
$g(w)$	density of states	88
G	Gibbs potential	26
h	Planck's constant ($h = 2\pi/\hbar$)	4,62,88
$\mathbf{k}$	wave vector	87
K_0	zero-pressure bulk modulus	26
K_B	Boltzmann's constant	88
K_T, K	isothermal bulk modulus	26
N	number of particles of a system	26
N_A	Avogadro's number	88
p	pressure	26,89
p_0	static pressure	90
p_{th}	thermal pressure	90
S	entropy	90
S	solvent shift	62
T	temperature	26
$\mathbf{u}(\mathbf{x}, t)$	vibrational displacement	87
v	group velocity	87
V	volume	26,88
V_L	volume of the real unit cell	88
V_R	volume of the reciprocal unit cell (Brillouin zone)	88
w	frequency of vibration	87
w_D	cutoff frequency	88
$\mathbf{x}$	spatial coordinate vector	87

Chapter 1

Introduction

In recent years the search for new materials of technological interest has given new impulses to the study of organic compounds. Organic substances possess a great number of advantages such as the possibility to adjust their properties for a given purpose by different chemical and physical techniques in the preparation process. One such example is the 1,3,4-oxadiazole ring. 1,3,4-oxadiazole compounds are thermally stable, hetero-aromatic molecules. They are used as chromophores, as material for light emitting diodes (LED) as well as scintillators [1, 2, 3, 4, 5, 6, 7, 8, 9]. This is due to their promising characteristics as UV and blue emitters [2, 4, 10, 11, 12, 13, 14, 15, 16], and as electron-injection layers [17, 18, 19, 20]. In addition, oxadiazole compounds are able to build thin films which is of crucial importance for applications in LEDs. Thin films of these compounds can be obtained by different methods: Langmuir-Blodgett, molecular beam deposition, spin coating, self assembly, etc. [9, 21, 22, 23, 24, 25, 26, 27, 28]. They also have applications in medicine and agriculture [29, 30]. Furthermore, 1,3,4-oxadiazoles have attractive liquid crystalline properties. A very broad application spectrum is well known for the polymeric form of 1,3,4-oxadiazole, based on its high thermal stability in oxidative atmosphere [9, 28, 31, 32, 33]. Other properties to be mentioned are good hydrolytic stability, high glass transition temperatures, low dielectric constants and tough mechanical properties.

Pressure is a thermodynamic variable which is as fundamental as temperature. The application of pressure to a substance is an excellent way to study the dependence of its properties upon the molecular and super-molecular arrangements without introducing chemical changes in the system. Nevertheless, up to recent years pressure was scarcely used in material science in comparison with temperature. This has its origin in the technological difficulties which are encountered when performing experiments under compression. In the last decades, with the development of the diamond anvil cell and the synchrotron sources, great progress has been made in the investigation of matter under compression [34].

The application of high pressure to a solid modifies the inter-atomic distances. This results in a change of its properties. Thus, the controlled variation of the applied pressure may serve to tune the properties of the material. High pressure phases of known materials may have completely new properties, in such a way that one could speak of new materials. A typical example, which in fact is of technological interest in its own right, is the transition of insulators into conductors or even into super-conductors under compression [35]. Probably the most interesting substances, from the technological point of view, which are obtained by means of high pressure are the super-hard materials diamond and cubic boron nitride. Additionally, pressure is a parameter which can strongly influence the course of a chemical reaction. In recent years it was used as a tool for the synthesis of meta-stable phases and of completely new compounds [36, 37, 38, 39, 40, 41].

Amongst the various solid state forms (e.g. amorphous, thin film, crystalline), we chose to investigate the crystalline one because it is the only one in which both molecular and super-molecular arrangement can be accurately determined—at least at normal conditions. For the

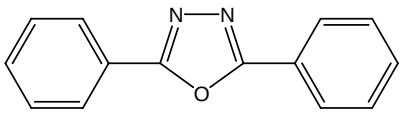

Fig. 1.1: Chemical structure of DPO.

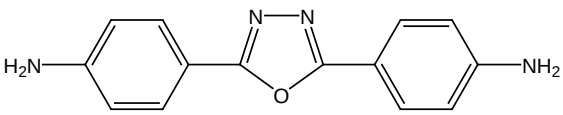

Fig. 1.2: Chemical structure of 6DPO6.

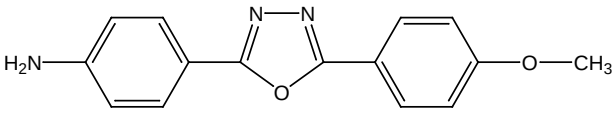

Fig. 1.3: Chemical structure of 6DPO4.

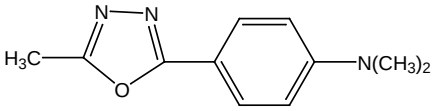

Fig. 1.4: Chemical structure of 7PO3.

present work we chose four 1,3,4-oxadiazole compounds with different molecular structure.

(i) DPO: It constitutes the basic unit for most of the other compounds. The phenyl rings are not substituted.

(ii) 6DPO6: It is a symmetrically substituted DPO derivative. Each phenylene ring is substituted by a NH_2 group in para position.

(iii) 6DPO4: This compound is an asymmetrically substituted DPO derivative. One phenylene ring is substituted by a NH_2 group, as in 6DPO6, and the other phenylene ring is substituted by a OCH_3 group both in para position.

(iv) 7PO3: This compound only contains one phenylene ring. It is therefore a two ring system while the other investigated compounds are three ring systems. The presence of only one phenylene ring causes an asymmetrical electron density which makes this molecule different from the rest.

The present work has a double objective. On the one hand, to systematically study for the first time the compression behaviour of the above mentioned oxadiazole compounds in crystalline state, i.e. to characterize the structural evolution of the crystals. On the other hand, to investigate the response to pressure of the spectroscopical properties of these substances. Both objectives are inter-related. In order to understand the evolution of the properties under compression it is fundamental to know how the molecular and super-molecular arrangement varies under compression. Conversely, the study of the evolution of the spectroscopical characteristics under compression may give information about the compression process.

The outline of this thesis is as follows. After a description of the employed experimental procedures, we begin our investigation with the study of the crystal structure of the materials at normal conditions (§3). This way, information about the inter-molecular interactions which hold the crystal together is gained. Such a knowledge is of major importance for the subsequent investigation. The behaviour of the crystal structure under compression and under heating is the subject of the following chapters (§4 and §5). As we will see, it is directly related to the inter-molecular interactions within the crystal. From the combination of the response of the volume of the crystal to pressure and to temperature, an empirical equation of state for the system can be determined. Once we have determined how the *structure* of the crystal varies under compression, the effect of compression upon the *absorption* and *emission* features is studied (§6 and §7). Finally, we investigate the *Raman spectrum* of the crystals at ambient and high pressure (§8). From these experiments an important contribution to a complete equation of state can be made.

Chapter 2

Experimental setup

2.1 Materials

All the substances (except one sample of 6DPO6, supplied by Aldrich) were provided by B. Schulz (IFZ DOBS, University of Potsdam). The oxadiazole compounds were synthesized following the usual procedures described in the literature [42, 43, 44, 45] and twice recrystallized from the solution. After the recrystallization, the crystals were dried in a vacuum chamber.

2.2 Structural studies

2.2.1 Structural studies at normal conditions

The structure analysis was carried out by G. Reck and S. Stockhause in the frame of the present work [45, 46, 47, 48, 49, 50]. Only the structure of one of the materials studied here, DPO I, was already known from the literature [51] and could be confirmed by our investigations.

The crystal structures were determined using single crystal techniques. The X-ray data collection was carried out on a Bruker AXS smart/CCD diffractometer at 293 K using Mo K_α radiation (λ=0.7103 Å) monochromatized by a graphite crystal. Data were collected employing the ω-scan technique generally in the range $4° < 2\theta < 47°$. The structures were solved by direct methods and refined by full-matrix least squares calculations using SHELXTL [52]. All H atoms could be located by Fourier synthesis.

2.2.2 Structural studies under compression

All X-ray investigations under compression and under heating were performed applying powder techniques. The high pressure structural investigations were carried out using the multi-anvil high pressure device MAX-80 [53] in connection with the high energy synchrotron radiation source of the HASYLAB facilities at DESY, Hamburg. A scheme of the anvils is shown in fig. 2.1. For the acquisition of the X-ray diffraction patterns we use the energy dispersive technique in the energy range up to 70 keV. The beam size was around 1 mm in diameter. The spectra were recorded with a Ge detector connected to a multi-channel analyser. All patterns were collected for approximately 5 min. However, the intensity of the peaks was influenced by experimental limitations. For instance, the intensity of the synchrotron light is not constant with time and the spectrum of the so called *white* X-rays is indeed not perfectly homogeneous due to the different energy-dependent absorbances of the materials the light passes through. Additionally, texture influences especially due to the needle-like morphology of most of the oxadiazole crystals have to

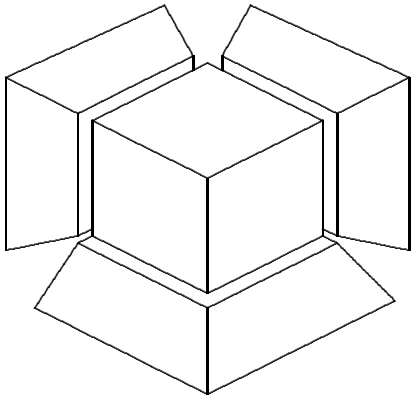

Fig. 2.1: Principal setup of the high pressure device MAX-80. Only three of the six anvils are shown.

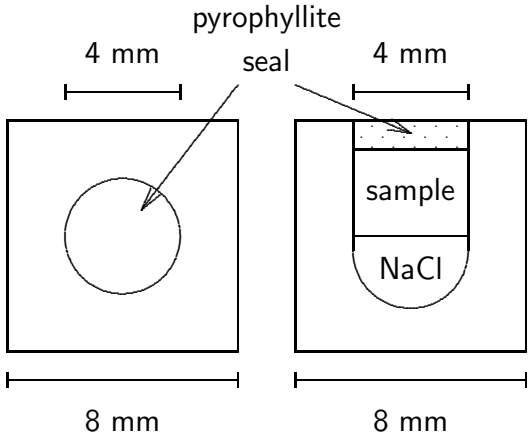

Fig. 2.2: Frontal and lateral view of the epoxy cube with sample and pressure marker (NaCl).

be taken into account. Figure 2.3 compares two powder X-ray diffraction patterns of one of the substances, one acquired using angle dispersive technique and another using the energy dispersive equipment. It can be seen that the energy dispersive technique lacks in high resolution which reduces somewhat the quality of the diffractograms.

The sample, in the form of powder, was introduced into an epoxy cube which serves as gasketing and pressure transmitting material. The pressure marker, NaCl, was also introduced into the cube. To prevent disturbances of the diffractograms the sample was not mixed with NaCl; both were placed in separate layers. Figure 2.2 visualizes this arrangement. Changing the position of the press by upward or downward motion it is possible to choose the point from which the diffractogram is taken. In this way we could move between the oxadiazole sample and NaCl and additionally scan across the sample to check the homogeneity.

The diffractograms obtained this way had to be converted to a usual 2θ-scale for their posterior analysis. The conversion was carried out using the diffraction angle θ_E determined for NaCl in the closed pressure cell at ambient pressure and the wavelength corresponding to Cu K_{α_1} radiation (λ=1.5406 Å). In the following we describe the transformation procedure.

Starting from Bragg's law for the first order of diffraction,

$$2d \sin\theta = \lambda \,, \tag{2.1}$$

where d is the inter-planar distance, θ the diffraction angle and λ the wavelength of the radiation, we modify it taking into account the relation between energy E and wavelength λ

$$E = \frac{hc}{\lambda} \,, \tag{2.2}$$

leading to

$$2d \sin\theta = \frac{hc}{E} \,. \tag{2.3}$$

We have substituted the values of three different inter-planar distances of NaCl and their corresponding energies into this equation. The d-spacings of NaCl at ambient pressure are well known [54]. We chose the families of planes: (200), (220) and (111). Their energies were extracted from the diffractograms. With these data as input, we obtained three values for the diffraction angle only slightly different, from which we determined the mean value. We called it the energy dispersive diffraction angle, θ_e. This angle depends on the experimental run because the adjustment of the detector to the X-ray beam may slightly vary (due to a slightly varying press position for

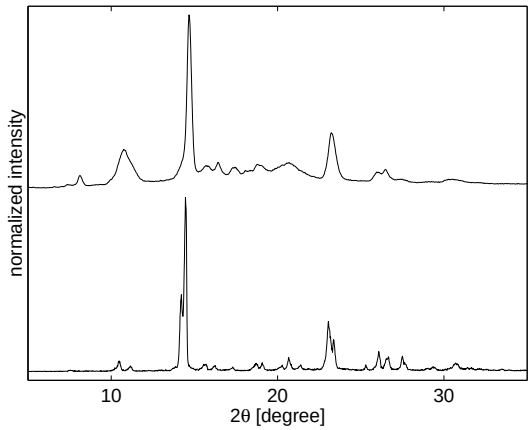

Fig. 2.3: X-ray diffraction pattern of DPO II at 303 K acquired with the STOE equipment using angle dispersive technique (bottom) and at 0 GPa acquired with the MAX-80 equipment using energy dispersive technique (top). The first peak in the energy dispersive diffractogram is a escape peak due to the detector material (Ge). The resolution of the pattern acquired with angle dispersive technique is considerably better.

mechanical reasons). However, it was always around 2.7°. Once θ_e is known, the energy scale can be transformed into the $2\theta_a$ scale, where θ_a denotes the angle dispersive diffraction angle. The d-spacings expressed for an energy dispersive diffraction pattern are

$$d = \frac{hc}{2\sin\theta_e E}\,, \tag{2.4}$$

while for an angle dispersive diffraction pattern it reads

$$d = \frac{\lambda}{2\sin\theta_a}\,. \tag{2.5}$$

As the d-spacings have to be equal, we obtain for the $2\theta_a$ scale

$$2\theta_a = 2\arcsin\left[\frac{\lambda\sin\theta_e E}{hc}\right]\,. \tag{2.6}$$

The pressure within the cell was determined *in situ* through the usual Decker equation for NaCl [55]. This equation establishes the relation between the lattice parameter of NaCl and pressure. Two diffractograms of NaCl were taken at every pressure step, before and after the measurement of the neighbouring oxadiazole sample. The three most intense peaks of NaCl—those corresponding to the families of planes (200), (220) and (111)—were used to determine the lattice parameter of NaCl. The values obtained for the cell axis were introduced into the Decker equation and the pressure within the sample calculated. Deviations between the values obtained before and after the measurement of the sample indicate that slight pressure gradients of 0.1 GPa may be present. We did not take into account the correction to the Decker's scale proposed by Brown [56] because in our pressure range it remains lower than 0.1 GPa, which is below the experimental error.

2.2.3 X-ray experiments under heating

The structure investigations with increasing temperature were carried out on a usual powder diffractometer STOE with a scintillator detector. Cu K_α radiation (λ=1.5419 Å) was used. For the data collection the $2\theta : \omega$ scan type was used. The samples were measured in the range $5° < 2\theta < 50°$ with 0.02° steps and 5 s per step.

The diffractometer was equipped with a heater, which allowed to achieve temperatures up to 1000 K, and vacuum chamber (pre-vacuum: 10^{-4} bar) to avoid larger temperature gradients and possible chemical reactions. The error in the temperature determination was lower than 4 K.

2.3 Spectroscopical studies

2.3.1 Diamond anvil cell

For the achievement of high pressure in the spectroscopical studies we use a diamond anvil cell (DAC) [57]. This device combines many advantages such as transparency in a broad range of the spectrum, small size, portability, etc. The basic principle of the DAC is very simple. A sample placed between the parallel flat faces of two opposed diamond anvils is subjected to pressure when a force pushes the two opposed anvils together (see fig. 2.4). The working faces of the diamonds (culets) have a diameter of 0.6 mm. A thrust generating mechanism, in our case a lever, transmits the external force which is simply manually applied to the anvils. The diamonds are separated by a metal plate, the gasket. The gasket which has an original thickness of approximately 0.2 mm is pre-indented by the anvil faces. This way the gasket material flows from the central to the exterior part forming a well and reducing its thickness in the center to about 0.07 mm. After the indentation a hole of 0.2 mm in diameter is drilled at the center of the indentation. This hole serves as sample chamber in order to confine the sample. Furthermore, the gasket provides support for the anvils. We used an alloy of Fe/Ni as gasket material. The gasket hole is filled with the sample (some small oxadiazole crystals), a pressure marker and a pressure transmitting fluid. As pressure marker we used tiny ruby chips (smaller than 0.03 mm). Since the position of the R1 line (694.2 nm at ambient pressure) of the fluorescence spectrum of ruby (Cr^{3+}-doped Al_2O_3) is calibrated as a function of pressure [58, 59], it suffices to acquire an emission spectrum of the ruby (excited by a He-Ne laser) to determine the pressure *inside* the cell. To achieve hydrostatic pressure the sample chamber was filled with fluorinert F-77 provided by 3M. This fluid guarantees hydrostatic conditions up to approximately 3.5 GPa and quasi-hydrostatic up to around 70 GPa. Fluorinert was chosen because it shows no remarkable absorption or luminescence signal in the spectral range investigated. The error in the pressure determination was estimated to be up to 0.1 GPa.

2.3.2 Absorption and fluorescence spectroscopy

Absorption and luminescence measurements of solutions at ambient pressure were acquired with standard spectrometers: the UV-Vis spectrometer Lambda 19 for the absorption and the luminescence spectrometer LS 50 for the luminescence, both commercialized by Perkin Elmer. Quartz cells were used for the collection of the absorption and luminescence spectra of solutions.

Optical measurements in organic crystals present difficulties because of the characteristics of these materials. Like most of the organic compounds, low molecular oxadiazole derivatives present difficulties to grow large single crystals. The oxadiazole substances investigated build mostly small polycrystalline needles or plates with dimensions of ten to hundred micrometers (cf. §3.2). Polycrystallinity implies the presence of multiple surfaces in the sample which act as diffraction centers. Additionally, scattering effects should be considered. The samples prepared for the optical measurements consisted of a rather uniformly distributed layer of several crystals on a quartz plate.

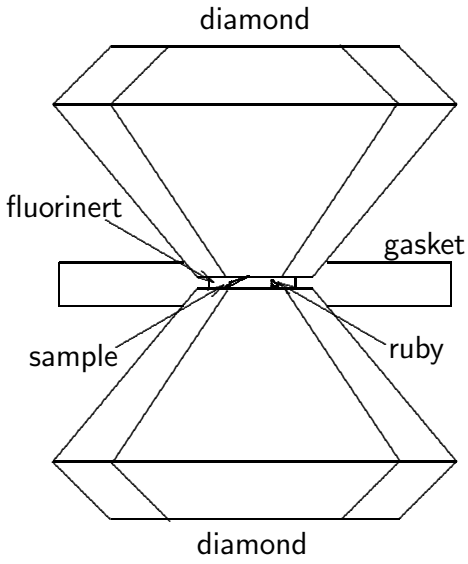

Fig. 2.4: Scheme of the basic part of a DAC. Opposed diamond anvil configuration with a metal gasket for sample confinement in a pressure medium.

The difficulty to prepare highly homogeneous films together with the inherent polycrystallinity of these crystals prevents the acquisition of sufficiently good absorption spectra. These difficulties were partially solved by the improvement of the local resolution in the measurements. Optic fibers were used to illuminate a small area of the sample and to collect the transmitted/emitted light. However, the large thickness of the crystals still prevents the correct determination of the spectral form of the absorption. But the preparation of very thin (range of micrometers) single crystal pieces with parallel faces is still impossible with the available techniques. Also the drop technique were thin polycrystalline films should result (see for instance [60]) was inadequate for the oxadiazole compounds discussed here. So, in the future refined techniques such as microtome cuts should be tested.

With a PTI UV-Vis luminescence spectrometer as starting point, a modular setup for both absorption and luminescence investigations of crystals was developed. An external white light source in the UV-Vis range (deuterium-halogen) equipped with fiber connection allowed the use of the luminescence spectrometer as absorption spectrometer as well. A quartz optic fiber guided the light from the lamp to the sample (see fig. 2.5 for a schematic illustration). Another optic fiber collected the light from the sample, leading it to the slit of the emission monochromator. The quartz fibers are transparent up 235 nm. The optic aperture of the fiber coincided with that of the emission monochromator entrance allowing the direct connection of the fiber to the slit without further modifications. As detector served a photo-multiplier.

For the luminescence investigations the setup was modified. Another UV-Vis arc lamp (xenon) was connected to the excitation monochromator in such a way that monochromatic light with the desired wavelength could be used as excitation source. A quartz optic fiber conducted the light from the slit of the excitation monochromator to the sample (see fig. 2.5). The collection of the light emitted by the sample and its guidance to the emission monochromator was performed with the same setup as in the absorption measurements.

Oxadiazole crystals are characterized by a large overlap between absorption and luminescence, indicated by the small Stokes shifts. This fact induces inner filter effects which give rise to difficulties to acquire luminescence spectra in inline geometry. To avoid this problem the sample was mounted on a goniometer. Thus, the angles could be varied to optimize the collection of the emitted light. We worked in a right angle geometry, where the incident beam formed an

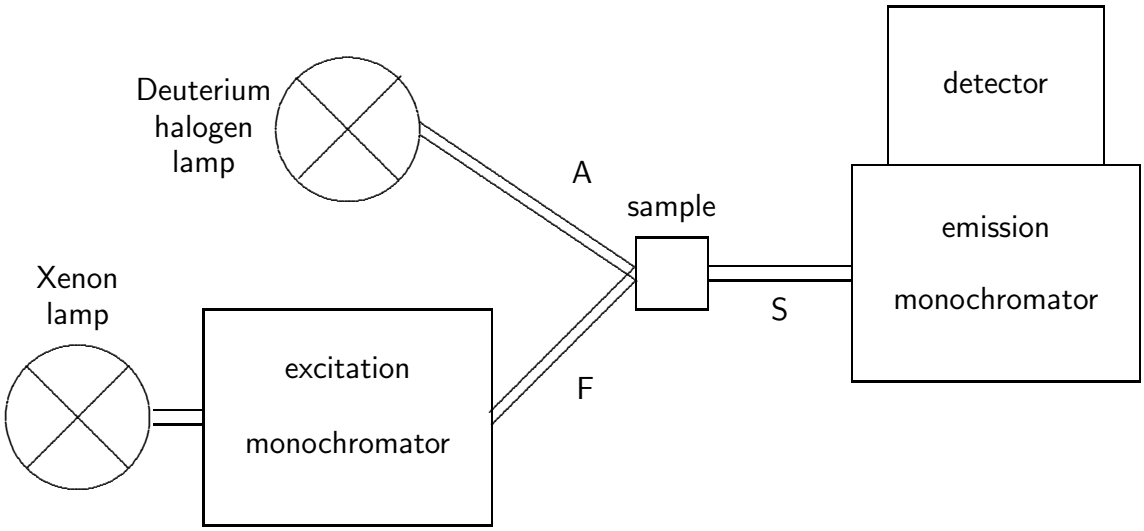

Fig. 2.5: Scheme of the experimental setup for the UV-Vis spectroscopy. The absorption measurements were performed connecting the light source to the sample by an optic fiber (marked with A). In the fluorescence measurements the light of the lamp is first monochromatized in the excitation monochromator and then guided to the sample by another optic fiber (marked with F). In both cases the light collected from the sample goes to the emission monochromator through a third optic fiber (marked with S).

angle of approximately 60° with the normal to the sample and the emitted light was collected at approximately 30° to the normal.

The investigations at *high pressure* were also performed with the fiber technique explained above. Appropriate coupling allowed the optimal connection of the optic fibers to the diamond anvil cell. The characteristics of this coupling only permitted measurements in transmission (also in the fluorescence so that here inner filter effects could not be avoided).

To allow comparison between the different measurements (e.g. solutions and crystals), the spectral slit width of all spectrometers was set to 2.5 nm and all measurements were taken in steps of 0.5 nm.

2.3.3 Raman spectroscopy

The Raman measurements were performed using a He-Ne laser (λ=632.8 nm) for excitation. The laser light was focused to a small spot of around 0.01 mm diameter so that the spectra are collected from single crystals. The laser output was reduced to less than 4 mW to avoid thermal heating effects of the sample. A triple Raman spectrometer system (focal length 0.75 m) with a liquid nitrogen cooled CCD detector (T64000, Instruments S.A.) was used for recording the scattered light. An additional camera system allowed the visual inspection of the sample and the precise localization of the laser spot on the sample. As can be seen in fig. 2.6, we used a free setup which allows the easy change between different samples, in particular between free samples for the ambient pressure experiments and samples within the DAC for the high pressure measurements. With a typical width of the entrance slits of 0.1 mm (first entrance slit) and 0.2 mm (entrance third stage) and a grating with 1800 grooves per cm, the resolution of the system was about 1 cm^{-1}. All spectra were calibrated using the spectral lines of Ne from a Pen Ray calibration lamp (LOT-Oriel).

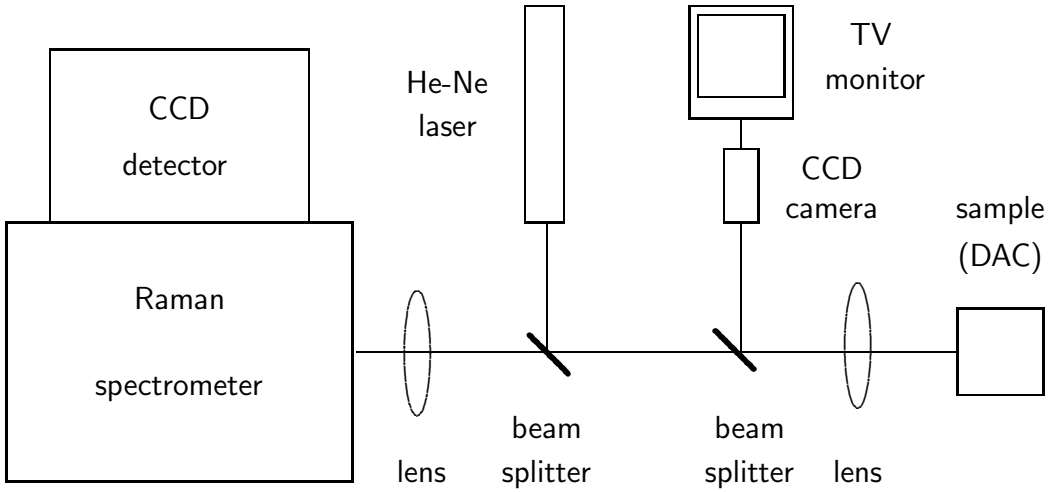

Fig. 2.6: Scheme of the experimental setup for the Raman spectroscopical investigations.

2.4 Thermal gravimetric analysis and differential scanning calorimetry

For the thermal gravimetric analysis (TGA) a TGA 7 device by Perkin Elmer was used. The samples, around 5 mg, were measured under nitrogen flow. The differential scanning calorimetric (DSC) studies were performed on samples of approximately equal mass applying a DSC 7 device (Perkin Elmer). Usual heating rates of 10 K/min were compared to some runs with heating rates of 20 K/min. The precision of the temperature measurement of both techniques is 0.5 K.

Chapter 3

Crystal structure at normal conditions

3.1 Introduction

As starting point for our investigation, the crystal structures of several oxadiazole compounds were studied [45, 46, 47, 48, 50, 61, 62, 63, 64, 65, 66, 67, 68, 69]. The knowledge of the molecular conformation and arrangement in the crystal is a very valuable information for our subsequent investigation. Physical properties such as UV-Vis absorption and fluorescence (§6.4), lattice and molecular vibrations (§8.3), and their behaviour under compression (§7.3 and §8.4) are influenced by the crystal packing of a given substance.

In recent years the crystal structure of many oxadiazole compounds has been determined [45, 47, 48, 50, 51, 61, 62, 63, 64, 65, 66, 67, 68, 69, 70, 71, 72]. However, a systematic study of the molecular arrangement related to the different functional groups attached to the oxadiazole ring is missing up to this date. With the present work, we try to deliver some contributions which help filling this gap. Here, we present for the first time a detailed description and comparison of the molecular conformation and the crystal packing of several oxadiazole compounds. Since this thesis principally deals with four oxadiazole compounds, in the present chapter only the crystal structures of these four compounds are described. For the purpose of comparison, a description of similar oxadiazole crystals is reported in appendix A.

3.2 Morphology and polymorphism

Although we did not carry out a complete study of the morphology of the crystals, some features of their appearance may be pointed out. One noteworthy fact is that for DPO and for 6DPO6 two different morphologies are found. Depending on the crystallization process, DPO builds two kinds of crystals [46]. When the crystallization is performed from a solution in petrol ether, white-transparent needle-like crystals with dimensions in the range of several millimeters for the long needle axis and some tens of micrometers for the other two directions are obtained. Typically, few needles are joined together, building a fan shaped poly-crystal. If the solvent used in the crystallization process is ethanol, colorless plate-like up to prismatic crystals arise. A representative specimen has dimensions of some hundreds of micrometers for the two large axes and tens of micrometers for the short one. The structural analysis revealed that both needle- and plate-like crystals also differ in its structure, that is, DPO can crystallize in at least two polymorphic forms. The needle-like crystals constitute the polymorph with the higher symmetry DPO I, while the plate-like crystals have a very complex crystal structure, DPO II.

Crystallization is a complicated process where all fragments of the molecules interact among each other to achieve a structure with minimum free energy. It is known that the overall optimization of forces which occurs in this process can be influenced by experimental preparative conditions such as temperature, pressure, nature of the solvent, concentration, cooling and stirring rates, presence of impurities, etc. [73]. Consequently, different polymorphic forms of the same compound may be obtained under different preparation parameters—as the nature of the solvent in the case of DPO. Although at a given temperature and pressure only one polymorph is thermodynamically stable, the coexistence of several polymorphs under normal conditions is usual. This is due to the fact that the rate of transformation of meta-stable phases to the stable one may be slow, or even negligible. Polymorphism is a rather common feature in organic compounds because of the multiple and weak inter-molecular interactions which hold organic molecular crystals together. The weakness of the forces induces the free energy differences between different polymorphic forms to be small, generally around few kJ/mol [73].

The reasons why DPO can crystallize in two different structures are not clear. Taking into account the dimensions of the resulting crystals—DPO I builds larger crystals than DPO II—, it can be suggested that the crystallization from a petrol ether solution implies the formation of few nuclei, which facilitates the achievement of bigger crystals. The non planarity and alternating orientation of the molecules in the second polymorph support the idea of a rapid crystallization process with the formation of many nuclei. Nevertheless, it is important to note that both polymorphs contain similar π-complexes (see §3.4.1 and §3.4.2) which is determinant for features such as the electronic transitions of the crystals (this point is discussed in detail in §6.4). Moreover, both polymorphs present a close packing with similar densities: 1.285 g/cm^3 for DPO I and 1.259 g/cm^3 for DPO II.

The crystalline form of 6DPO6 presents as well singularities. We investigated two samples of 6DPO6. The first sample was provided by Aldrich and used as received*. It consists of small colorless prismatic crystals with dimensions of the order of hundreds of micrometers in each direction. Powder X-ray diffraction examination of the sample at 303 K showed that it contained mainly one modification of crystals, 6DPO6 I. A second sample was synthesized as usual, twice recrystallized from an ethanol solution, and finally dried in a vacuum-chamber. This sample cosists of yellowish needles with dimensions in the order of several hundreds of micrometers for the long needle axis and some tens of micrometers for the other two directions. Its powder was also studied by means of X-ray diffraction at 303 K. It resulted that this second sample is a mixture of two crystalline modifications. 21% of the sample corresponded to 6DPO6 I. The remaining 79% built a new molecular packing where water molecules are incorporated in the crystal structure, which occurs for the first time in an oxadiazole compound. The water molecules originate from the impurities (4%) of the ethanol used for the recrystallization. The intense H-bonds between the water and the 6DPO6 molecules prevent the dehydration of the sample in the drying-chamber (cf. §3.4.4). This phenomenon, that is, the inclusion of solvents in the crystal structure of a given chemical substance, is usually designated as pseudo-polymorphism [74]. Strictly, it is not polymorphism because it involves different chemical species. We chose the term *modification* to distinguish the water free and water containing structures.

The compound 6DPO4 also builds long light yellow needles with the same typical dimensions as 6DPO6 II. The two rings containing 7PO3 crystallizes in colorless prisms with dimensions of the order of hundreds of micrometers in each direction. It is interesting to note that 6DPO6 I as well as 6DPO4 form big prisms when they crystallize from the sublimation.

The crystallographic data of the investigated compounds are summarized in table C.1.

*Except in the spectroscopical investigations, where crystals obtained from the sublimation were used.

3.3 Molecular conformation

All the crystals studied here are built by quite planar molecules. The oxadiazole unit is perfectly planar, as usual for oxadiazole compounds, and the phenyl(ene) rings are nearly planar. The oxadiazole and phenyl(ene) rings are nearly coplanar with only slight deviations of the planes of the phenyl(ene) rings with respect to the plane of the oxadiazole ring which can be in the same or in opposite directions. The nearly coplanarity of the rings favours a partial conjugation of the π electron system along the whole molecule. The shortness of the inter-ring bonds compared with the theoretical value expected for a C(sp^2)-C(sp^2) single bond (which is 0.148 nm, [75]) confirms this partial conjugation. The substituents scarcely influence the planarity of the molecule. The most important data concerning the molecular conformation are reported in table C.3.

It is noteworthy that the molecules of DPO II and 6DPO6 I show a larger deviation from planarity than those of the other crystals (cf. table C.3). In DPO II the deviation of the phenyl groups from the molecular plane, defined by the oxadiazole unit, differs among the six molecules which constitute the asymmetric unit[†]. It has the maximum value 11° and the mean value 6°. The phenyl rings are rotated in opposite directions to the oxadiazole group. In 6DPO6 I the deviation from planarity is even larger, though still rather low: the phenylene rings are 15° and −14° inclined to the oxadiazole unit. Despite these molecules are not perfectly planar, their inter-ring bonds are shorter than the theoretical C(sp^2)-C(sp^2) single bond, indicating the partial conjugation of the π electrons along the molecule. Therefore, it can be concluded that such deviations from planarity do not disturb the conjugation significantly. However, since the length of the inter-ring bonds in DPO II and in 6DPO6 I is slighly larger than in the other crystals, their conjugation may be smaller (cf. table C.3).

3.4 Molecular arrangement

3.4.1 DPO I

The molecular arrangement of DPO I is depicted in fig. 3.1[‡]. DPO I crystallizes in a herring bone structure. A herring bone arrangement is characterized by stacks of parallel molecules where the molecules of adjacent stacks have opposite inclination to the stack axis. The stack axis is a. Within the stacks the molecules are oriented in the same direction, referring to the line joining the center and the O atom of the oxadiazole ring. Neighbouring stacks are translated in the b-direction, avoiding an aligned arrangement of the oxadiazole rings along c (fig. 3.1(a)). The molecules of adjacent stacks show an inclination angle of ±41° to the stack axis, respectively (fig. 3.1(b)).

The most intense inter-molecular interactions[§] in DPO I occur along a stack between the π systems of the oxadiazole unit of one molecule and the phenyl groups of the adjacent molecules. This feature is also characteristic for other oxadiazole compounds. The strong electron acceptor character of the oxadiazole moiety induces the building of *π-complexes*. The term π-complex generally designates the complex which results from the interaction between the π electron systems of two molecules, one containing electron-rich ring systems (π-donor) and the other containing electron-poor ring systems (π-acceptor) [76]. In the case of DPO, this is slightly different. Now the π-donor and the π-acceptor are not molecules but parts of molecules. The π-donor is the phenyl ring and the π-acceptor the oxadiazole ring. Thus, every DPO molecule contains two π-donors and one π-acceptor. The sandwich arrangement along the stacks, where the oxadiazole ring of one molecule is located between two phenyl rings of the neighbouring molecules, is the result of the optimization of the π-π interactions between π-donors and π-acceptors. In this way,

[†]The asymmetric unit is the smallest part of a crystal structure from which the complete structure can be derived by use of the space group symmetry operations (including translations) [76].

[‡]Hydrogen atoms are omitted in all the figures of the crystal structures for the purpose of clarity.

[§]The data concerning the inter-molecular interactions within the crystals of the investigated compounds are summarized in table C.5.

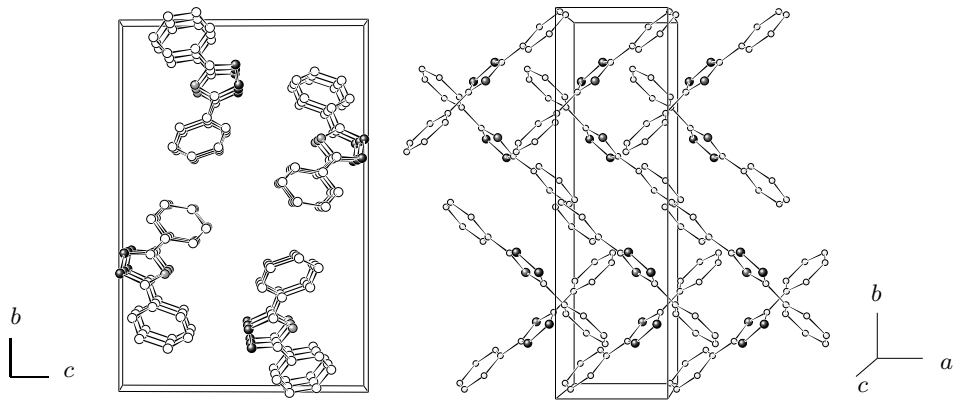

(a) Top view of the stacks.

(b) Lateral view of the stacks.

Fig. 3.1: Molecular arrangement of DPO I.

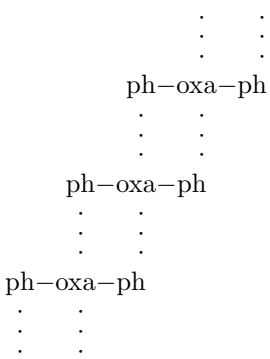

Fig. 3.2: Infinite π-complexes in DPO I.

the oxadiazole group of every molecule interacts with *two* phenyl rings of the adjacent molecules and the phenyl ring of a molecule interacts with *one* oxadiazole ring of the adjacent molecule. This is outlined in fig. 3.2. In this way a network of π-π interactions is built, resulting in the stacking of the molecules. Furthermore, the needle-like morphology of DPO I may result from the stack-arrangement. The distance between the molecular planes of a π-complex amounts to 0.344 nm[¶], which is the normal spacing for these complexes [77]. The existence of charge transfer within the complex is dismissed for two reasons. Firstly, in the case of having charge transfer the inter-molecular spacing should be shorter, around 0.31 nm [77]. And secondly, a charge-transfer band should appear in the UV-Vis absorption spectrum, which does not occur (§6.4).

The shortest inter-molecular distances in the crystal[‖] are found between the C atoms of the phenyl rings of molecules of stacks *adjacent to the b-direction* (0.321 nm, cf. table C.5). This results from a *van der Waals* interaction between the stacks. Taking into account that C atoms rarely approach each other closer than 0.34 nm, this van der Waals interaction can be described as strong [76]. A larger spacing is found between *adjacent* stacks *in the c-direction*. It appears

[¶]Inter-planar distances were determined as the mean value of the distance from several points of a plane to the other plane, defined by three points. For this reason they do not have standard deviation and are rounded to the third decimal figure.

[‖]When referring to distances between atoms, no H atoms are considered, except when dealing with H-bonds.

between an N atom of the oxadiazole group of one molecule and a C atom of the phenyl ring of its neighbour (0.342 nm). One may describe it as associated with a van der Waals force. However, we propose that this spacing is originated by a *weak H-bond* between one of the CH groups of the phenyl ring and an N atom of the oxadiazole ring. Such interactions, which are indeed at the limit between van der Waals forces and usual H-bonds, were already described for this (C-H$\cdots$N) and similar (C-H$\cdots$O) groups of atoms. They present high directionality, the H-bond angle lies between 100° and 180° with a major cluster between 150° and 160°, and have C$\cdots$N spacings in the range 0.3...0.4 nm [78]. In the case of DPO I, the parameters of the *weak H-bond* are: distance C-H$\cdots$N, 0.273 nm; spacing between C and N, 0.342 nm; and angle C-H$\cdots$O, 124°.

3.4.2 DPO II

The crystal structure of the second polymorph of DPO is more complicated. Though it shares with the first polymorph the crystal system —both are monoclinic (table C.1)—the arrangement of the molecules in the unit cell is much more complex. DPO II is non-centrosymmetric, which makes it a promising candidate as non linear optical material for the generation of second harmonics. This feature of DPO II is very surprising because organic compounds usually pack in centrosymmetric arrangements. Actually, it occurs for the first time for an oxadiazole crystal. Figure 3.3(a) shows the unit cell, which contains 24 molecules. The crystal packing is characterized by stacks of molecules. These stacks build layers parallel to the *ab*-plane (fig. 3.3(b)). The molecular planes are perpendicular to the layer plane.

The molecular arrangement along a stack is reminiscent of the one encountered in the first polymorphic form. Parallel molecules are placed in such a way that the oxadiazole unit of a molecule is sandwiched between the phenyl rings of the adjacent molecules, leading to the formation of π-*complexes* like those explained above for DPO I. Nevertheless, the difference to the infinite stacks of DPO I lies in the fact that every third molecule of the stacks of DPO II is oriented in opposite direction (referring to the oxadiazole ring) in relation to its neighbours. This fact has two consequences. Firstly, the prevention of the formation of *perfect* stacks. Secondly, the appearance of two kinds of π-complexes: one between molecules with the same orientation and another between molecules with opposite orientation. Since DPO shows a boomerang-like shape, the overlap of the π systems is higher when the molecules have the same orientation than when the molecules have the opposite orientation. The spacing between molecular planes of molecules with the same orientation amounts to 0.338 nm and to 0.355 nm when the molecules are oriented in opposite directions. Corresponding molecules of adjacent layers are tilted by 13°. This small deviation from parallel arrangement complicates the crystal structure.

Alternating stacks in zig-zag arrangement build a layer. The molecules of adjacent stacks are oriented perpendicular to each other. They interact through *van der Waals* forces between the phenyl rings (cf. table C.5).

Different layers are connected through *weak H-bonds* between a CH group of the phenyl ring of a molecule and an N atom of the oxadiazole ring of another molecule (cf. table C.5).

3.4.3 6DPO6 I

Both crystal structures of 6DPO6 are orthorhombic (table C.1). The water free modification (6DPO6 I) has a herring bone arrangement with b as stack axis (fig. 3.4). The packing of the molecules along a stack is such that one molecule is turned around 83° in relation to its neighbours (fig. 3.4(a)). The orientation of a molecule was determined by the line which joins the N atoms of the oxadiazole unit. Every second molecule along the stack shares the same orientation. Taking this into account, it should be remarked that the stacking along b only involves the oxadiazole rings and not the whole molecule. The molecular planes are tilted by about $\pm$36° to the stack axis. Contiguous molecules are slightly tilted relative to each other (7°) and show a short mean

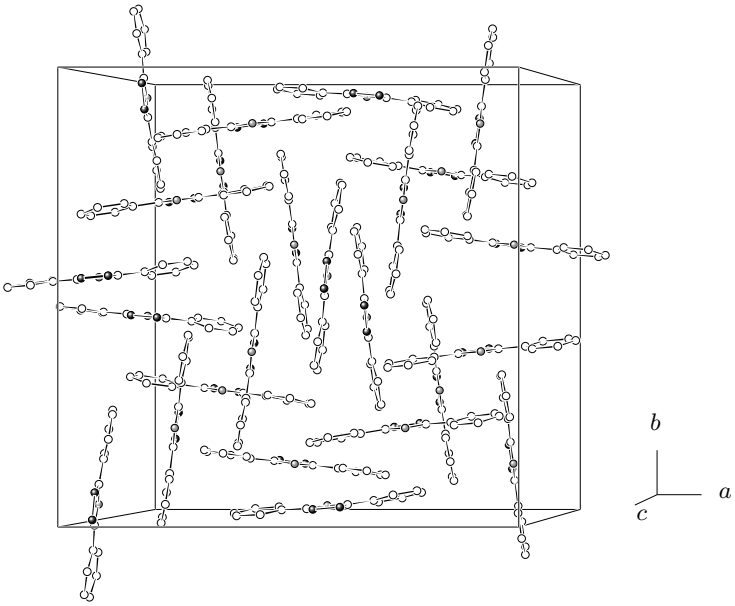

(a) View of the unit cell.

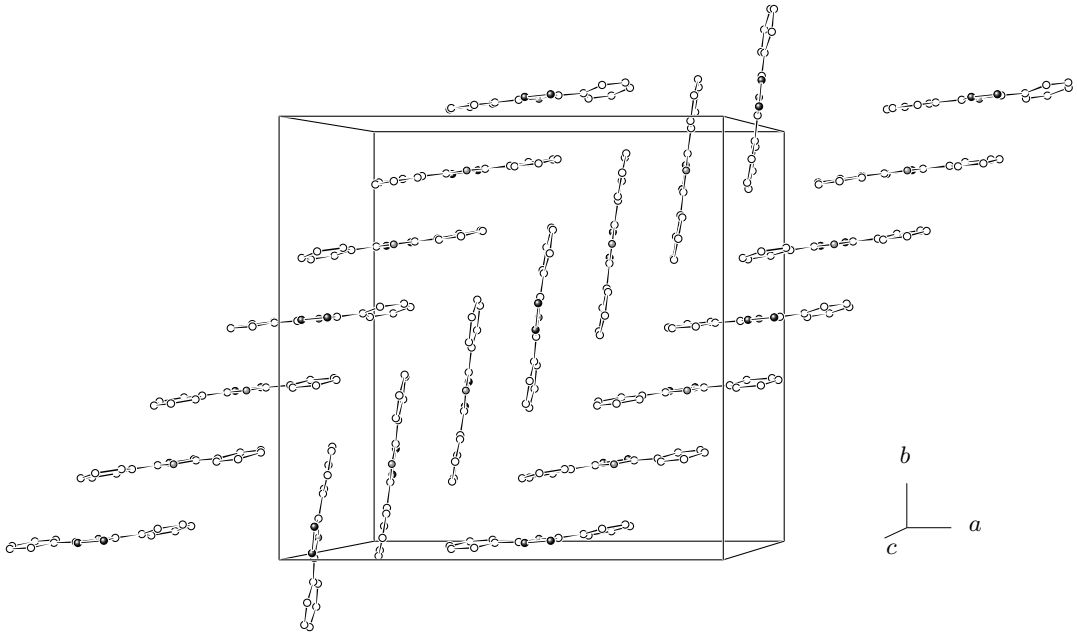

(b) View of a layer.

Fig. 3.3: Molecular arrangement of DPO II.

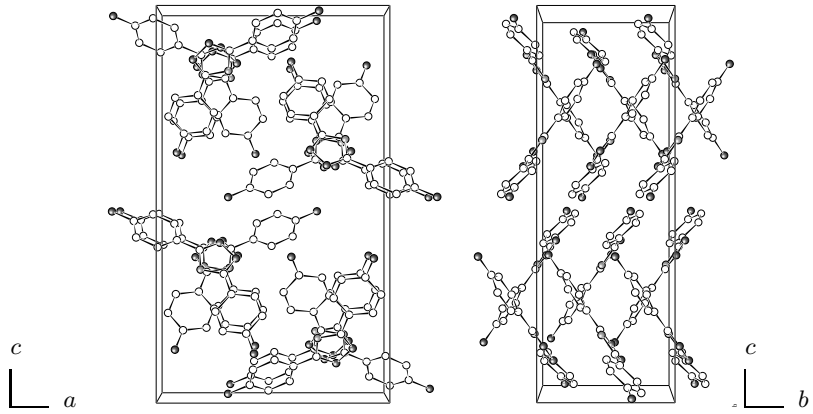

(a) Top view of the stacks. (b) Lateral view of the stacks.

Fig. 3.4: Molecular arrangement of 6DPO6 I.

spacing between the atoms of the oxadiazole rings (0.325 nm). Thus, the forces responsible for the building of the stacks are π-π interactions just between the oxadiazole rings of the molecules, that is, between two π-acceptors. The Coulomb repulsion between NH_2 groups and phenylene rings induces the turn of adjacent molecules and prevents the formation of π-complexes.

Two kinds of interactions appear between stacks. On the one hand, *adjacent* stacks *along the axis c*, are connected by *weak H-bonds* between the NH_2 group of a molecule of a stack and an N atom of the oxadiazole ring of a molecule of an adjacent stack. On the other hand, *adjacent* stacks *in a-direction* interact through *van der Waals* forces between the phenylene rings (cf. table C.5).

3.4.4 6DPO6 II

The crystal structure of the water containing modification is characterized by the existence of layers of 6DPO6 molecules and of water molecules parallel to the *ab*-plane (fig. 3.5). Inside a layer all molecules lie in the layer plane and have two opposite orientations regarding the line between the center and the O atom of the oxadiazole ring. They are arranged in rows parallel to *a* (fig. 3.5(b)). The rows are strongly connected by *H-bonds*. The water molecules act as bridges between two neighbouring 6DPO6 molecules. One water molecule builds two H-bonds with the NH_2 groups of two 6DPO6 molecules which share the same *b*- and *c*-coordinates and are translated along the axis *a* (see fig. 3.5(a) and 3.6). The character of these bonds is so strong that the position of the H atom could not be perfectly determined. Neutron diffraction would be needed for this purpose. Its electronic density lies in the line joining the N and the O atoms [79]. As result of the refinement process, the H atom involved in this bond, which originally comes from the water molecule appears to be bonded to the N atom of 6DPO6. This is why we describe the H-bond by the distance H$\cdots$O which amounts to 0.187 nm. The angle of this H-bond is 176° and the spacing between the N and the O atoms—the most trustworthy quantity—amounts to 0.300 nm.

Two kinds of interactions hold the rows together, leading to the formation of the layer. There are *weak H-bonds* between an NH_2 group of one molecule and an N atom of the oxadiazole moiety of a neighbouring molecule (cf. table C.5). These weak inter-molecular H-bonds are very similar to those between the stacks of 6DPO6 I. The other interactions which appear between the rows of a layer are *van der Waals* forces between the phenylene rings (cf. table C.5).

The layers of 6DPO6 II interact through *van der Waals* forces between an N atom of the

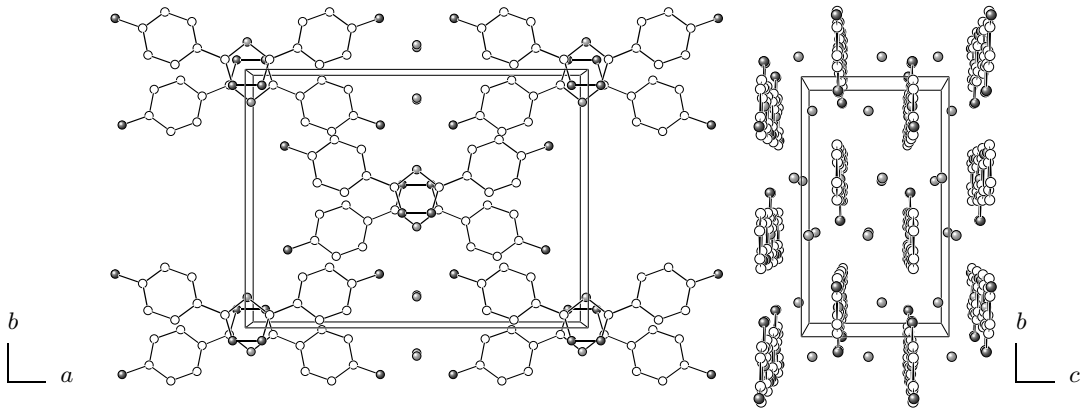

(a) Top view of the layers.

(b) Lateral view of the layers.

Fig. 3.5: Molecular arrangement of 6DPO6 II.

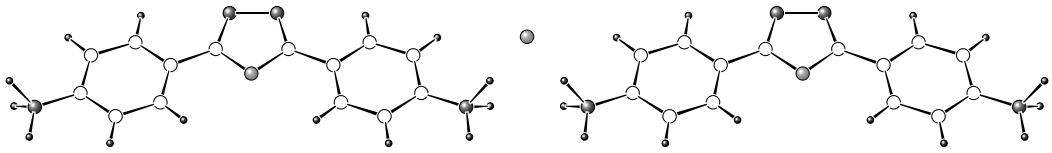

Fig. 3.6: Schematic illustration of the H-bonds between two 6DPO6 molecules and one water molecule. The 6DPO6 molecules belong to the same row and the water molecule is in a different depth. The H-bonds are so strong that the H atoms of the water molecule appear bonded to the H atom of the NH_2 group.

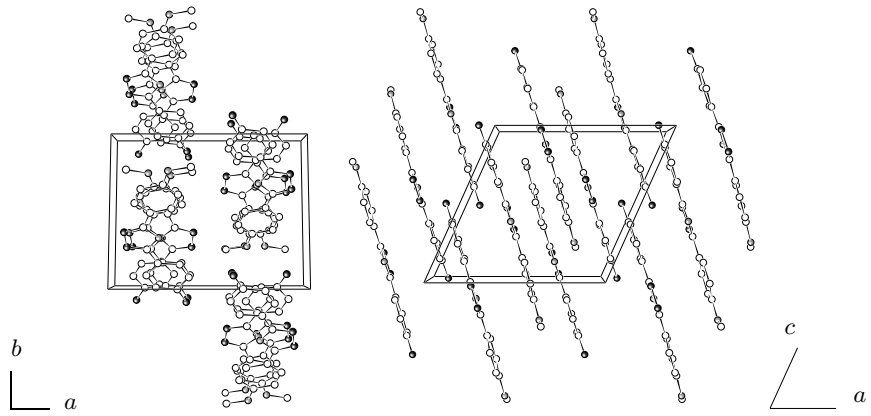

(a) Top view of the stacks.

(b) Lateral view of the stacks. Adjacent stacks in the figure lie in different depths.

Fig. 3.7: Molecular arrangement of 6DPO4.

oxadiazole ring and a phenylene ring and between the phenylene rings (cf. table C.5).

3.4.5 6DPO4

The three-dimensional molecular packing of 6DPO4 is characterized by the presence of stacks of molecules along c (fig. 3.7). The adjacent stacks are parallel to each other. Inside a stack, the molecules are arranged parallel to each other and with alternating orientation regarding the oxadiazole ring. All the NH_2 groups are aligned at the same end of the molecules of a stack. The molecular plane forms an angle of 42° with the stack axis. Again, the molecules of a stack are arranged in such a way that the oxadiazole unit of one molecule is connected by strong π-π interactions with the phenylene rings of the adjacent molecules. This leads to the building of π-*complexes* similar to those reported for DPO I and DPO II (see §3.4.1 and §3.4.2). The inter-planar distance inside a stack is 0.348 nm.

The forces between stacks are *van der Waals* interactions. *Adjacent* stacks *regarding the axis* a interact specially through the O atom of a OCH_3 group of one molecule and the phenyl ring of the neighbour molecule and *neighbouring* stacks *along the b-direction* through a N atom of the oxadiazole ring and the C atom of the OCH_3 group (cf. table C.5).

It is believed that 6DPO4 may build different polymorphs. One fact which induces this idea is the presence of a H-bond donor (the NH_2 group) and a H-bond acceptor (the O atom of the OCH_3 group) in the molecule. It is generally accepted that H-bonds will be formed whenever possible [77]. Thus, another crystal structure where the molecules build H-bonds may exist. Another fact which supports this hypothesis is the behaviour of this crystal at high pressure: it undergoes phase transitions under compression (cf. §4.4.1 and §8.4.1). From the study of its Raman modes under compression it is proposed that H-bonds may be built in the phase transition (see §8.4.1). Therefore, further crystallization procedures should be attempted in order to search for new polymorphic forms of 6DPO4.

3.4.6 7PO3

The molecular packing of the two rings containing 7PO3 is characterized by the existence of pairs (fig. 3.8(a)). The three-dimensional arrangement of the pairs results in a layer packing motif. The

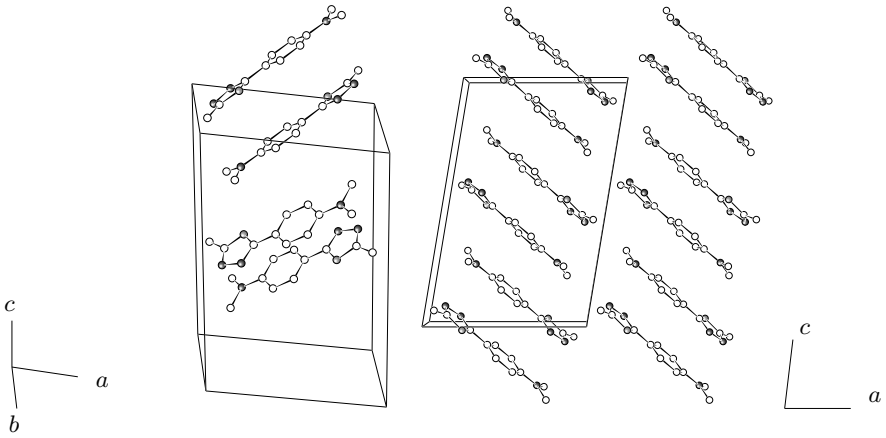

(a) View of two π-complexes.

(b) Lateral view of the layers.

Fig. 3.8: Molecular arrangement of 7PO3.

$$\begin{array}{c} \mathrm{N(CH_3)_2{-}ph{-}oxa{-}CH_3} \\ \vdots \quad \vdots \\ \mathrm{CH_3{-}oxa{-}ph{-}N(CH_3)_2} \end{array}$$

Fig. 3.9: π-complex in 3PO7.

layers are parallel to the *bc*-plane of the unit cell (fig. 3.8(b)). In a layer the molecules arrange in two sets slightly inclined to each other. Figure 3.8(a) shows two pairs in which two molecules are connected by strong π-π interactions. The π-*complex* which results from these π-π interactions shares some features with that found in DPO I, DPO II and 6DPO4. Again, the interactions occur between the oxadiazole ring of one molecule and the phenylene ring of the adjacent one. But now, the fact that 7PO3 only possesses one phenylene ring prevents the infinite sandwich arrangement of the other compounds. A π-complex of 7PO3 is represented in fig. 3.9. The molecules which form a pair are related by an inversion center. The distance between the molecular planes of a pair is 0.347 nm. The pairs are translated, inverted and inclined to one another.

The molecules are tilted to the layer plane. The angle which the molecular axes form with the layer plane amounts to approximately 60°. The shortest distance between layers occurs between the NH_2 group of one molecule and the CH_3 group of another molecule. From the relative orientation between the molecules of different layers and the spacing between them, it may be concluded that the forces responsible to pack the layers together are *van der Waals* interactions (cf. table C.5).

3.5 Relations among the crystal structures of the investigated oxadiazole compounds

A crucial question is whether it is possible to predict the *crystal* structure of a substance from the knowledge of its *molecular* structure. In general this is still not possible. Several kinds of inter-molecular interactions determine the formation of a crystal: electrostatic, hydrogen bonding, donor-acceptor, steric hindrances and van der Waals attractions. Additionally, these forces depend on the characteristics of the interacting partners and on their respective surroundings. This results in a large amount of possible interactions and thus crystal packings. An approach to this complicated problem is the *supra-molecular synthon model* introduced by Desiraju [74, 80]. He defined supra-molecular synthons as: 'structural units within super-molecules** which can be formed and/or assembled by known or conceivable inter-molecular interactions' [81]. In other words, synthons are the various ways in which complementary fragments approach to each other. Of course, two, three or more given fragments can interact in many different forms leading to many possible synthons. The identification of synthons and the determination of their relative importance, depending on their existence probability, substantially simplifies the comprehension of the structure of organic molecular crystals. The way to extract synthons from the crystal structures consists in the comparison of many crystals containing the same or similar molecular structure.

A particular point of interest in the present work is precisely the determination of common patterns of interaction (synthons) for oxadiazole containing compounds. The identification of synthons should allow the prediction of the molecular arrangement of crystals and indeed of thin films built by similar compounds. Furthermore, it may induce the design of new materials with desired properties.

We compared eleven crystal structures (those reported in appendix A were also taken into account). From this comparison we propose the π-*complexes* described in §3.4.1 as a novel synthon for oxadiazole compounds. The molecules which build the π-complexes are shifted in such a way that the interaction occurs between the oxadiazole unit of one molecule and the phenyl(ene) rings of their neighbours (cf. fig. 3.2 and 3.9). Seven of eleven oxadiazole crystals show this characteristic arrangement where parallel molecules are connected through π-π interaction (see tables C.5 and C.6). These π-complexes interact among them through van der Waals forces—mostly between the phenyl rings—and through weak H-bonds—mostly between a CH group of a phenyl(ene) ring and one of the N atoms of the oxadiazole unit (see tables C.5 and C.6).

3.6 Summary

From the study of the crystal structure of oxadiazole compounds the following statements can be concluded.

(i) The oxadiazole containing molecules studied here generally build white-transparent or yellowish long needles and small plates or prisms. The habits may slightly vary with the crystallization conditions.

(ii) The 1,3,4-oxadiazole ring is always perfectly planar and the phenyl(ene) ring nearly planar.

(iii) The DPO body shows only slight deviations from planarity, quantified by the dihedral angle between the planes of the oxadiazole and phenyl(ene) rings. These angles are mostly lower than 10°.

(iv) The nearly complete coplanarity between the oxadiazole and the phenyl(ene) rings favours the partial conjugation of the electronic π system along the molecule. As a measure for the

**The expression 'super-molecule' refers to a crystal

conjugation, we considered the length of the inter-ring bonds between the oxadiazole unit and the phenyl rings. Its value varies between 0.144 and 0.146 nm and is shorter than the 0.148 nm expected for a C(sp^2)-C(sp^2) single bond.

(v) Two compounds, DPO and 6DPO6, showed two different crystalline modifications. DPO II—one of the polymorphs of DPO—has a non-centrosymmetric structure being this way a potential material for non linear optical applications. In 6DPO6 II water molecules are incorporated in the crystal structure.

(vi) The molecular arrangement in most of the crystals is determined by the presence of π-*complexes* of the type outlined in fig. 3.2. The inter-planar distances between the molecules which build the π-complexes are in the range of 0.333 to 0.371 nm.

(vii) The presence of *infinite* π-*complexes* in the crystals induces a stack-like arrangement either with parallel stacks or with crossed stacks (herring bone).

(viii) Weak H-bonds and van der Waals forces constitute a net of interactions which hold the stacks together.

Chapter 4

Crystal structure under compression

4.1 Introduction

The knowledge of the molecular arrangement of a compound constitutes the starting point for the understanding of the inter-molecular interactions present in the system and hence of its properties. Further information can be achieved from the study of the behaviour of the solid under compression and/or under heating.

In the study of condensed matter under compression and/or heating it is decisive to achieve information about the spacings between the components. When dealing with crystalline substances, the most precise methods to do this are X-ray and neutron diffraction. A proper knowledge of the structural behaviour of the material under compression and under heating is needed in order to determine an equation of state for the system [82, 83, 84, 85, 86, 87], which in turn provides parameters for inter-atomic potentials used in theoretical calculations [87, 88, 89, 90, 91, 92, 93, 94, 95, 96, 97, 98, 99, 100, 101, 102]. In addition, equations of state have important industrial applications, e.g. in the estimation of tableting properties of pharmaceuticals [103].

In this chapter we present the results of a structural investigation of oxadiazole compounds under compression performed by X-ray energy dispersive diffraction. One emerging question for organic substances is if there exist some general trends for equation-of-state parameters based on similarities in molecular and/or super-molecular structures. In an attempt to answer this question we have compared our results—found for oxadiazole containing molecules—with those of other similar aromatic compounds.

4.2 Literature review

For a large number of inorganic compounds, the study of the structural modification under compression and under heating allowed the determination of an equation of state for the system [56, 104, 105, 106, 107, 108]. Additionally, the study of phase transitions as well as of meta-stable phases of many inorganic compounds has attracted great interest by theoreticians [109, 110, 111, 112, 113]. Nevertheless, only few is known about the structural behaviour of organic compounds at high pressure. In the following we comment on a number of relevant articles dealing with systems similar to the present ones.

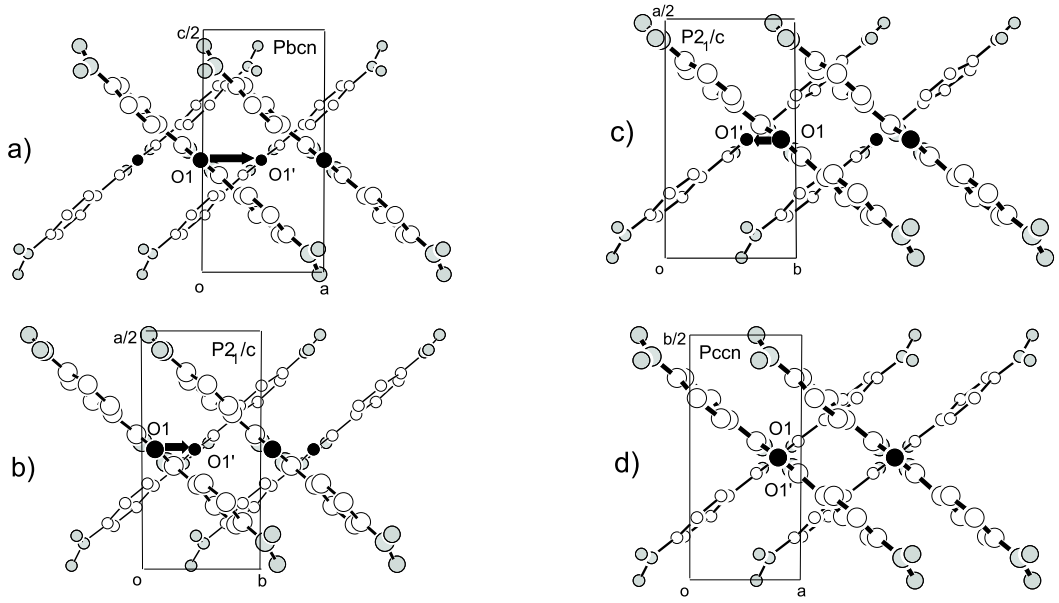

Fig. 4.1: Structure variation of 1DPO1 with pressure; from [63]

4.2.1 1DPO1

Of fundamental importance for our study are the investigations that Orgzall et al. carried out on 1DPO1 (the DPO derivative with R_1=R_2=NO_2) up to 5 GPa [63]. The authors combined different experimental techniques, such as Raman scattering and X-ray energy dispersive diffraction, with molecular modelling simulations by means of force field calculations using the commercial package Cerius2 [114]. Here we summarize their results concerning the crystal structure study. A discussion about the Raman investigation can be found in §8.2.2.

Changes in the external Raman modes and in the X-ray patterns indicate that 1DPO1 undergoes three phase transitions up to 5 GPa (at 0.88, 1.28 and 2.2 GPa). By comparison of the experimental X-ray patterns with simulated ones, the crystal structure of the high pressure phases could be determined (phase I: orthorhombic, *Pbcn*; phases II and III: monoclinic, $P2_1/c$; and phase IV: orthorhombic, *Pccn*). All phase transitions are reversible. For a description of the crystal structure of 1DPO1 at ambient pressure see §A.2.4.

Orgzall et al. describe the mechanism of the phase transitions as a typical topotactical reaction. The herring bone structure is conserved in all phases as well as the arrangement of the molecules along a stack. The only feature which changes is the relative position of the stacks, as fig. 4.1 illustrates. The closely packed arrangement and the large molecular volume hinder large changes in the position and orientation of the molecules.

4.2.2 Biphenyl

Puschnig et al. recently studied the effect of pressure on the electronic, molecular and crystal structure of solid films of polycrystalline biphenyl [115]. In their investigation, they combine experimental methods, X-ray powder diffraction up to 0.2 GPa and optical absorption up to 0.3 GPa, with three-dimensional band structure calculations. In the computations, with the Wien97 code [116], they follow the density functional theory for three-dimensional periodic systems. Biphenyl is, to our knowledge, the only oligo(para-phenylene) from which the crystal structure at high pressure has been investigated by means of X-ray diffraction. Since biphenyl has a a similar chemical struc-

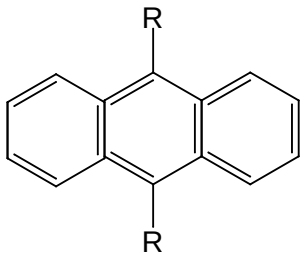

Fig. 4.2: Anthracene derivatives.

ture to 7PO3—both have two aromatical rings—it will be interesting to compare its compression behaviour with that of 7PO3.

The crystal structure of biphenyl at ambient pressure was determined by Charbonneau and Delugeard [117]. Planar molecules crystallize in the monoclinic system with space group $P2_1/a$ and lattice parameters a=0.812(2), b=0.563(1), c=0.951 nm and β=95.1°. There are two molecules per unit cell. The biphenyl molecules arrange in a herring bone structure with an angle between the molecular plane and the stack axis, the cell axis a, of 57°.

Puschnig et al. performed their study in consecutive steps. Firstly, they determined the lattice constants from the different high pressure diffractograms. They found a linear compression behaviour of the lattice parameters. Then they optimized the bond lengths and angles and the orientation of the molecular axis, under the constraint that biphenyl stays planar. From these calculations, they report that the herring bone angle increases leading to a slightly more cofacial arrangement. Besides, the inter-ring bond and its contiguous bonds in the phenyl rings are shortened, the former one more strongly, while the other bonds of the phenyl rings scarcely change.

Several authors reported that oligo(para-phenylene)s in crystalline state are planar only on average [118, 119, 120, 121]. This is associated with large librational amplitudes around the long molecular axis. Puschnig et al. calculated the pressure modification of the potential which describes the libration. At ambient pressure this potential shows a W-shape versus the torsion angle between the phenyl rings; the energetically most favorable conformation is the one with a twist of 15° (40 meV less than the planar conformation). At 0.2 GPa the most favorable torsion angle is 5° (5 meV less than for 0°). Already at 0.3 GPa the potential is U-shaped and therefore the most favorable conformation is the planar one. Thus the molecule undergoes a planarization at high pressure due to the inter-molecular packing interactions.

4.2.3 Anthracene derivatives

In a series of articles, Brillante et al. [88, 89, 90, 91, 92] studied the pressure-induced phase transitions of some 9,10-disubstituted anthracenes by means of Raman spectroscopy, optical absorption and fluorescence experiments, and lattice dynamics calculations. Anthracene is an aromatical molecule consisting in three condensed rings (see fig. 4.2). Thus, the substances investigated by Brillante et al. cannot be directly compared with ours, however they share with the oxadiazole crystals the fact of being built by planar molecules. The crystals formed by these substances are considered quasi-one-dimensional because they pack in stacks. From comparison of different substituted anthracenes it arose the question about the factor which determines the possibility of a phase transition. When the substituents are Cl, Br or O, the crystals present a pressure-induced phase transition at 3, 2.2 and 1.3 GPa, respectively, while for the case of I or CH_3 as substituents no phase transition in the same pressure range is observed. To resolve this question, lattice dynamics calculations with a Buckingham potential model between atoms of rigid molecules were performed by the authors.

It turns out that pressure-induced phase transitions occur only in systems with high degree of one-dimensional character. With increasing pressure, the molecules are placed closer together which implies the increase in the repulsive interactions between the molecular pair. This involves instability which produces the pressure-induced transition. Then the molecules undergo an orientational rearrangement within the stacks moving closer to orthogonality with the stack axis. In this way the spacing between molecular planes increases.

4.3 Murnaghan equation of state

The thermodynamic state of a system is completely defined when one of the thermodynamic potentials is expressed as function of its canonical variables. The equation of state is then obtained from the study of the first derivatives of the thermodynamic potential. The thermodynamic potentials most often used are Gibbs G and Helmholtz F free energies because they have easily measurable canonical variables: $\{T, p, N\}$ and $\{T, V, N\}$, respectively, where T is the temperature, p the pressure, V the volume and N the number of particles. However, for complex solids, like the oxadiazole crystals, it is not possible to specify the correct form of the inter-atomic potential, and therefore of the Gibbs and Helmholtz functions. For this reason the experimental data are usually adjusted to an empirical equation of state relating V, p, and T; the number of particles N is normally constant.

Since temperature has much less effect for solids than for gases, the behaviour of solids is often described by an isothermal equation of state relating p and V. The temperature effect is then introduced as a thermal expansion correction to the equation. The equations of state are normally parameterized in terms of the zero-pressure moduli, K_0 (the value of the bulk modulus, K, at $p = 0$) and K_0' (the value of the pressure derivative of the bulk modulus at $p = 0$).

The stiffness or incompressibility of a solid is characterized by its isothermal bulk modulus (K_T, henceforth denoted K for simplicity), defined as [83]:

$$K = -\left(\frac{\partial p}{\partial \ln V}\right)_T \tag{4.1}$$

The most frequently used equation of states are [83]:

(i) Murnaghan equation of state:

$$p = \frac{K_0}{K_0'}\left[\left(\frac{V_0}{V}\right)^{K_0'} - 1\right] \tag{4.2}$$

(ii) second order Birch-Murnaghan equation of state, where K_0'=4:

$$p = \frac{3K_0}{2}\left[\left(\frac{V_0}{V}\right)^{7/3} - \left(\frac{V_0}{V}\right)^{5/3}\right] \tag{4.3}$$

(iii) third order Birch-Murnaghan equation of state*:

$$p = \frac{3K_0}{2}\left[\left(\frac{V_0}{V}\right)^{7/3} - \left(\frac{V_0}{V}\right)^{5/3}\right]\left\{1 + \frac{3}{4}\left(K_0' - 4\right)\left[\left(\frac{V_0}{V}\right)^{2/3} - 1\right]\right\} \tag{4.4}$$

*Note that the third order Birch-Murnaghan equation of state (eq. (4.4)) reduces to the second order Birch-Murnaghan equation of state (eq. (4.3)) when K_0'=4.

In the present work we use the Murnaghan equation of state (MEOS) to describe our experimental results. The MEOS reproduces well the p-V data and yields correct values of K_0 and K_0' for small compressions [122].

The MEOS can be derived from the assumption that K varies linearly with pressure:

$$K = K_0 + K_0' p \tag{4.5}$$

K_0' being independent of pressure.

Substituting eq. (4.5) in eq. (4.1), we obtain the following differential equation (T is constant):

$$-\,\mathrm{d}\ln V = \frac{\mathrm{d}p}{K_0 + K_0' p} \tag{4.6}$$

Introducing the variable $u = K_0 + K_0' p$, in eq. (4.6), we get ($\mathrm{d}u = K_0' \,\mathrm{d}p$):

$$-\,\mathrm{d}\ln V = \frac{1}{K_0'}\frac{\mathrm{d}u}{u} = \frac{1}{K_0'}\,\mathrm{d}\ln u \tag{4.7}$$

This equation can be directly integrated between $p = 0$ ($u = K_0$) and $p = p'$ ($u = K_0 + K_0' p'$):

$$-\ln\left(\frac{V}{V_0}\right) = \frac{1}{K_0'}\ln\left(\frac{K_0 + K_0' p'}{K_0}\right) \tag{4.8}$$

Taking exponentials, rearranging the terms and renaming p' with p, we obtain the MEOS:

$$p = \frac{K_0}{K_0'}\left[\left(\frac{V_0}{V}\right)^{K_0'} - 1\right] \tag{4.9}$$

4.4 Phase transitions

The first question which arises in the study of a crystal under compression is whether it undergoes phase transitions or not. The change of the space group associated with a phase transition modifies the diffraction pattern by the introduction of new peaks, associated with new reflection planes, and/or by the disappearance of others. Therefore, we began the high pressure structural study of the crystals with the comparison of their X-ray patterns at different pressures. In all cases except that of 6DPO4 which is described below, no significant differences were found. Thus, it is concluded that the investigated crystals except 6DPO4 do not undergo phase transitions in the pressure range investigated (up to approximately 5 GPa). To visualize this we show in fig. 4.3 the diffractograms of DPO I at the first and last step of the compression. As can be observed, there are no significant changes in the shape of the diffractogram, just modifications attributable to an increased texture with pressure. Besides, a general decrease in the intensity under compression occurs. This is principally due to the approximation of the anvils and hence the decrease of the radiation which pass through the sample but possibly also to a slight increase of the amorphous content. Such an enhance of the amorphous component of the sample could also be concluded from the Raman investigation at high pressure (see §8.4). The general shift of the X-ray pattern with pressure is associated with the decrease of the lattice parameters. Additionally, there are no discontinuities in the shift of the Raman lattice modes under compression supporting the statement of absence of pressure-induced phase transitions as is discussed in §8.4.

It is noteworthy that despite the fact that DPO shows two crystal structures at normal conditions (see §3.4.1 and §3.4.2) and DPO I undergoes a phase transition into DPO II under heating (as is explained in the next chapter, §5.4.1), neither DPO I nor DPO II suffer phase transitions under compression.

Associated with the question of the presence of phase transitions is another one which refers to the reversibility of the compression process. To answer this question, the pressure was unloaded

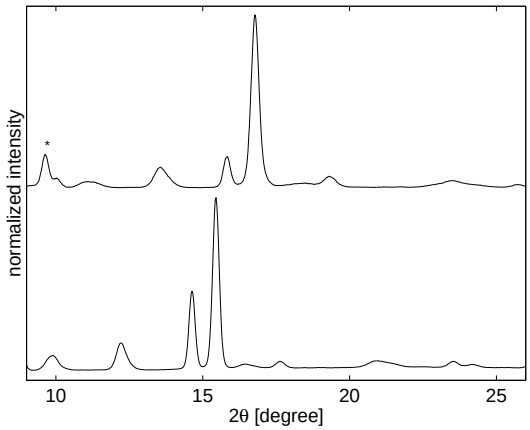

Fig. 4.3: X-ray diffraction pattern of DPO I at 0 GPa before the compression (bottom) and at 4.8 GPa at the end of the compression (top). The peak marked with $*$ is an escape peak due to the detector material (Ge). There are no significant differences between the patterns indicating the absence of phase transitions under compression. The only difference is the shift of the peaks due to the decrease of the lattice parameters.

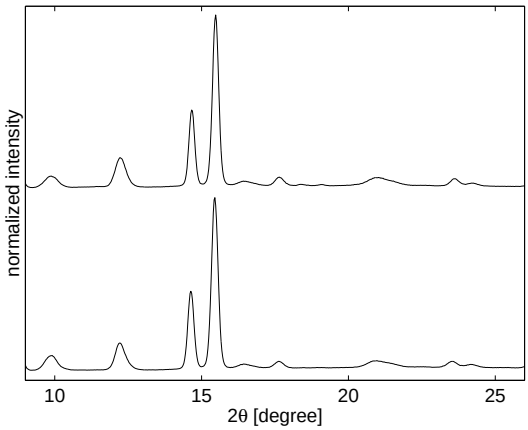

Fig. 4.4: X-ray diffraction pattern of DPO I at 0 GPa before the compression (bottom) and at 0.2 GPa after the compression (top). The similarity between the patterns indicates the reversibility of the compression.

after the compression run and a diffraction pattern of the relaxed sample was acquired. The comparison of the patterns for the initial and the unloaded sample indicates that the compression is reversible for all the investigated crystals with the exception of 6DPO4. Moreover, no hysteresis was found, again with the exception of 6DPO4. Figure 4.4 shows this for DPO I. The pressure at the relaxation point amounted to 0.1 or 0.2 GPa, depending on the sample. A total relaxation could not be achieved due to the presence of stress in the sample, within the closed cell. As we comment below, this might be the reason of the apparent irreversibility of the phase transitions in 6DPO4.

4.4.1 6DPO4

As is indicated above, the only oxadiazole crystal investigated here which performs pressure-induced phase transitions is 6DPO4. The analysis of the X-ray patterns reveals that important changes occur. Some peaks disappear while new ones appear and other ones split. Figure 4.5 shows two diffractograms of 6DPO4 at 0 and 2.4 GPa. Besides the shift of the pattern to larger 2θ values, which is due to the decrease of the inter-planar distances, we can observe the following. The intense peak located at 2θ=11.2° at ambient pressure, disappears nearly completely at higher pressures. The rather intense peak at 2θ=17.6° as well as the small peak close to it, at 2θ=18.8°, only exist at ambient pressure. These modifications imply changes in the symmetry of the crystal, that is, phase transitions. After release of pressure, the X-ray patterns do not get back to the virgin structure. Figure 4.6 shows this *apparent* irreversibility of the phase transitions. However, the Raman spectrum of the fully relaxed sample clearly indicates the reversibility of the transitions (see §8.4.1). We believe that this *apparent* irreversibility is just the result of the incomplete relaxation of the sample. As is pointed out above, the full relaxation is not possible in the X-ray diffraction experiments due to the experimental conditions. Since the first phase transition occurs at relatively low pressure, it may be true that the relaxed sample still bears its structure.

For a clearer visualization of this, we reproduce the inter-planar distances as function of pre-

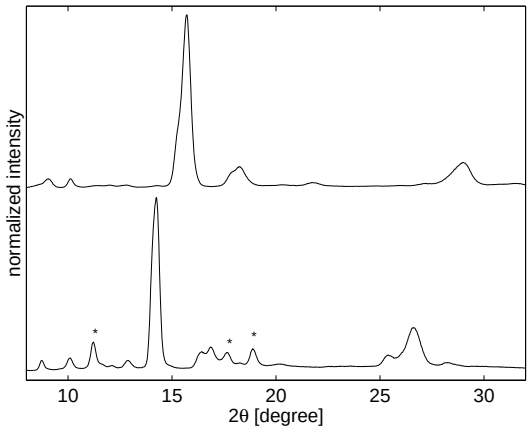

Fig. 4.5: X-ray diffraction pattern of 6DPO4 at 0 GPa before the compression (bottom) and at 2.4 GPa after the phase transition (top). There are significant differences between the patterns indicating the occurrence of phase transitions under compression.

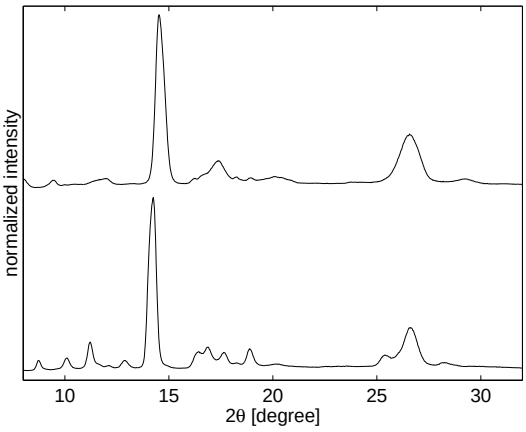

Fig. 4.6: X-ray diffraction pattern of 6DPO4 at 0 GPa before the compression (bottom) and at 0.2 GPa after the compression (top). The differences between the patterns indicate the irreversibility of the compression.

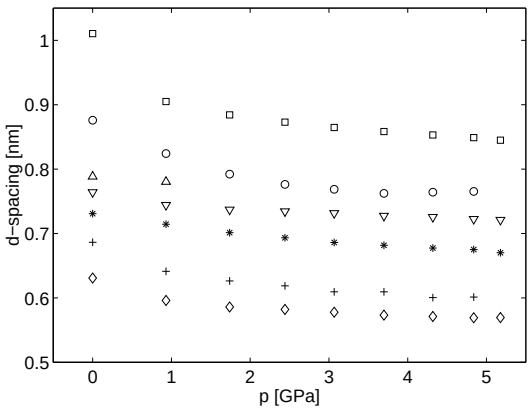

Fig. 4.7: Long inter-planar spacings of 6DPO4 under compression.

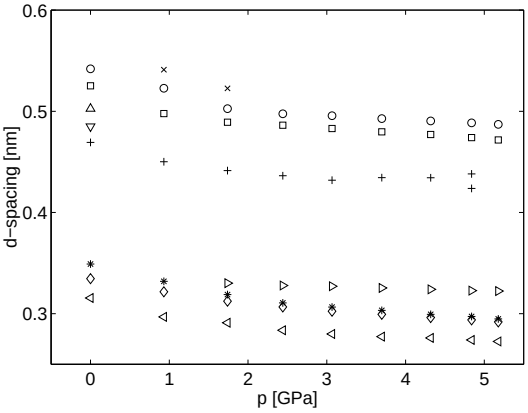

Fig. 4.8: Short inter-planar spacings of 6DPO4 under compression.

ssure in fig. 4.7 and 4.8. The changes with pressure of the X-ray patterns are:

(i) The peak marked '△' in fig. 4.7, which represents the family of planes (011) with d=0.789 nm and 2θ=11.2° at ambient pressure, only exists in the first two compression steps, that is, up to 0.9 GPa. This can also be seen in fig. 4.5.

(ii) A new peak exists in the range 0.9 to 1.7 GPa. It is represented by '×' in fig. 4.8 and corresponds to inter-planar distances about 0.541 nm and 2θ values around 16.4°, at 0.9 GPa.

(iii) In the first compression step, 0 to 0.9 GPa, the family of planes $(\bar{2}11)$, with d=0.503 nm and 2θ=17.6° at ambient pressure, disappears. It is marked with '△' in fig. 4.8.

(iv) Also in the first compression step, another peak disappears: that corresponding to the planes $(\bar{1}12)$, which has d=0.485 nm and 2θ=18.3° at ambient pressure. It is the peak '▽' in fig. 4.8.

(v) After 1.7 GPa the peak marked with '∗' in fig. 4.8, which characterizes the family of planes $(\bar{3}11)$, located at ambient pressure at 2θ=25.5° and with d=0.349 nm, splits into the intense and sharp peak '∗' and the small and broad peak '▷'.

(vi) Nearly at the end of the compression, another peak splits, that corresponding to the family of planes (210). It is marked with '+' in fig. 4.8. At ambient pressure this peak is located at 2θ=18.9° and has a spacing of d=0.469 nm.

As we see, there are important changes in the diffraction patterns as well between 0 and 0.9 GPa as between 0.9 and 1.7 GPa and between 1.7 and 2.4 GPa. Therefore, 6DPO4 may undergo several phase transitions. Since the quality of the energy dispersive patterns is not high enough, the structure of the high pressure phases could not be resolved. However, the phase transitions of 6DPO4 are thought to be topotactical reactions similar to those described by Orgzall et al. for 1DPO1 [63] (cf. 4.2.1). The close molecular packing of 6DPO4 characterized by stacks of infinite π-complexes (cf. §3.4.5), may not allow large movements of the molecules. The evolution of the absorption and emission spectra of the crystal under compression supports this idea. In order to verify the previous hypothesis, single X-ray diffraction under compression should be performed in the future.

4.5 Method to determine the lattice parameters

For the evaluation of the energy dispersive powder diffractograms we used the program Powder Cell 2.3 [123]. The experimental diffraction patterns were fitted to the theoretical pattern which results from the structure determination of a single crystal at ambient pressure. The quality of the energy dispersive X-ray diffraction patterns did not allow the performance of a crystal structure determination at high pressures.

Powder Cell 2.3 offers a specific resource to fit *powder* diffraction patterns. Through this option, the intensities of the different peaks are varied individually to neglect the influence of the powder technique. Although the crystals were always investigated in powder form, their needle-like (DPO I, 6DPO6 II) and plate-like (DPO II, 7PO3) habits could imply an increasing texture under high pressure conditions. This characteristic of the substances makes such procedure particularly useful because the presence of texture induces additional changes in the relative intensity of peaks associated with different planes.

It should be remarked that from this approach only information about the *lattice parameters*, and not about crystal symmetry or atom positions, can be achieved. The crystal symmetry was supposed to remain that of the ambient pressure structure. If changes in the symmetry appear, that is, if a phase transition occurs, the fit is not possible. As is commented in the previous section, modifications of the crystal symmetry can be easily detected since they involve drastic

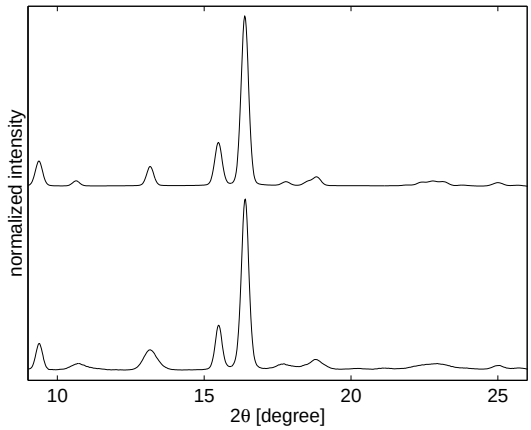

Fig. 4.9: Experimental X-ray diffraction pattern of DPO I at 2.5 GPa (bottom) and its fit (top). Nearly no differences appear between the two curves indicating the quality of the fit.

changes in the diffraction pattern. However, small variations of the crystal packing induced by slight rotations and translations of the molecules, without symmetry modification, were proved to preserve the structure of the *powder* X-ray pattern. Thus, slight changes in the relative orientation of the molecules, such as the enlargement of the herring bone angle of biphenyl found by Puschnig et al. [115] (cf. §4.2.2) or the increased approximation to orthogonality of anthracene derivatives with the stack axis with pressure reported by Brillante et al. [88, 89, 90, 91, 92] (cf. §4.2.3), cannot be excluded. Since such small modifications of the molecular arrangement are not taken into account in the model of Powder Cell, they will be carefully considered *a posteriori* for each particular crystal (see §4.6).

Additionally, in the fit procedure the *rigid body* approximation was used. This implies that the conformation of the molecule is assumed to remain constant. The rigid body approximation suits well the behaviour of compounds with a delocalized π electron system along the whole molecule such as the oxadiazole compounds. Due to this observation, we performed a new analysis of the results of Orgzall et al. concerning 1DPO1 [63] and found that its molecular conformation in the different phases is nearly maintained (deviation from planarity: 10°...6° and maximal modification of the inter-ring bonds of 0.005 nm). We believe that those changes in the molecular conformation of the oxadiazole compounds which are the object of the present work may be similar to those of 1DPO1. Moreover, molecules which show a higher planarity at ambient pressure than 1DPO1 (all the ones investigated here except 6DPO6 I) are even more rigid, justifying the rigid-body approximation.

Figure 4.9 shows an example of the results for DPO I at 2.5 GPa fitted with Powder Cell. The small difference between the experimental and the approximated curve may be explained by the influences of the gasketing epoxy cube and of the detector (escape peaks of Ge and fluorescence lines of In) [124]. The precision of the determination of the lattice parameters determination from Powder Cell is estimated to 0.005 nm. Of course, the resulting error in the lattice parameters also depends on the quality of the experimental pattern. Some substances show peaks which are difficult to resolve. Additional disturbances come from the device (see §2.2.2). Since the estimation of the total error is a complex issue, we decided not to give error bars for our results.

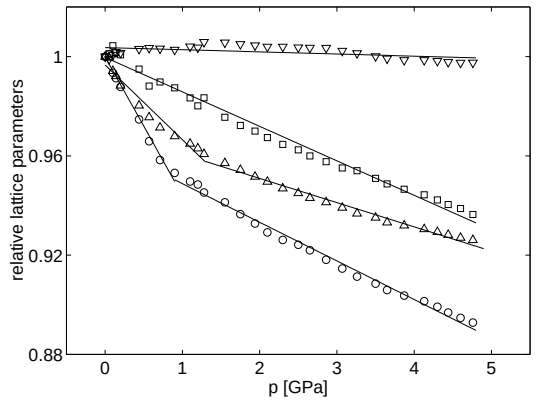

Fig. 4.10: Relative lattice parameters of DPO I under compression (□ a/a_0, ◯ b/b_0, △ c/c_0, ▽ β/β_0). The lines correspond to the fits described in the text.

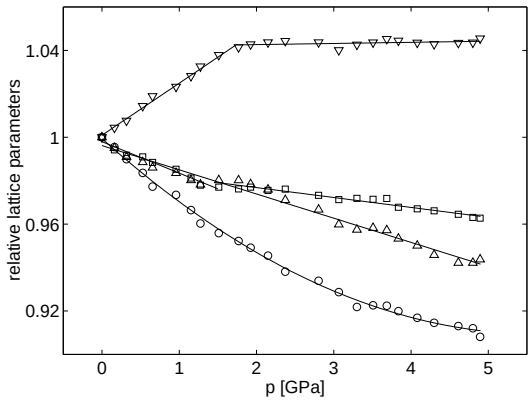

Fig. 4.11: Relative lattice parameters of DPO II under compression (□ a/a_0, ◯ b/b_0, △ c/c_0, ▽ β/β_0). The lines correspond to the fits described in the text.

4.6 Lattice parameters at high pressure

4.6.1 DPO I

Figure 4.10 shows the relative decrease of the lattice parameters for DPO I in the pressure range investigated[†]. The stack-like arrangement of the molecules in the crystal induces the anisotropic response of DPO I to compression. To characterize the compressibility of the axes, the experimental data were approximated in a piecewise linear manner (fig. 4.10). The results obtained are:

$$\begin{array}{lrcll} \text{DPO I}: & a/a_0 & = & 1.000 - 0.014p & p \in [0, 4.8]\ \text{GPa} \\ & b/b_0 & = & 1.000 - 0.056p & p \in [0, 0.9]\ \text{GPa} \\ & b/b_0 & = & 0.964 - 0.016p & p \in [0.9, 4.8]\ \text{GPa} \\ & c/c_0 & = & 0.997 - 0.030p & p \in [0, 1.3]\ \text{GPa} \\ & c/c_0 & = & 0.970 - 0.010p & p \in [1.3, 4.8]\ \text{GPa} \\ & \beta/\beta_0 & = & 1.004 - 0.001p & p \in [0, 4.8]\ \text{GPa} \end{array}$$

The crystal packing of DPO I is characterized by the presence of stacks (see §3.4.1). The arrangement of the molecules along the stacks is determined by π-π interactions between the oxadiazole (π-acceptor) and the phenyl rings (π-donors). Slight rotations or translations of the molecules of a stack would lead to the destabilization and break of the π-complexes and hence to important changes in the crystal packing. Thus, we propose that the π-complexes and the stack arrangement are maintained during the compression. Otherwise a phase transition would occur. The only movements which are allowed in these crystals are translations of the stacks as a whole and the parallel approach of the molecules of a stack.

Following the model in which the stack arrangement is preserved, the compression rates of the lattice parameters give an insight into the compression process. Since β is nearly maintained, the only significant modifications of the unit cell are those of the cell axes. To facilitate the understanding of the compression process explained below, see fig. 3.1 of the crystal structure of DPO I.

[†]The experimental lattice parameters at high pressure of all the investigated compounds are summarized in tables D.1 to D.5

The stack axis, a, is the least compressible one (linear compressibility[‡], 0.014 GPa^{-1} in the whole pressure range). The shortening of a implies the compression of the stacks, that is, the approximation of the molecules which form the π-complexes. This is difficult because the electron density between the molecules which build a π-complex is high, inducing a strong electrostatic repulsion. Thus, from the compression behaviour of a, it can be concluded that the potential well which describes the π-π interactions of the π-complexes has a steep slope for shorter distances between molecules.

The second to least compressible axis is c. To describe the bend in the compression of c which appears after approximately 1.3 GPa, the pressure range was divided into two intervals. The bend informs about the increased difficulty in the compression of c when the molecules are brought close enough together. At the beginning of the compression the molecules of different stacks interact principally through weak H-bonds and can be joined together relatively easy. But when the stacks are close enough, the electrostatic repulsion becomes large and induces the decrease of the compressibility. Although the electron density between molecules of adjacent stacks is not large—the π systems of the π-complexes are oriented perpendicular to c—the spacings are so short that the forces may be intense.

A similar, even more pronounced, response to pressure is exhibited by b, which is the most compressible axis. In this case, we also divided the pressure range into two intervals. In the first interval (up to 0.9 GPa) the linear compressibility of b is very large (0.056 GPa^{-1}). After 0.9 GPa its compression becomes more difficult as is indicated by the decrease of the value of the linear compressibility (0.016 GPa^{-1}). We propose the following explanation for the compression behaviour of b. At the beginning of the compression the stacks can be easily joined together along b (fig. 4.12(a) and 4.12(b)). The low electron density between adjacent stacks allows this. Since the molecules just interact via the end part of the phenyl rings, the electron density between adjacent stacks along the b-direction is lower than those between adjacent stacks in c-direction. This explains why the linear compression coefficient of b in the first pressure steps is larger than that of c (0.056 and 0.030 GPa^{-1}, respectively). Around 0.9 GPa the easy translation of the stacks ceases because the spacings are so short that the electrostatic repulsion is large. After this point the compression of the stacks themselves becomes more important (fig. 4.12(b) and 4.12(c)). Taking into account the molecular arrangement within the π-complexes, it can be concluded that the π-π forces are principally perpendicular to the molecular planes (fig. 4.13). The characteristics of the crystal structure of DPO I (π-complexes contained in planes parallel to the ab-plane; herring bone angle, 41°; γ=90°) imply that these π-π interactions have nearly the same component along a as along b. Thus, the forces which act against the compression of a and b after 0.9 GPa should be rather similar, which explains the similarities in the linear compressibilities of both axes after 0.9 GPa (0.014 and 0.016 GPa^{-1}, for a and b, respectively). The differences between these values originate in the influence of other forces along the b-direction such as the electrostatic repulsion between the stacks and in the deviation of the herring bone angle from 45°. As we outline in fig. 4.13, the compression of the stacks induces the modification of the herring bone angle. The stacks begin their compression already at the first pressure step to allow the decrease of the length of a.

4.6.2 DPO II

The X-ray pattern of DPO II shows some groups of peaks close to each other (see fig. 2.3). The lack of high resolution of the energy dispersive technique, as pointed out in §2.2.2, reduces somewhat the quality of the high pressure diffractograms and therefore of their fits. The behaviour of the lattice constants of DPO II under compression up to 4.9 GPa is shown in fig. 4.11. The compression of the axes and the monoclinic angle can be described by the following relations:

[‡]The linear compressibility of an axis is defined as the ratio of the relative decrease in the axis length to pressure.

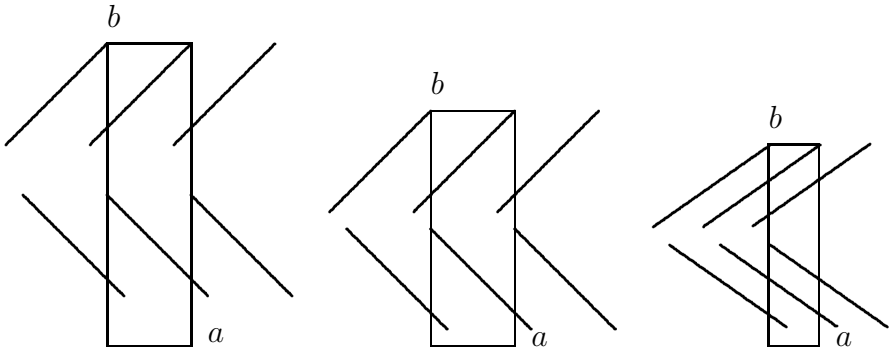

(a) p=0 GPa. (b) p=0.9 GPa. (c) p=4.8 GPa.

Fig. 4.12: Schematic diagram of the compression mechanism of DPO I. For a less schematic figure of (a) see fig. 3.1(b). From (a) to (b) the two stacks approach each other; from (b) to (c) the stacks are compressed internally which induces the decrease of the herring bone angle. The strong exaggeration of the effect implies the break of the symmetry in (c), which in reality does not occur.

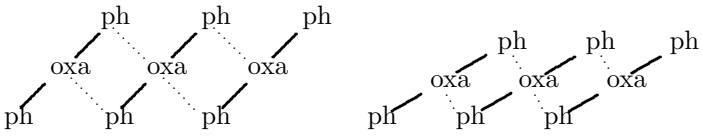

(a) Non compressed stack. (b) Compressed stack.

Fig. 4.13: Schematic diagram of the compression mechanisms of the stacks of DPO I. The conservation of the π-complexes and of the symmetry induces the tilting of the molecules (decrease of the herring bone angle). The effect is strongly exaggerated.

$$
\begin{array}{lllll}
\text{DPO II}: & a/a_0 & = & 0.998 - 0.015p & p \in [0, 1.5] \text{ GPa} \\
& a/a_0 & = & 0.986 - 0.005p & p \in [1.5, 4.9] \text{ GPa} \\
& b/b_0 & = & 0.999 - 0.032p + 0.003p^2 & p \in [0, 4.9] \text{ GPa} \\
& c/c_0 & = & 0.996 - 0.011p & p \in [0, 4.9] \text{ GPa} \\
& \beta/\beta_0 & = & 1.001 + 0.024p & p \in [0, 1.8] \text{ GPa} \\
& \beta/\beta_0 & = & 1.042 + 0.001p & p \in [1.8, 4.9] \text{ GPa}
\end{array}
$$

It is a remarkable fact that β strongly increases up to 1.8 GPa and then nearly does not vary. This step-wise variation of β corresponds well with the decrease, also in two steps, of a.

An analogous reasoning to the one discussed above for DPO I leads to the conclusion that the only possible movements in DPO II crystals are translations of the entire stacks and hence also of the layers as a whole, as well as the parallel approximation of the molecules within a stack. At this point it is worthwhile to take one step back and look even more closely at the molecular packing of DPO II at *ambient* pressure. The interaction of molecules of different layers—the layers are perpendicular to c—remind us of those found for adjacent stacks along the axis c of DPO I (weak H-bonds between the CH groups of the phenylene rings and the N atoms of the oxadiazole unit, see §3.4.1 and §3.4.2). When pressure increases, the molecules approach laterally and the electrostatic repulsion should become larger as occurs in DPO I. Therefore, a similar behaviour of the axes c of DPO I and DPO II is expected. As we pointed out above, unfortunately, the quality of the fits of DPO II is lower than that for the other substances due to the characteristics of the X-ray pattern of this crystal and to the limitations of the energy dispersive technique. This causes the dispersion of the values found for the length of c in DPO II (fig. 4.11). Thus, the comparison of the compression laws of the relative decrease of c for DPO I and DPO II may only be done taking into account this limitation. However, it is significant to note that the linear compressibility of c of DPO I after 1.3 GPa (0.010 GPa^{-1}) is nearly identical to that found for c of DPO II in the whole pressure range (0.011 GPa^{-1}). Besides, the relative length of both axes at the end of the compression are very similar (0.926 for DPO I and 0.942 for DPO II at 4.8 GPa, tables D.1 and D.2). These similarities give support to our analogy between the behaviour of axes c of these two substances. The reasons for the differences between the compression of these axes in the first pressure steps are not clear.

The arrangement of the molecules within a layer in stacks perpendicular to each other is such, that the axes a and b of the unit cell are expected to behave in the same way. The π-π interactions between the molecules of the two sets of stacks are oriented along a and b, respectively. Additionally, the weak van der Waals forces which act between the stacks are also equal in both directions. But the non-maintenance of β under compression disturbs the expected similarity. As we indicated above, β suffers a strong linear increase up to 1.8 GPa and after this value remains nearly constant. An increment in the monoclinic angle produces the approximation of the stacks. It also reduces the those molecules (within a stack) which are perpendicular to a (fig. 4.14). For this reason the decrease of the length of a up to approximately 1.5 GPa is not as large as the one suffered by b. Beyond this value of pressure, β remains nearly constant and a decreases only slightly. The molecules perpendicular to a are so close together that the electrostatic repulsion between the components of the π-complexes prevents the compression of a as well as any further increase of β.

4.6.3 6DPO6 I

The crystal 6DPO6 I (as well as 6DPO6 II) belongs to the orthorhombic crystal system, where $\alpha = \beta = \gamma = 90°$, which facilitates the discussion of the compression of the unit cell axes. The relative decrease of the cell axes of 6DPO6 I up to 4.9 GPa at room temperature is shown in fig. 4.15. The values of the cell axes at high pressure were approximated by the following laws:

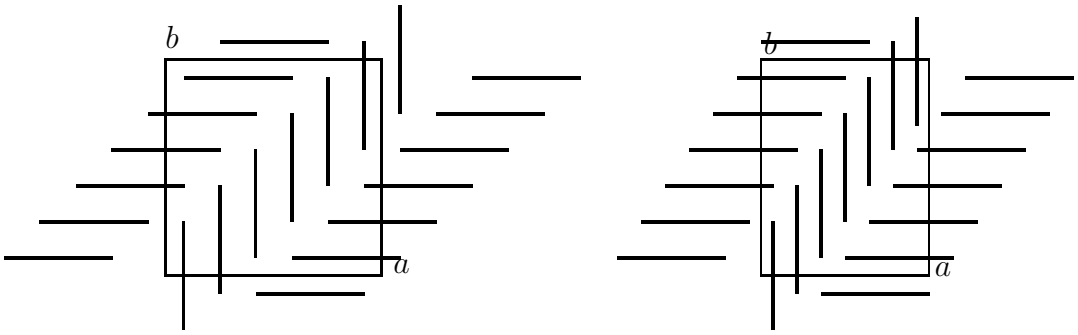

(a) p=0 GPa. (b) p=1.8 GPa.

Fig. 4.14: Schematic diagram of the compression mechanism of DPO II showing the effect of the increase of β. For a less schematic figure of (a) see fig. 3.3(b).The effect is strongly exaggerated.

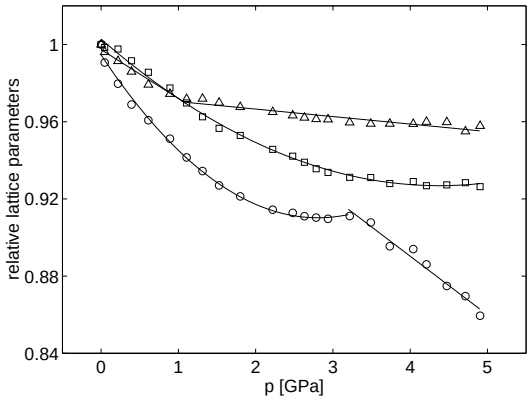

Fig. 4.15: Relative lattice parameters of 6DPO6 I under compression ($\square\, a/a_0$, $\bigcirc\, b/b_0$, $\triangle\, c/c_0$). The lines correspond to the fits described in the text.

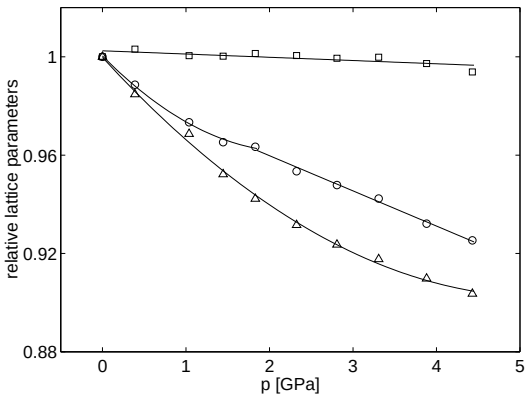

Fig. 4.16: Relative lattice parameters of 6DPO6 II under compression ($\square\, a/a_0$, $\bigcirc\, b/b_0$, $\triangle\, c/c_0$). The lines correspond to the fits described in the text.

$$
\begin{array}{lrcll}
\text{6DPO6 I}: & a/a_0 & = & 1.003 - 0.035p + 0.004p^2 & p \in [0, 4.9]\ \text{GPa} \\
& b/b_0 & = & 0.995 - 0.060p + 0.011p^2 & p \in [0, 3.2]\ \text{GPa} \\
& b/b_0 & = & 1.012 - 0.030p & p \in [3.2, 4.9]\ \text{GPa} \\
& c/c_0 & = & 0.997 - 0.025p & p \in [0, 1.1]\ \text{GPa} \\
& c/c_0 & = & 0.974 - 0.004p & p \in [1.1, 4.9]\ \text{GPa}
\end{array}
$$

For DPO I and DPO II, we proposed that the molecular arrangement is maintained owing to the strong π-π interactions which build the π-complexes. However, in the case of 6DPO6 I, slight rotations and translations of the molecules may occur, of course, preserving the crystal symmetry, but not the molecular arrangement. The inter-molecular interactions within a stack are not as strong as those found in the π-complexes of DPO I and DPO II and may allow such movements (see §3.4.3).

The stack axis, b, is the most compressible one. Its response to compression is well described by dividing the pressure range into two intervals. In the first interval (up to 3.2 GPa) the length of b decreases with a quadratic law in pressure, which adjusts properly the saturation of the compression in the range 2.2 to 3.2 GPa. In the second range (3.2 to 4.9 GPa), a linear fit

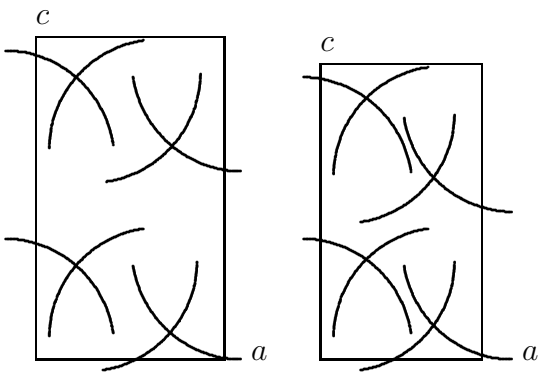

(a) p=0 GPa. (b) p=3.2 GPa.

Fig. 4.17: Schematic diagram of the compression mechanism of 6DPO6 I. For a less schematic figure of (a) see fig. 3.4(a). The effect of the displacement of the molecules in the plane perpendicular to the stack axis is shown. The effect is strongly exaggerated.

describes well the high compressibility of b. Since the 6DPO6 molecules pack in such a way that the π-π interaction along a stack only occurs between the oxadiazole rings, the stack axis has a great compressibility. The saturation of the compression between 2.2 and 3.2 GPa and its posterior linear increase can be explained by the following hypothesis. The compression of b proceeds without large resistance up to a point where the arrangement between molecules induces strong π-π interactions. The compression of the stack axis is thought to be accompanied by an increase in the overlap between the π systems of the oxadiazole units. As a result, an important electrostatic repulsion between the π systems of the oxadiazole units of adjacent molecules appears. The overlap is thought to be maximal in the interval 2.2 to 3.2 GPa where the compression along b is saturated. At this point, around 3.2 GPa, the great repulsion between the electronic π systems induces the decrease of the overlap of the oxadiazole units by the displacement of the molecules in the plane perpendicular to b (fig. 4.17). The first consequence of this lateral displacement is the important increase of the compressibility of b. A second consequence is the saturation of the compression along the other two axes. Although consistent with the measurements, this explanation remains a hypothesis since it cannot be proved with the present high pressure X-ray analysis; Single crystal high pressure diffraction or molecular modelling would be required.

The other two axes (a and c) are significantly less compressible. After a given point, they nearly become their incompressible. For a, the pressure interval where the saturation appears coincides with the range where the compressibility of the stack axis levels off and then strongly increases again. The axis c is the least compressible one due to the presence of H-bonds between the NH_2 group and the N atom of the oxadiazole ring of molecules of neighbouring stacks. The pressure range where the collapse of the c compressibility appears, begins already at 1.1 GPa. It is thought that at this pressure the stacks are already very close together. Having observed the saturation of the compressibilities of a and c, we can now add to our hypothesis of the previous paragraph that the lateral shift of the molecules of a stack occurs in the a-direction.

4.6.4 6DPO6 II

The water containing crystals 6DPO6 II show a strong anisotropical behaviour under compression (fig. 4.16). The pressure dependence of the different axes is as follows:

$$
\begin{array}{lllll}
\text{6DPO6 II}: & a/a_0 & = & 1.002 - 0.001p & p \in [0, 4.4]\ \text{GPa} \\
& b/b_0 & = & 1.000 - 0.034p + 0.008p^2 & p \in [0, 1.8]\ \text{GPa} \\
& b/b_0 & = & 0.988 - 0.014p & p \in [1.8, 4.4]\ \text{GPa} \\
& c/c_0 & = & 1.000 - 0.037p + 0.004p^2 & p \in [0, 4.4]\ \text{GPa}
\end{array}
$$

An look at the crystal packing of 6DPO6 II shows that the interactions between layers and between the rows of a layer are van der Waals forces and weak H-bonds (cf. §3.4.4). The molecules which build a row are connected by *strong* H-bonds through the water molecules. That is why we believe that the rows are maintained during the compression. Then the only allowed movements are translations of the layers and of the rows inside a layer without modification of the crystal symmetry.

The anisotropical compression results from the differences among the forces which hold the molecules together. The strong H-bonds between the water molecules and the NH_2 groups of the 6DPO6 molecules are responsible for the extremely weak compressibility of a (0.001 GPa^{-1}). Such a stiffness of a unit cell axis was not found in any of the other oxadiazole compounds studied here.

The next least compressible axis is b. For the description of the compression of this axis, the pressure range was again divided into two intervals. In the first interval (up to 1.8 GPa) a polynomial of second order was chosen to reproduce the strong decrease of the axis length in the first steps of the compression and the apparent saturation around 1.8 GPa. Beyond this value of pressure, a linear decrease is observed. In the compression of b two different forces are involved: weak H-bonds and van der Waals interactions.

The most compressible axis of 6DPO6 II is c, which is perpendicular to the layers. In this structure no overlap between molecules of adjacent stacks occurs. Consequently, the electrostatic repulsion is not as strong as within the π-complexes of other oxadiazole compounds and therefore the compressibility of c does not show a noticeable saturation.

4.6.5 7PO3

The relative decrease of the lattice parameters of 7PO3 is shown in fig. 4.18. The experimental values are reasonably reproduced by the following fits:

$$
\begin{array}{lllll}
\text{7PO3}: & a/a_0 & = & 1.005 - 0.015p + 0.001p^2 & p \in [0, 4.1]\ \text{GPa} \\
& b/b_0 & = & 0.998 - 0.040p + 0.005p^2 & p \in [0, 4.1]\ \text{GPa} \\
& c/c_0 & = & 0.995 - 0.065p + 0.011p^2 & p \in [0, 2.9]\ \text{GPa} \\
& c/c_0 & = & 0.956 - 0.021p & p \in [2.9, 4.1]\ \text{GPa} \\
& \beta/\beta_0 & = & 0.999 - 0.015p + 0.001p^2 & p \in [0, 4.1]\ \text{GPa}
\end{array}
$$

The molecular arrangement of 7PO3 is determined by the existence of pairs of molecules connected by strong π-π interactions (cf. §3.4.6). Similarly as for DPO I and DPO II, small turns or shifts of the molecules of a pair would induce the destabilization and break of the π-complexes. This would lead to important changes in the crystal packing which should be reflected in the X-ray patterns. Thus, we believe that the pairs of 7PO3 are maintained during the compression. However, the relative orientation of the pairs within a layer may slightly change. Since the interactions between pairs are not very strong, they are easily movable. Modifications of the layer arrangement are not expected because this would probably lead to changes in the crystal symmetry, i.e. to phase transitions, which are not observed.

The variation of β induces a slight increase in the interactions of molecules of different pairs which are adjacent along c. The principal effect of this is the increased resistance to compression of c. This is discussed below in more detail (cf. fig. 3.8 for a better understanding of the compression process of 7PO3).

The least compressible axis of the unit cell is a. This fact informs about the large difficulty in joining the layers together due to the repulsion among $N(CH_3)_2$ and the CH_3 groups of molecules

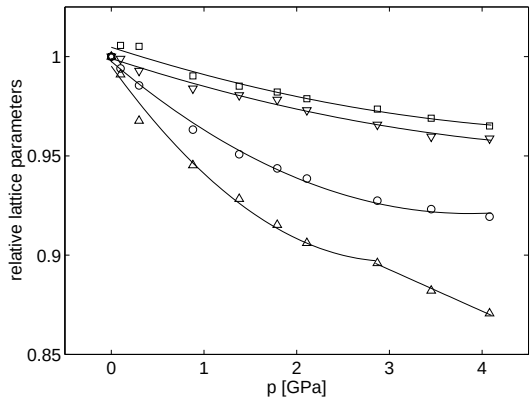

Fig. 4.18: Relative lattice parameters of 7PO3 under compression ($\square a/a_0$, $\bigcirc b/b_0$, $\triangle c/c_0$, $\triangledown \beta/\beta_0$). The lines correspond to the fits described in the text.

of different layers. The axis b is rather compressible because of the large lateral distance between the molecules of a layer and the absence of strong forces. After approximately 2.9 GPa, the compression of b suffers a saturation.

Finally, c shows a large compressibility. In order to achieve a better adjustment of the experimental data, the pressure range was divided into two intervals. A possible explanation to the step-wise compression behaviour and to the large compressibility values of c follows. At the beginning of the compression, up to 2.1 GPa, the pairs of 7PO3 molecules easily approximate each other then the distance between two pairs along c is large. In the pressure range between 2.1 and 2.9 GPa the compression of c becomes more difficult because the pairs are already very close to each other. Additionally, the decrease of the monoclinic angle induces an increase in the overlap between different pairs and therefore an increase in the electrostatic repulsion between pairs. This contributes to a slight reduction of the compression of c. At around 2.9 GPa the pairs cannot approximate closer and they slightly shift laterally along b relative to each other. In this way the overlap between the molecules of adjacent pairs decreases which favors the further compression of c. Again, due to the limitation of the energy dispersive x-ray diffraction pattern, single crystal angle dispersive diffractogram or the realization of a molecular modeling calculation would be needed to further investigate the present hypothesis. Nevertheless, the compression behaviour of b supports the hypothesis. Above 2.9 GPa the compression of b nearly stops. The lateral displacement of the pairs relative to each other should be responsible for this.

4.7 Volume at high pressure

From the knowledge of the lattice parameters at every pressure step value, the determination of the volume of the unit cell is directly obtained. The volume decrease as a function of pressure is shown in fig. 4.19, 4.20 and 4.21 for the studied crystals at room temperature and up to approximately 5 GPa. A good description of the the experimental data is provided by the MEOS (eq. (4.2)) with the following values for K_0 and K_0':

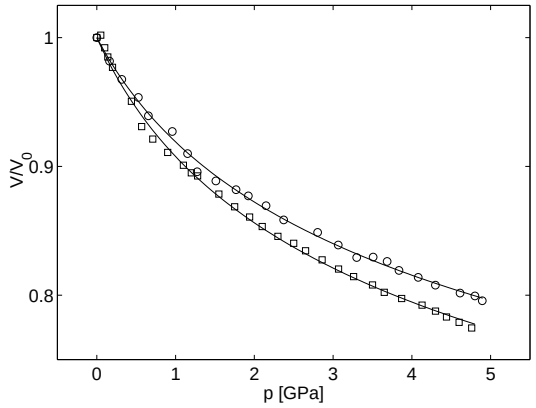

Fig. 4.19: Relative volume of DPO I (□) and DPO II (◯) under compression. The lines are the corresponding MEOS described in text.

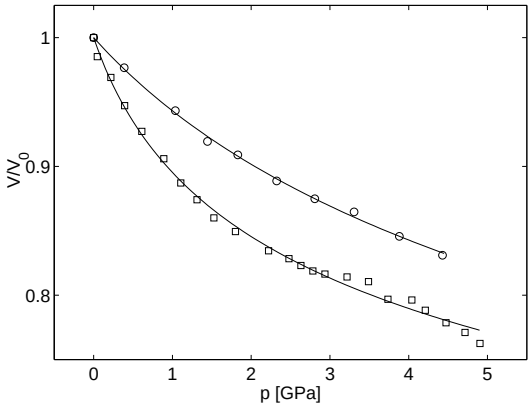

Fig. 4.20: Relative volume of 6DPO6 I (□) and 6DPO6 II (◯) under compression. The lines are the corresponding MEOS described in text.

DPO I :	K_0	=	7.3 GPa,	K_0'	=	6.7,	$p \in [0, 4.8]$ GPa
DPO II :	K_0	=	8.6 GPa,	K_0'	=	7.2,	$p \in [0, 4.9]$ GPa
6DPO6 I :	K_0	=	5.6 GPa,	K_0'	=	8.2,	$p \in [0, 4.9]$ GPa
6DPO6 II :	K_0	=	14.7 GPa,	K_0'	=	5.1,	$p \in [0, 4.4]$ GPa
7PO3 :	K_0	=	6.3 GPa,	K_0'	=	6.8,	$p \in [0, 4.1]$ GPa

All the oxadiazole crystals investigated have small values of K_0 and K_0', which indicates large compressibility with only slight dependence on pressure in the investigated range[§]. To facilitate the comparison of the results obtained for the different oxadiazole crystals, their MEOS are depicted together in fig. 4.22. The first remarkable feature is that the compression behaviour of the compound containing one phenylene ring (7PO3) does not differ strongly from that found for compounds with two phenylene rings. Taking into account their MEOS, the substances can be ordered in relation to increasing stiffness as follows: first, 6DPO6 I and 7PO3; then DPO I;

[§]Since $K = K_0 + K_0' p$ (eq. 4.5), a low value of K_0' indicates a weak dependence of K on pressure.

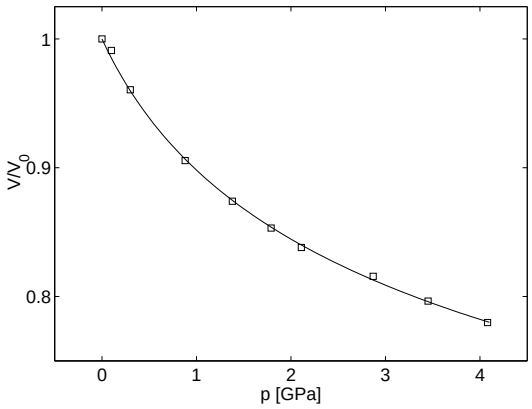

Fig. 4.21: Relative volume of 7PO3 under compression. The line is the corresponding MEOS described in text.

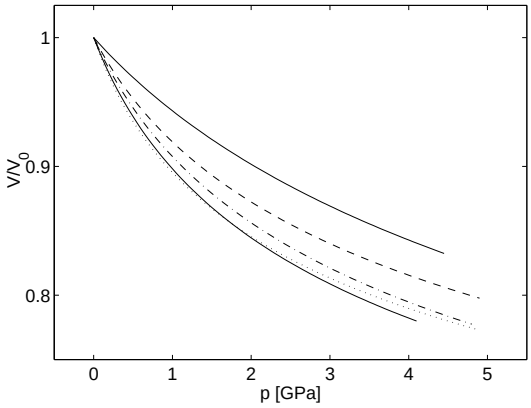

Fig. 4.22: From bottom to top: MEOS of 7PO3 (solid line bottom), 6DPO6 I (dotted line), DPO I (dash-dotted line), DPO II (dashed line) and 6DPO6 II (solid line top).

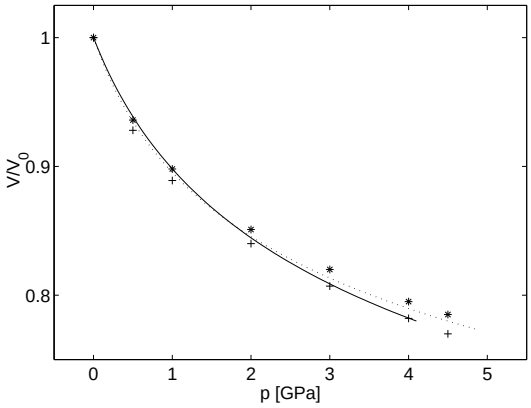

Fig. 4.23: MEOS of 7PO3 (solid line) and 6DPO6 I (dotted line), and experimental volumes for biphenyl (+) and para-terphenyl (*) from [125].

followed by DPO II; and finally, 6DPO6 II.

The softest substances are 6DPO6 I and 7PO3. The inter-molecular interactions in 6DPO6 I are weak H-bonds and van der Waals forces (cf. §3.4.3 and §3.4.4). In 7PO3 there are van der Waals interactions as well and pairs of molecules are connected by π-π interactions (cf. §3.4.6). The next soft substances are DPO I and, slightly less soft, DPO II. These crystals are held together by weak H-bonds and van der Waals forces and additionally by strong π-π interactions within the infinite π-complexes (see §3.4.1 and §3.4.2). The inter-molecular interactions in the stiffest material, 6DPO6 II, are weak H-bonds and van der Waals forces as in the other oxadiazole crystals and besides strong H-bonds between 6DPO6 molecules and water molecules (cf. §3.4.4). Combining the knowledge of the inter-molecular interactions present in the crystals with their relative stiffness, the following can be concluded.

(i) When the inter-molecular interactions in the crystal are weak H-bonds, van der Waals forces, and π-π interactions only between the *oxadiazole rings*, the substances are soft (6DPO6 I). This means that the potentials which describe the previous interactions are rather shallow.

(ii) In the case of having π-π interactions between *pairs* of molecules in addition to the weak H-bonds and the van der Waals forces does not increase the stiffness of the crystal (7PO3).

(iii) When, additional to weak H-bonding and van der Waals interactions, the molecules interact through π-π forces building *infinite stacks* of π-complexes, the stiffness of the material increases (DPO I and DPO II). This together with the low linear compressibilities of the stacks, discussed in §4.6.1, leads to the conclusion that the potential well which characterizes the π-π interactions of the infinite stacks has a large slope at short inter-molecular spacings.

(iv) The presence of strong H-bonds between 6DPO6 molecules and water molecules in 6DPO6 II, is responsible for the relatively high stiffness of this crystal. The H-bonds stabilise the crystal packing and restrict its compression. Therefore among those interactions which occur in oxadiazole crystals, H-bonding is believed to be described by the potential well with sharper edge at low inter-molecular distances.

We have also compared the decrease of the normalized volume of the oxadiazole crystals with that of similar aromatic compounds such as biphenyl and para-terphenyl from [125] (see fig. 4.23). Biphenyl and para-terphenyl show a compression behaviour very similar to that of 6DPO6 I and

7PO3. Additionally, we have expressed the experimental values for the volume decrease of biphenyl and para-terphenyl in terms of the MEOS (eq. (4.2)). The values for K_0 and K_0' are:

$$\begin{array}{lccccccc} \text{biphenyl}: & K_0 & = & 5.1\,\text{GPa}, & K_0' & = & 8.2, & p \in [0, 4.5]\,\text{GPa} \\ \text{para}-\text{terphenyl}: & K_0 & = & 5.8\,\text{GPa}, & K_0' & = & 8.4, & p \in [0, 4.5]\,\text{GPa} \end{array}$$

With the exception of 6DPO6 II, where strong H-bonds influence the compression behaviour, all the oxadiazole crystals investigated and the corresponding oligo(para-phenylene)s, biphenyl and para-terphenyl, show values for K_0 between 8.6 and 5.1 GPa and between 6.8 and 8.4 for K_0'. The relatively *weak* inter-molecular interactions of these molecular crystals, compared with ionic, covalent or metallic crystals, are responsible for these low values of the bulk modulus. Another organic compound—but not aromatic— for which the bulk modulus is known is tetra-cyano-ethylene (TCNE) in its two polymorphic forms. Yamawaki et al. determined the following values for K_0 and K_0' [126]:

$$\begin{array}{lccccccc} \text{TCNE}-\text{cubic}: & K_0 & = & 8.6\,\text{GPa}, & K_0' & = & 6.4, & p \in [0, 6.0]\,\text{GPa} \\ \text{TCNE}-\text{monoclinic}: & K_0 & = & 9.5\,\text{GPa}, & K_0' & = & 4.9, & p \in [0, 3.5]\,\text{GPa} \end{array}$$

The slightly larger values for the K_0 of TCNE, in relation to those of most oxadiazole crystals and to biphenyl and para-terphenyl, indicate that TCNE compresses in a slightly more difficult way than the previous aromatic compounds. However, it has to be noted that these differences are very small taking into account that differences between the K_0 values for these organic crystals and inorganic crystals are of at least one order of magnitude.

4.8 Summary

The structural study of oxadiazole crystals under compression can be summarized as follows.

(i) DPO I, DPO II, 6DPO6 I, 6DPO6 II, and 7PO3 do not show phase transitions at room temperature under compression in the pressure range up to about 5 GPa.

(ii) The only investigated crystal which undergoes pressure-induced phase transitions at room temperature is 6DPO4.

(iii) The three dimensional molecular arrangement of the present compounds induces a marked anisotropic response of the crystal under compression.

(iv) The least compressible axes are those where intense π-π interactions or strong H-bonds are present. Molecules connected in this way arrange, already at ambient pressure, very near to each other. For this reason the further approximation of the molecules is strongly hindered by electrostatic forces.

(v) Contrarily, axes along which the molecules are connected by weak H-bonds or van der Waals interactions, are easily compressible.

(vi) The volume-pressure isotherm of those oxadiazole crystals which do not undergo phase transitions, is well described by the MEOS.

(vi) The values of K_0 and K_0' obtained from the approximation of the experimental data by the MEOS are low. The small values of K_0 indicate the large compressibility of the substances. Besides, the relatively low K_0' implies that the softness of the crystals does not strongly depend on pressure.

(viii) The fact of having molecules with two or three rings only influences the compression in an indirect way. In the case of the oxadiazole compounds, 7PO3 is more compressible

than DPO I, DPO II and 6DPO6 II, but shows nearly identical compression behaviour as 6DPO6 I. The decisive factor are the inter-molecular interactions which hold together the molecules in the crystal. Since 7PO3 only possesses two aromatic rings, the formation of *infinite* π-complexes as those of DPO I and DPO II, is not possible. The lack of this kind of π-complexes, and hence of stacks, is the factor that determines the compression.

A direct comparison of the linear compressibilities of the lattice parameters of different crystals is not meaningful because of the different molecular arrangement. However, it should be pointed out that the values which we found for the oxadiazole crystals are in the same range as those determined by Puschnig et al. for biphenyl [115].

Chapter 5

Crystal structure under heating

5.1 Introduction

In the previous chapter we studied the effect of pressure on the crystal structure of the substances which are the subject of this work. Now we complete this study with the investigation of the effect of temperature.

In order to study the response of the crystals to temperature, we have used several experimental techniques. Firstly, we performed a thermo-gravimetric analysis (TGA) of the materials to determine possible weight changes under heating. This technique was combined with differential scanning calorimetric measurements (DSC). The DSC method informs about the presence of phase transitions of first order. Moreover, the latent heat of phase transitions can be derived from the DSC curves.

Once the most significant trends of the behaviour of the substances under heating were known from the DSC measurements, X-ray diffraction patterns of the crystals up to temperatures near the melting point were acquired. The objective of these experiments was the identification of the crystal structure of possible high temperature phases* and the determination of the expansion coefficient. As we did in the high pressure X-ray experiments, the sample was measured in the form of powder. However, here we used the angle dispersive technique, which considerably improves the quality of the diffraction patterns. The analysis of the X-ray data was performed with the program Powder Cell 2.3 [123], in the same manner as we did in the high pressure experiments. A discussion of the limitations of the analysis procedure can be found in §4.5.

5.2 TGA studies

The TGA studies of all self synthesized crystals, that is, all except 6DPO6 I, indicates that they are very pure and stable. They do not show considerable weight losses in the temperature range of interest, except 6DPO6 II as is explained below.

As is pointed out in §3.2, we investigated two samples of 6DPO6. The one provided by Aldrich contained mainly the water free modification 6DPO6 I. The self synthesized one was a mixture of 6DPO6 I and 6DPO6 II (21% and 79% at 303 K, respectively).

The TGA curves of the two samples of 6DPO6 up to 573 K are shown in fig. 5.1. Up to this temperature the first sample (6DPO6 I) looses only 3% of its mass, while the second one (mixture of 6DPO6 I and 6DPO6 II) loses 14%. The small mass loss of 6DPO6 I is due to sublimation.

*Although we do not achieve *high temperature* in the usual sense of several hundreds of degrees, we use the term *high temperature* phase to designate the phase which appears under heating.

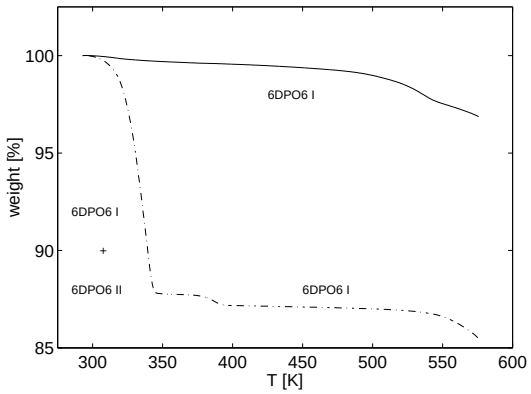

Fig. 5.1: TGA heating curves of 6DPO6 I (solid) and of the mixture of 6DPO6 I and 6DPO6 II (dash-dotted).

Contrarily, the mass loss of the mixture, which occurs principally around 338 K, is thought to be associated with the dehydration of the sample. However, sublimation cannot be fully ruled out. When this process ends, at approximately 344 K, the sample weighs 12% less than at 293 K. The remaining loss of mass up to 573 K is due to sublimation.

5.3 DSC studies

The DSC analysis of DPO II, 6DPO6 II, 6DPO4, and 7PO3 reveals that these crystals do not undergo any solid-solid phase transition under heating. The melting and crystallization temperatures found for the first and second cycles are reported in table 5.1. Since the 6DPO6 I sample, provided by Aldrich, contains some impurities (purity: 90%), the DSC curve shows a certain structure up to approximately 393 K in the first heating run. The introduction of a previous run in which the sample is heated up to 453 K and then cooled to 303 K, has nearly no influence on the shape and position of the melting and crystallization peaks of the posterior runs. The only consequence is the achievement of a smooth curve in the range where it was already heated. This is associated with the loss of impurities.

A more detailed description of the DSC results for those substances which undergo phase transitions under heating is given in the following.

5.3.1 DPO I

We performed several DSC measurements on DPO I. In the first series of experiments, DPO I was successively heated and cooled three times in the temperature interval 303 to 433 K. In the first heating curve a broad peak appears at 371 K (ΔH=3 kJ/mol) followed by the melting peak, at 414 K[†] (ΔH=24 kJ/mol). Figures 5.2 and 5.3 show the first and second heating/cooling curves. The successive cooling shows a unique peak associated with the crystallization at 389 K (ΔH=-17 kJ/mol). The next two heating and cooling cycles have the same parameters as the first one. The broadness of the peak at 371 K indicates that the process associated with it, a phase transition, occurs along a relatively large interval of temperature.

To determine whether this phase transition is reversible or irreversible, we performed a second

[†]In good agreement with the value reported in [51].

	cycle no.	T_m (K)	ΔH_m (kJ/mol)	T_c (K)	ΔH_c (kJ/mol)
	1	414	24	389	−18
DPO I*	2	414	24	389	−18
	1	415	24	388	−19
DPO II	2	414	24	387	−19
	1	525, 534	32	464, 465	−23
6DPO6 I	2	515, 519	28	460, 463	−23
	1	540	32	478	−22
6DPO6 II†	2	521, 525	23	468	−18
	1	453	28	436	−25
6DPO4	2	453	28	436	−25
	1	443	27	429	−27
7PO3	2	441	27	430	−27

Tab. 5.1: Melting and crystallization data from the DSC analysis of the investigated crystals. *The data are obtained from a sample which originally contained DPO I. †The DSC measurement was acquired from a sample originally composed of a mixture of 6DPO6 I and 6DPO6 II crystals (21% and 79% in mass, respectively, according to X-ray investigations).

series of measurements. It consisted firstly in the heating of DPO I up to 383 K, that is, some degrees after the phase transition but before the melting. Then, the substance was cooled to 303 K and twice successively heated and cooled along the whole temperature interval (303 to 433 K). As expected, in the first heating run the substance undergoes a phase transition at 371 K. During the first cooling no peaks appear. This means that there are no phase transitions of first order when cooling the high temperature phase, that is, DPO I undergoes an irreversible phase transition under heating. The melting and crystallization peaks of the following runs coincide well with those found in the first series of experiments.

We combined DSC with Raman spectroscopy to investigate the structure of the material obtained from the phase transition. With the DSC technique, we heated a sample of DPO I up to 383 K and then cooled it to room temperature. As expected, the DSC curves show the presence of the irreversible phase transition. The crystal obtained from the cooling was investigated by means of Raman spectroscopy. The comparison of its lattice modes with those of DPO II allowed to identify it as DPO II. Since the previous phase transition is irreversible, it can be concluded that the high temperature phase of DPO I is DPO II.

In a similar way, it is concluded that the crystal which results from the crystallization when cooling the melt is DPO II.

The small energy (3 kJ/mol) necessary to induce the transition of DPO I into DPO II is a typical feature of organic polymorphism. It indicates that the inter-molecular interactions in both crystals are similar as described in §3.4.1 and §3.4.2 and that the energy barrier between both structures is low.

5.3.2 6DPO6 II

We performed two DSC measurements of the 6DPO6 sample which at room temperature contains a mixture of 6DPO6 I and 6DPO6 II crystals (21% and 79% in mass, respectively, according to X-ray investigations, see §5.4.2). In the first measurement, the sample was successively heated and cooled twice in the interval 303 to 573 K. In the first heating curve, several peaks appear (fig. 5.4). We believe the first endothermic peak to be associated with loss of water from the sample (408 K). Its broadness and asymmetry is a consequence of the progressive escape of the water molecules: firstly, those which are near the crystal surfaces, and then the remaining ones. Then a small exothermic peak appears followed by a small endothermic one. They may be associated with

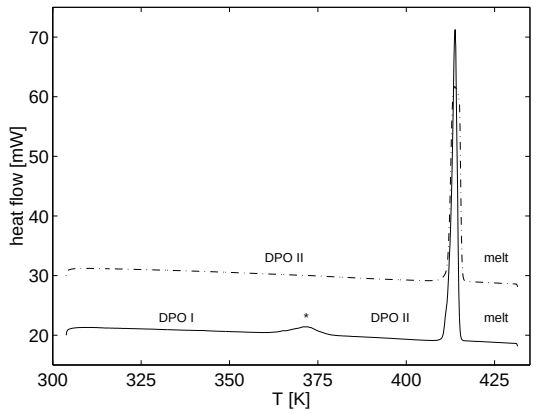

Fig. 5.2: DSC heating curves of DPO I: first (solid) and second (dash-dotted) heating runs. The dash-dotted curve is 10 mW vertically shifted for the purpose of clarity.

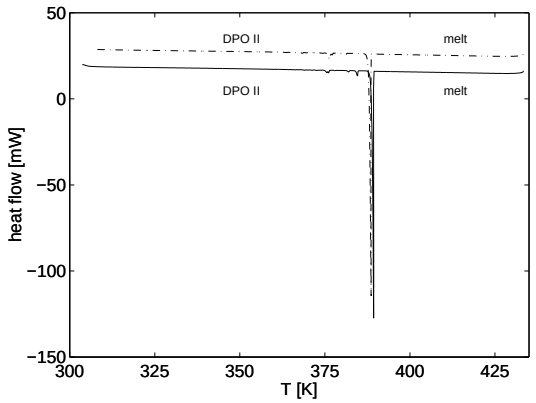

Fig. 5.3: DSC cooling curves of the mixture of 6DPO6 I and 6DPO6 II: first (solid) and second (dash-dotted) heating runs. The dash-dotted curve is 10 mW vertically shifted for the purpose of clarity.

the rearrangement of the 6DPO6 molecules and possible restructuring of the crystal. By further heating, the sample undergoes a new phase transition (428 K, ΔH=47 kJ/mol[‡]). The resulting phase is maintained up to the melting of the sample (540 K, ΔH=32 kJ/mol). The posterior cooling curve shows a unique crystallization peak (478 K, ΔH=22 kJ/mol, fig. 5.5). The second heating and cooling show a double melting peak (521 and 525 K, ΔH=23 kJ/mol) and a crystallization peak (468 K, ΔH=18 kJ/mol), respectively. The fact that the first and second melting, as well as the first and second crystallization peak strongly differ induces the hypothesis of the formation of a new phase from the melt.

In order to conclude w.r.t. reversibility of the phase transition, we carried out a second DSC experiment in the same manner as for DPO I (§5.3.1). The first heating run was stopped at 453 K, that is, after the dehydration process but before the melting. Then, the substance was cooled to 303 K and again heated and cooled along the whole temperature range (303 to 573 K), twice. As in the first experiment, the first heating of the sample induces the dehydration and molecular rearrangement. It occurs again in several steps with very similar parameters as before. The following cooling shows no peaks. Therefore, the dehydration process is irreversible. The melting and crystallization peaks of the next runs match up with those of the first experiment.

Again, to determine the structure of the substance which results from the dehydration, we combined DSC with Raman spectroscopy. The sample was heated up to 453 K and then cooled to room temperature. The irreversible dehydration was confirmed by the DSC curve. The Raman spectrum of the substance, indicates that it is in fact 6DPO6 I. Thus, it can be affirmed that 6DPO6 II transforms irreversibly into 6DPO6 I under heating.

Analogously, we measured the crystal obtained from the crystallization by the second cooling cycle of the liquid. Its Raman spectrum does not coincide neither with that of 6DPO6 I nor with that of 6DPO6 II confirming the idea exposed above that the crystal obtained from the solidification of the melt shows a new structure. This structure is still unknown.

[‡]To calculate the number of moles of 6DPO6, we assumed that the sample was completely dehydrated, following the results of the X-ray experiments.

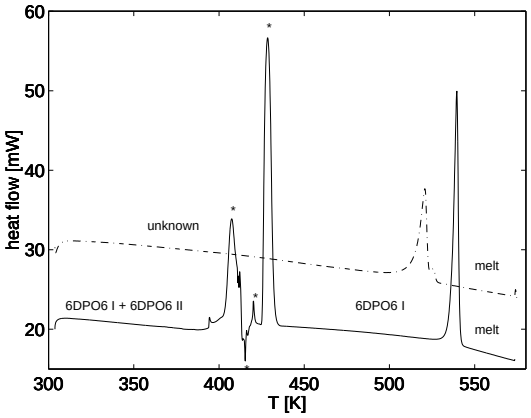

Fig. 5.4: DSC heating curves of the mixture of 6DPO6 I and 6DPO6 II: first (solid) and second (dash-dotted) heating runs. The dash-dotted curve is 10 mW vertically shifted for the purpose of clarity.

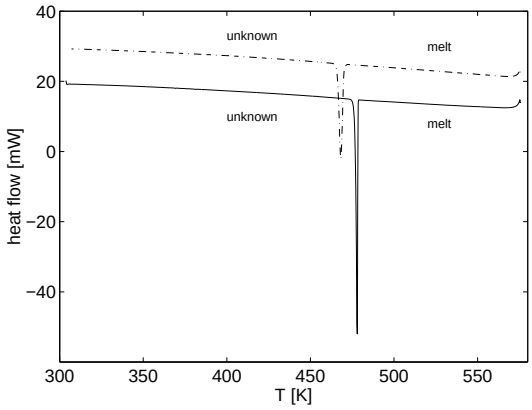

Fig. 5.5: DSC cooling curves of the mixture of 6DPO6 I and 6DPO6 II: first (solid) and second (dash-dotted) heating runs. The dash-dotted curve is 10 mW vertically shifted for the purpose of clarity.

5.4 X-ray diffraction under heating

The X-ray patterns of DPO II, 6DPO6 I, 6DPO4, and 7PO3 do not show modifications besides the shift to lower 2θ-values, that is, to larger d-spacings associated with the expansion of the crystal. This means that no structural changes appear under heating in agreement with the DSC results. Under vacuum and quasi-static conditions the previous crystals strongly sublimate above approximately 40 K below their melting temperatures. 6DPO4 presents an exception to this behaviour. The onset of its sublimation appears just a few degrees before its melting point. The strong sublimation of the crystals is a consequence of the weakness of the forces which hold the molecules together.

As pointed out in the previous chapter (§4.3), the thermodynamic state of a system with a constant number of particles, is completely characterized by the relation among volume V, pressure p, and temperature T. We also mentioned that when dealing with solids, an isothermal equation of state of the type $V(p, T_0) = V(p)$—as those determined for the oxadiazole crystals (§4.7)—may describe quite well the behaviour of the system. The effect of temperature can then be taken into account as a correction to the equation through a coefficient of thermal expansion $\alpha(p)$ which is in general a function of pressure, viz.

$$V(p, T) = V(p, T_0)\,[1 + \alpha(p)\,(T - T_0)] \tag{5.1}$$

A proper estimation of the thermal expansion coefficient of the crystals which undergo phase transitions under heating (DPO I and 6DPO6 II) as well as of DPO II was not possible with the available technique. The expansion of these crystals before the solid-solid phase transition and before the sublimation, respectively, was not large enough. However, such an estimation could be performed, at least in an approximate way, for the other substances. The modifications of the volume of these crystals up to the onset of the sublimation are shown in fig. 5.6, 5.8, and 5.10[§]. In order to determine the coefficient of thermal expansion, we consider—as a first approximation—a *linear* dependence of the volume upon temperature:

$$V(p_0, T) = V(p_0, T_0)\,[1 + \alpha_0\,(T - T_0)] \tag{5.2}$$

[§]The experimental lattice parameters under heating of all the studied compounds are reported in tables E.1 to E.3.

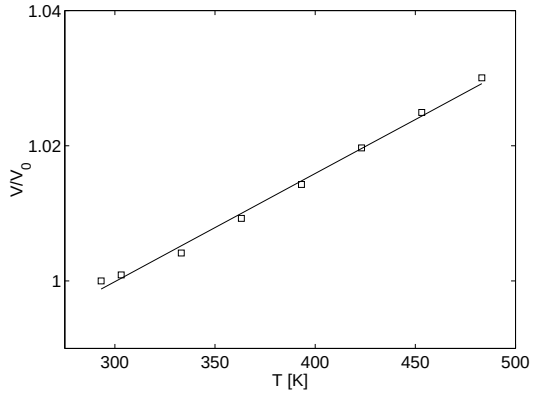

Fig. 5.6: Relative volume of 6DPO6 I under heating. The line corresponds to the adjustment for the determination of α_0.

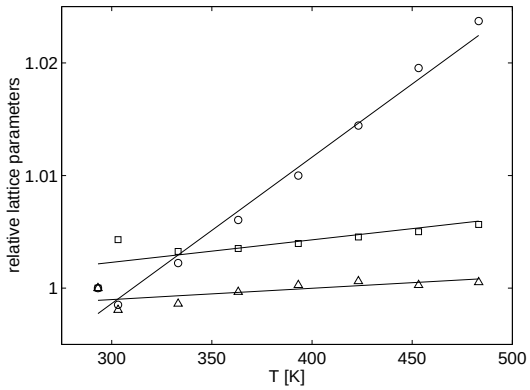

Fig. 5.7: Relative lattice parameters of 6DPO6 I under heating ($\square\, a/a_0$, $\bigcirc\, b/b_0$, $\triangle\, c/c_0$). The lines correspond to the fits described in the text.

thus,

$$\alpha = \frac{1}{V}\left(\frac{\partial V}{\partial T}\right)_p \approx \frac{1}{V(p_0,T_0)}\left(\frac{\partial V}{\partial T}\right)_{p_0} = \alpha_0 \tag{5.3}$$

The values of α_0 determined by applying (5.3) to our data are:

$$\begin{array}{lllll} \text{6DPO6 I}: & \alpha_0 & = & 1.6\cdot 10^{-4}\,\mathrm{K}^{-1} & T\in[293,483]\,\mathrm{K} \\ \text{6DPO4}: & \alpha_0 & = & 2.6\cdot 10^{-4}\,\mathrm{K}^{-1} & T\in[293,443]\,\mathrm{K} \\ \text{7PO3}: & \alpha_0 & = & 1.9\cdot 10^{-4}\,\mathrm{K}^{-1} & T\in[293,383]\,\mathrm{K} \end{array}$$

These values are of the same order as those found for similar organic compounds [125].

The coefficients of linear expansion of the lattice parameters were determined in an analogous way. Figures 5.7, 5.9, and 5.11 show the behaviour of the lattice parameters of 6DPO6 I, 6DPO4, and 7PO3 under heating. The following linear coefficients in the temperature were determined:

$$\begin{array}{lllll} \text{6DPO6 I}: & \alpha_{0la} & = & 2\cdot 10^{-5}\,\mathrm{K}^{-1} & T\in[293,483]\,\mathrm{K} \\ & \alpha_{0lb} & = & 13\cdot 10^{-5}\,\mathrm{K}^{-1} & T\in[293,483]\,\mathrm{K} \\ & \alpha_{0lc} & = & 1\cdot 10^{-5}\,\mathrm{K}^{-1} & T\in[293,483]\,\mathrm{K} \\ \text{6DPO4}: & \alpha_{0la} & = & 20\cdot 10^{-5}\,\mathrm{K}^{-1} & T\in[293,443]\,\mathrm{K} \\ & \alpha_{0lb} & = & -8\cdot 10^{-5}\,\mathrm{K}^{-1} & T\in[293,443]\,\mathrm{K} \\ & \alpha_{0lc} & = & 20\cdot 10^{-5}\,\mathrm{K}^{-1} & T\in[293,443]\,\mathrm{K} \\ & \alpha_{0\beta} & = & 4\cdot 10^{-5}\,\mathrm{K}^{-1} & T\in[293,443]\,\mathrm{K} \\ \text{7PO3}: & \alpha_{0la} & = & 4\cdot 10^{-5}\,\mathrm{K}^{-1} & T\in[293,383]\,\mathrm{K} \\ & \alpha_{0lb} & = & 2\cdot 10^{-5}\,\mathrm{K}^{-1} & T\in[293,383]\,\mathrm{K} \\ & \alpha_{0lc} & = & 13\cdot 10^{-5}\,\mathrm{K}^{-1} & T\in[293,383]\,\mathrm{K} \\ & \alpha_{0\beta} & = & 2\cdot 10^{-5}\,\mathrm{K}^{-1} & T\in[293,383]\,\mathrm{K} \end{array}$$

It is interesting to note that the most compressible axes (a and c in 6DPO6 I, and c in 7PO3; see §4.6.3 and §4.6.5 are the most expansible ones. This is consequence of the relatively strong inter-molecular interactions along these axis (cf. §3.4.3 and §3.4.6).

Again, we describe below in more detail the results obtained from the X-ray diffraction study of those substances which show phase transitions under heating.

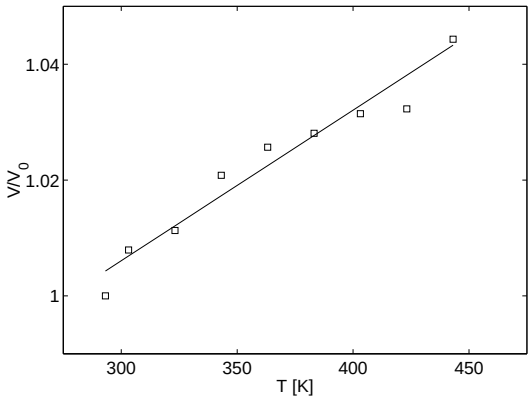

Fig. 5.8: Relative volume of 6DPO4 under heating. The line corresponds to the adjustment for the determination of α_0.

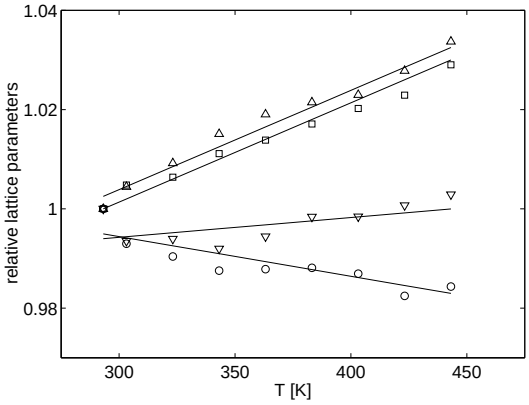

Fig. 5.9: Relative lattice parameters of 6DPO4 under heating ($\square$ a/a_0, $\bigcirc$ b/b_0, $\triangle$ c/c_0, $\bigtriangledown$ β/β_0). The lines correspond to the fits described in the text.

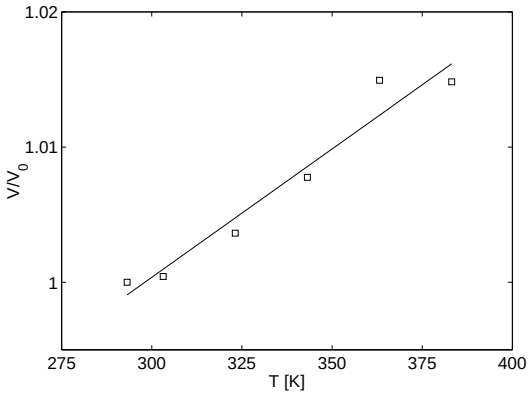

Fig. 5.10: Relative volume of 7PO3 under heating. The line corresponds to the adjustment for the determination of α_0.

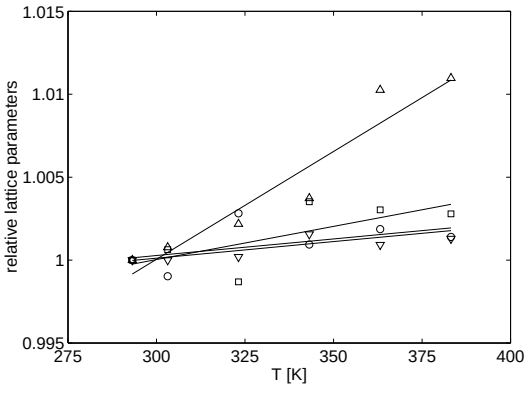

Fig. 5.11: Relative lattice parameters of 7PO3 under heating ($\square a/a_0$, $\bigcirc b/b_0$, $\triangle c/c_0$, $\bigtriangledown \beta/\beta_0$). The lines correspond to the fits described in the text.

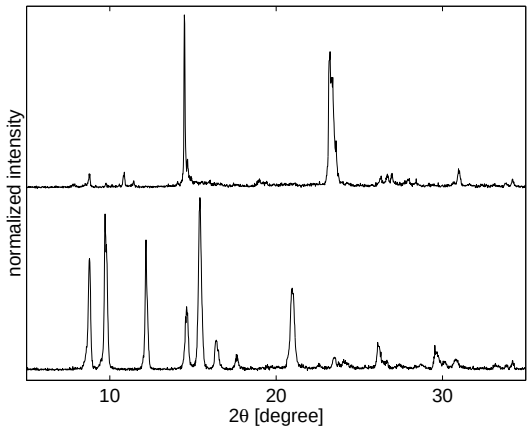

Fig. 5.12: X-ray diffraction pattern of DPO I at 333 K before the phase transition (bottom) and at 348 K after it (top).

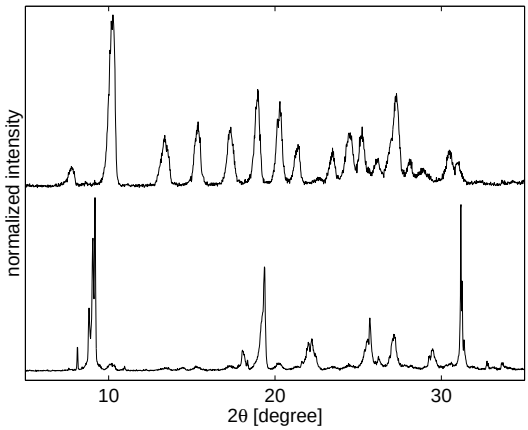

Fig. 5.13: X-ray diffraction pattern of the mixture of 6DPO6 I and 6DPO6 II at 303 K before the phase transition (bottom) and at 333 K after it (top).

5.4.1 DPO I

The phase transition process can be directly visualized by means of X-ray diffraction. Figure 5.12 shows the X-ray patterns of DPO I before and after the transition. The latter pattern coincides with that of DPO II. Up to 333 K only the first structure is present but at 338 K already 32% (by mass) of the sample has transformed into the second structure. With increasing temperature this percentage increases rapidly. At 343 K, 72% of the sample showed the second structure and at 348 K this percentage was 98%—which can be considered, within the impurity limit detectable with X-ray techniques, as a full transformation. From the X-ray experiments, it results that the phase transition occurs at a temperature between 338 and 348 K. The disagreement between this temperature and that determined by DSC (371 K) is due to several facts. On the one hand, the pressure conditions are different: while the DSC curve is taken at ambient up to slightly enhanced pressure (the sample chamber is closed), the X-ray experiments were performed under vacuum. On the other hand, the temperature measurement and control in the heating device coupled with the X-ray diffractometer are not so accurate as those of the DSC experiment. The experimental error in the temperature determination is estimated to 4 K. However, the most important reason for the disagreement in the transition temperature is the fact that the X-ray measurement is performed in a quasi-static regime (every temperature step was maintained several hours) while the DSC technique is a dynamic method.

A detailed inspection of the crystal structures leads to the conclusion that the transition from DPO I to DPO II occurs through an intermediate amorphous state (see §3.4.1 and §3.4.2, for a description of the crystal packings). Since every third molecule of the stacks of DPO II is oriented in the opposite direction, a mechanism in which the molecular arrangement within the stacks is maintained is not possible. The destruction of the infinite π-complexes is necessary. Since the π-π inter-molecular interactions within the stacks are the strongest forces which build the crystals, the crystal looses its perfect order when the π-complexes are broken and becomes amorphous. Of course, a certain short range order may be maintained. Then, since the π-π interactions are strong, the molecules rearrange, building again infinite stacks leading to DPO II. Since the DSC curve shows a unique peak, the possibility of the presence of further intermediate crystalline states is discarded. However, to confirm this hypothesis, single X-ray technique combined with an extremely precise heating device is needed.

5.4.2 6DPO6 II

The dehydration of 6DPO6 II under heating could be confirmed by the X-ray experiments. The original sample was a mixture of 6DPO6 I and 6DPO6 II. At 303 K the percentage of 6DPO6 I was 21%. This percentage amounts to 60% already at 318 K. At 323 K 91% of the sample was 6DPO6 I. The dehydration is completed at 333 K, where the whole sample has the structure 6DPO6 I (fig. 5.13). Thus, the dehydration temperature under vacuum determined from the X-ray investigations is around 318 K. Here, the remarks concerning the differences in the phase transition temperature determined by DSC and by X-ray under heating outlined in the preceding subsection have to be considered.

Since the mass fractions are known, the weight loss can be easily calculated. For a sample with the initial (at 303 K) content: 21% 6DPO6 I and 79% 6DPO6 II, the weight loss at 333 K amounts to 10%. This value coincides roughly with that determined by TGA, which is 12%.

With the available technique, the presence of intermediate crystalline states in the phase transition from 6DPO6 II to 6DPO6 I, proposed from the analysis of the DSC curves, cannot be investigated. Single crystal diffractometry with a highly precise heating device should be used.

5.5 Summary

From our investigation of oxadiazole crystals under heating the following points can be concluded.

(i) The TGA shows the large thermal stability of these compounds.

(ii) The latent heat of the solid-liquid phase transitions lies between 20 and 30 kJ/mol. This rather low value indicates the weakness of the inter-molecular forces responsible for the building of the crystals.

(iii) DPO I undergoes an irreversible phase transition into DPO II. The phase transition temperature is 371 K at ambient pressure, in a dynamic process (DSC); and between 338 and 348 K under vacuum, in a quasi-static process (X-ray).

(iv) 6DPO6 II irreversibly dehydrates into 6DPO6 I. The dehydration temperature is 338 K at ambient pressure in N atmosphere (TGA); between 408 and 428 K at ambient pressure, in a dynamic process (DSC); and around 318 K under vacuum and in a quasi-static process (X-ray).

(v) All the other investigated crystals do not suffer any phase transitions under heating except the final melting.

(vi) The coefficient of thermal expansion of 6DPO6 I, 6DPO4 and 7PO3 is around $\alpha_0 = 2 \cdot 10^{-4}\ \mathrm{K}^{-1}$, as for similar substances.

(vii) The coefficients of linear expansion of the lattice parameter of 6DPO6 I, 6DPO4 and 7PO3 could be determined as well. It turns out that the more compressible axes are those which show larger expansion under heating, as expected.

Chapter 6

Electronic transitions at normal conditions

6.1 Introduction

The optical properties of the substances in solid state are of great interest to our study. They allow for a distinction between influences caused by changes of the *intra-molecular* interactions (*molecular* level) from those with origin in the variation of the *inter-molecular* interactions (*super-molecular* level). However it should be taken into account that these two levels are related. The molecular conformation of a given molecule, and therefore its electron distribution, may depend on the super-molecular arrangement. For instance, thin films as well as amorphous and crystalline solid states may be built by distinct conformers of the same molecule. Additionally, the presence of relatively strong interactions among the molecules can lead to the modification of the electronic structure.

In this chapter we study the influence of the intra- and inter-molecular interactions on the absorption and emission properties of our set of oxadiazole compounds. On the one side, the absorption and fluorescence spectra of the compounds in solution were compared in order to study the influence of the substituents (a more complete comparison with similar compounds is reported in §B.2). On the other side, the crystals were investigated under normal conditions. The comparison of the optical properties of a given compound in solution and in crystalline state and among different crystal structures provides valuable information about the influence of the inter-molecular interactions on the electronic structure. These results are then completed by the investigation under compression as described in the following chapter.

6.2 Literature review

Due to their interesting applications as LED material, several oxadiazole compounds were already investigated from the point of view of their electronic transitions in solution and in thin films, both in low molecular form [25, 26, 127, 128, 129, 130] and as polymers [1, 9, 15, 17, 18, 25, 131, 132]. Special attention was given to 2-(diphenyl-4'-yl)-5-phenyl-1,3,4-oxadiazole (PBO) and 2-(4-diphenyl)-5-(4-t-butyl-phenyl)-1,3,4-oxadiazole (PBD) derivatives [13, 14, 133, 134, 135]. Nevertheless, up to now the only articles dealing with the electronic transitions of oxadiazole compounds in crystal state are those which appeared in the frame of the present work [62, 136].

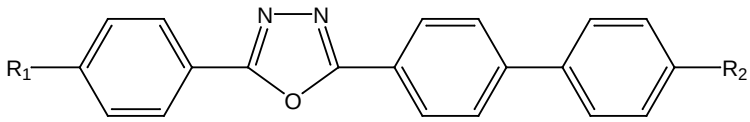

Fig. 6.1: PBO derivatives.

6.2.1 Substituent variation of DPO and PBO derivatives in solution

Popova et al. investigated the dependence of the absorption and fluorescence of some DPO derivatives on the electronic structure of the substituents (in para-position) [129]. The absorption spectra of these materials in toluene solution show three bands. The authors focus on the most intense one, which is in the long wavelength region. For DPO the maximum is at 284 nm and for its derivatives between 300 and 390 nm (cf. table F.1). It is associated with a $\pi\pi^*$ transition within the delocalized π electron system of the entire molecule in agreement with the theoretical results of Pedash et al. [137]. This band is responsible for the fluorescence. The fluorescence maximum of DPO in toluene occurs at 365 nm, and for the other substances between 360 and 565 nm (cf. table F.1). The authors observed that the introduction of substituents implies a red shift of the long wavelength absorption band as well as of the emission band. Together with the shift, an increase of the molar extinction coefficient and a retention of the high fluorescence quantum yield are observed. From the study of dipole moments of these molecules the authors concluded that the oxadiazole ring is an electron acceptor.

It should be remarked that some molecules containing the DPO basic unit do not behave like oxadiazole compounds. Sometimes another group has more importance for its electronic transitions. This is the case of the substances investigated by Krasovitskii et al. and by Gruzinskii et al. which in addition to the DPO basic unit contain a C=C bond and behave hence as stilbene compounds [138, 139]. Only the short-wave absorption band of the molecules investigated by Krasovitskii et al. could be linked to the present compounds.

Lunak et al. studied the photo-physics of several PBO derivatives (fig. 6.1) in 2-methyl-tetrahydro-furan (MTHF) [134]. Some of these compounds were also theoretically investigated using the Pariser-Parr-Pople method. In a similar way as Popova et al. did for the DPO derivatives, Lunak et al. encountered that the addition of substituents implies a red shift in the absorption (maxima between 305 and 340 nm) and fluorescence (maxima between 365 and 450 nm) bands (cf. table F.2).

6.2.2 Molecular structure modification of DPO derivatives in solution

The dependence of the absorption and fluorescence of some DPO derivatives in hexane on their molecular conformation was experimentally studied by Feygelman et al. [140]. Introducing CH_3 groups at the ortho-positions of the phenyl rings, a non planar geometry of the molecule in the ground state is obtained. The absorption spectrum has two bands: one around 200 nm and another one which moves between 240 and 300 nm, depending on the molecule. The authors identify the band around 200 nm with the absorption of the non conjugated 1,3,4-oxadiazole ring because this band does not depend on the molecular geometry. Contrarily, the long-wave band shifts to lower wavelengths (higher energies) when the molecule adopts a non planar conformation. Taking into account the red shift that appears with the addition of an electron donor substituent, Feygelman et al. concluded the $\pi\pi^*$ nature of this electronic transition, in agreement with Popova et al. [129].

Since pure hexane absorbs at 200 nm, we believe that the short-wave band reported by Feygelman et al. is due to the solvent. The authors also indicate the presence of a small shoulder around 240 nm in the absorption spectra of the DPO derivatives. By comparison with our own results, we propose that this small band is associated with an $n\pi^*$ transition localized at the hetero-atoms

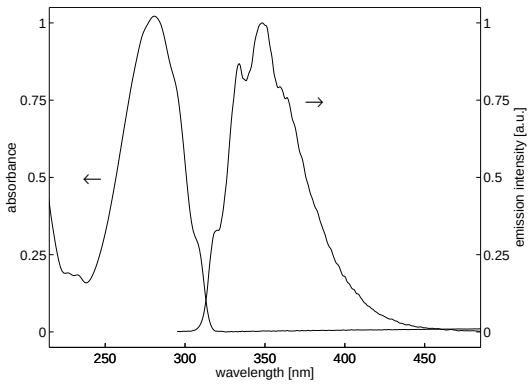

Fig. 6.2: Absorption (left) and emission (right) spectra of DPO in ethanol.

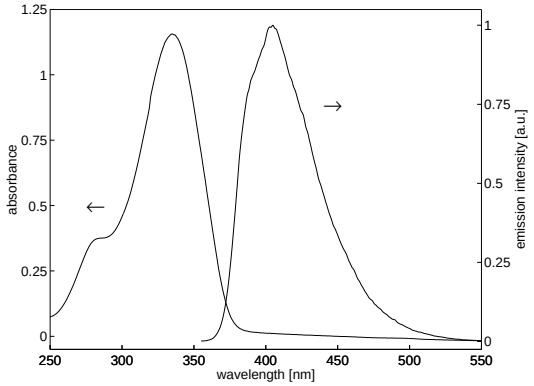

Fig. 6.3: Absorption (left) and emission (right) spectra of 6DPO6 in ethanol.

(N and O) of the oxadiazole group (for a discussion about the association of the bands in our compounds see §B.2).

The emission of these compounds does not depend on the addition of CH_3 groups in ortho-position. They all show a band with some vibrational structure at about 370 nm. To explain this the authors propose that the conformation of the molecules in the excited state is planar. Thus, the molecules, which are non planar in the ground state, undergo a torsional relaxation process in the excited state.

6.3 Absorption and emission spectra of solutions

To begin the study of the optical properties, we investigated the absorption and emission spectra of dilute solutions of our set of substances*. The inter-molecular interactions solute-solute are expected to be negligible. The solvent was chosen to be ethanol. Although a non polar solvent is preferred in order to reduce the interactions solute-solvent, most of the oxadiazole compounds are not soluble in such solvents.

The absorption spectrum of DPO, 6DPO6, 6DPO4 and 7PO3 in ethanol is characterized by two bands (see fig. 6.2 to 6.5). The maximum of the short wave band is between 230 (the very small band of DPO) and 303 nm, depending on the substance. That of the long wave band, the most intense one, is between 280 and 345 nm. The exact values are summarized in table 6.1. The position of both bands matches well with those reported by Popova et al. and by Feygelman et al. (see §6.2.1 and §6.2.2). We agree with the conclusion of these authors that the long-wave band results from a $\pi\pi^*$ transition delocalized along the molecule and propose that the small short-wave band is associated with an $n\pi^*$ transition localized at the hetero-atoms of the oxadiazole ring and the possible substituents. Further discussion can be found in §B.2.

The excitation at the maximum of the long-wave absorption band induces an intense emission with vibrational structure and maximum between 349 and 425 nm, depending on the compound (see fig. 6.2 to 6.5 and table 6.1). Time resolved measurements performed on DPO and some of its derivatives in ethanol and other solvents, indicated that the decay times of these transitions are in the range of few nanoseconds (1-3 ns) [11, 128, 141]. Thus, the emission may correspond to a fluorescence, that is, to a singlet-singlet transition.

DPO, 6DPO6 and 6DPO4 show an abnormally large Stokes shift in ethanol solution (see

*Since we do not perform any studies on the absolute absorbance and emission intensity, the solutions were prepared to achieve absorbances around 1. This corresponds to concentrations in the order of 10^{-5} mol/l.

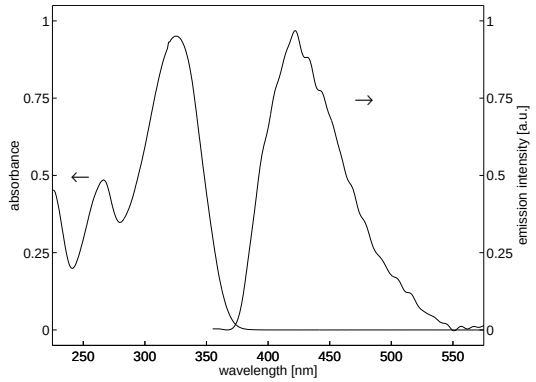

Fig. 6.4: Absorption (left) and emission (right) spectra of 6DPO4 in ethanol.

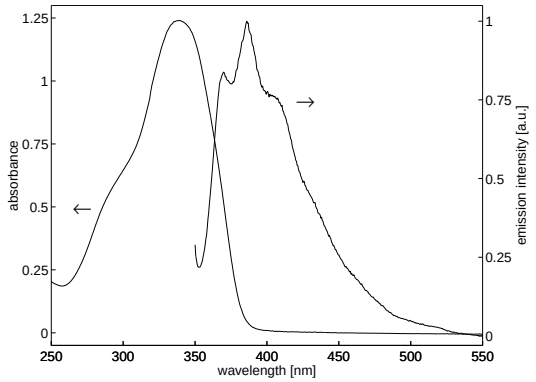

Fig. 6.5: Absorption (left) and emission (right) spectra of 7PO3 in ethanol.

	$\lambda^{abs}_{n\pi^*}$ (nm)	$\lambda^{abs}_{\pi\pi^*}$ (nm)	$\lambda^{lum}_{\pi\pi^*}$ (nm)	Stokes shift (nm)
DPO	230	280	349	69
6DPO6	285	336	405	68
6DPO4	264	324	425	101
7PO3	303	345	385	40

Tab. 6.1: Absorption and emission maxima of the investigated compounds in ethanol solution.

table 6.1), which implies its optical transparency to self absorption, making them interesting materials for technological applications. The normal Stokes shift results from the loss of excitation energy by thermalization of the excess vibrational energy (cf. fig. 6.6(a)). This process, called internal conversion, occurs normally in 10^{-12}s or less, and is thus prior to emission (the lifetime of S_1 in DPO was estimated to 1-3·10^{-9}s [11, 128, 141]). In addition, DPO, 6DPO6, and 6DPO4 display further contributions to the Stokes shift due to solvent effects and to the modification of the molecular conformation in S_1 (cf. fig. 6.6(b)). The relatively long lifetime of S_1 allows ample time for the solvent molecules to reorient around the excited molecule by rapid rotational motions, which lowers the energy of S_1. This process, called solvent relaxation, only occurs for polar fluorophores (e.g. the investigated compounds) and takes approximately 10^{-10}s. Another mechanism which induces the abnormally large Stokes shift is the geometric reorganization of the atoms in the excited molecule. By comparison with similar oxadiazole compounds [140] (cf. §6.2.2), para-terphenyl [11], and phenyl-oxazolyl and phenyl-oxadiazolyl compounds [142, 143], we propose that these molecules undergo a structural relaxation in S_1 from the non planar Franck-Condon state to a planar relaxed state. Such a flattening leads to the partial recovery of the conjugation and therefore to a decrease in the S_1 energy. The presence of better resolved vibrational structure in the emission than in the absorption bands supports the previous conclusion of the planarization of the molecules in S_1 [11].

Since the Stokes shift of the 7PO3 solution is relatively small (cf. table 6.1), 7PO3 may not undergo a strong relaxation in S_1. We believe that the molecule is planar or nearly planar already in S_0 and therefore does not perform an important flattening process in S_1 as the other compounds do. The strong electron donor character of the $N(CH_3)_2$ group and the fact that 7PO3 possesses only one phenyl ring, may induce the planarity of the molecule in S_0.

The comparison of the absorption spectra[†] of the solutions of 6DPO4 and 6DPO6 with that of

[†]Since the investigated compounds show an abnormally large Stokes shift in ethanol solution, the position of the absorption maximum and not the emission maximum is a preferable reference when comparing different substances.

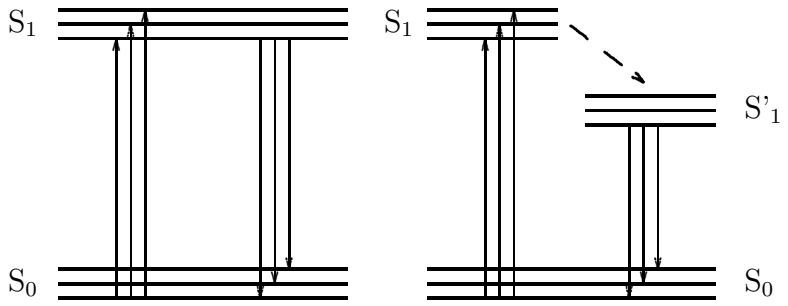

(a) Normal Stokes shift. (b) Abnormally large Stokes shift.

Fig. 6.6: Energy scheme illustrating (a) the normal and (b) the abnormally large Stokes shift. The normal Stokes shift results from the loss of the excess vibrational energy. The abnormally large Stokes shift results from the loss of the excess vibrational energy and the further relaxation of the molecule in the excited state (from S_1 to S'_1) caused by the solvent effect and the flattening of the molecule. Though it is not indicated in (b), the solvent may affect S_0 too, increasing its energy [144]. The transitions between the different vibrational states are not indicated in the figure for the purpose of clarity.

DPO confirms the following expected phenomenon: the introduction of a donor substituent, like NH_2 in 6DPO4 and in 6DPO6, induces a red shift of the absorption in relation to the unsubstituted DPO. The magnitude of the red shift increases with an increase of the donor properties of the second substituent: 6DPO6 is more shifted than 6DPO4 since NH_2 has a larger donor character than OCH_3. This effect is due to the increase of the conjugation of the molecules. In §B.2 we present a study of the effect of the substituents on the absorption and fluorescence spectra of several DPO derivatives in solution.

6.4 Absorption and emission spectra of crystals

In order to achieve a good absorption spectrum from the crystals, a thin and homogeneous sample is needed. The preparation of DPO I, DPO II, and 6DPO6 I[‡] in this form following the usual procedure was not possible (cf. §2.3.2 for a description of the usual preparation procedure). In the case of the DPO polymorphs this problem could be overcome using an alternative preparation method. We dissolved some DPO I crystals in ethanol directly on the quartz plate and investigated the film resulting after the evaporation of the solvent. Observation of the sample under a microscope showed that it was formed by a mixture of needle-like crystals with few plate-like crystals. To determine the crystal structure of the needles and plates, a Raman spectrum was acquired. The lattice modes of the sample correspond principally with those of DPO I but there was also a low percentage of DPO II. We used the previous procedure with 6DPO6 I but the obtained film was amorphous (it did not show any external Raman modes). Since we are interested in materials with perfectly determined structure, e.g. crystals, this sample was not further investigated. However, the mixture of 6DPO6 I and 6DPO6 II crystals (21% and 79% in mass, respectively, according to X-ray investigations, §5.4.2) could be satisfactorily prepared in the usual way.

Figures 6.7 to 6.10 compare the absorption spectra of the investigated compounds in ethanol solution and in crystal state. The quality of the spectra of the crystals is not as high as that of the solutions due to perturbations caused by the large thickness of the crystals, and by phenomena

[‡]We tried unsuccessfully to prepare an appropriate film with both the 6DPO6 I sample provided by Aldrich and a sample obtained by sublimation (during the X-ray experiments under heating), which had higher purity. The emission measurements were performed from the crystal achieved from the sublimation.

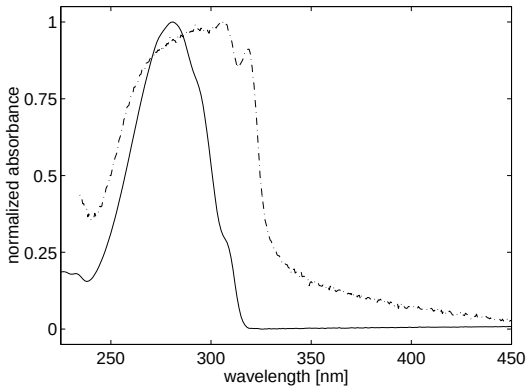

Fig. 6.7: Absorption spectra of DPO in ethanol (solid curve) and of a mixture of DPO I and DPO II crystals (dash-dotted curve).

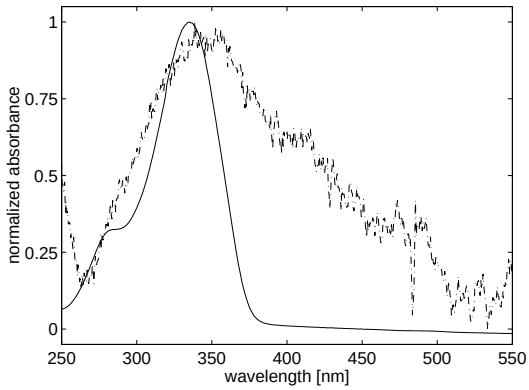

Fig. 6.8: Absorption spectra of 6DPO6 in ethanol (solid curve) and of a mixture of 6DPO6 I and 6DPO6 II crystals (21% and 79% in mass, respectively, according to X-ray investigations) (dash-dotted curve).

such as scattering at small crystals and reflection at crystal surfaces. Despite the short-wave band is not resolved in most of the crystal spectra, it can be recognized that they show essentially the same pattern as the spectra of the solutions. In the crystal state no new bands appear. That is, the optical properties of the *crystal* are principally ruled by those of the *molecule*. However, the spectrum of the crystals are strongly red shifted in relation to that of the solution (except in the case of 7PO3 which is blue shifted, fig. 6.9) and broader. We believe that the increased width of the $\pi\pi^*$ band, probably together with a red shift of the short-wave band, induces the loss of resolution of the latter. The positions of the maxima of the crystal spectra together with their shift in relation to the solution spectra are given in table 6.2.

The acquisition of emission spectra from normally prepared samples of all crystals presented no difficulties (see fig. 6.11 to 6.14). As it occurs for the absorption, the fluorescence of the crystals corresponds well with that of the solution and is slightly red shifted in relation to it (cf. table 6.2 for the exact maximum values and their shift compared to the solution spectra). The red shift of

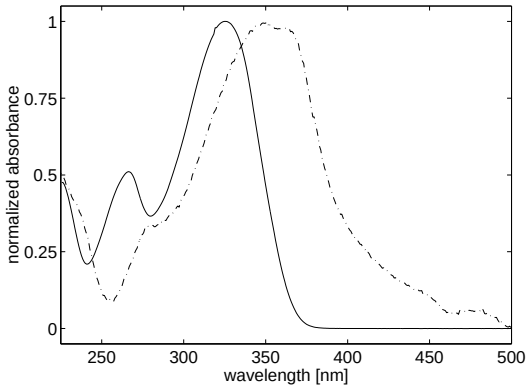

Fig. 6.9: Absorption spectra of 6DPO4 in ethanol (solid curve) and in crystal state (dash-dotted curve).

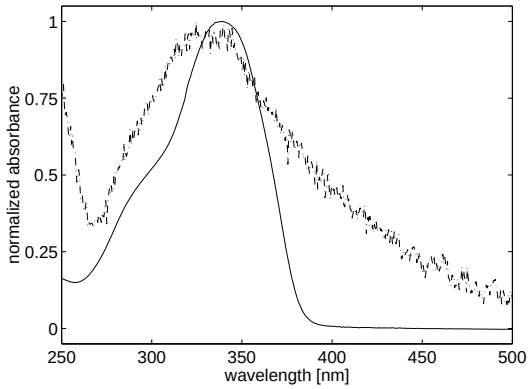

Fig. 6.10: Absorption spectra of 7PO3 in ethanol (solid curve) and in crystal state (dash-dotted curve).

	$\lambda^{abs}_{n\pi^*}$ (nm)	$\lambda^{abs}_{\pi\pi^*}$ (nm)	$\lambda^{lum}_{\pi\pi^*}$ (nm)	$\Delta\lambda^{abs}_{n\pi^*}$ (nm)	$\Delta\lambda^{abs}_{\pi\pi^*}$ (nm)	$\Delta\lambda^{lum}_{\pi\pi^*}$ (nm)
DPO I*	–	294	353	–	14	4
DPO II	–	–	353	–	–	4
6DPO6 I	–	–	405	–	–	0
6DPO6 II†	–	346	412	–	10	7
6DPO4	281	353	433	17	29	8
7PO3	315	332	395	12	−13	10

Tab. 6.2: Absorption and emission maxima of the investigated crystals. *The absorption spectrum was measured in a sample which contained mainly DPO I crystals with a low percentage of DPO II crystals. †Both absorption and emission spectra were acquired from a mixture of 6DPO6 I and 6DPO6 II crystals (21% and 79% in mass, respectively, according to X-ray investigations). $\Delta\lambda$ indicates the red shift of the absorption and emission bands of the crystals in relation to the solutions.

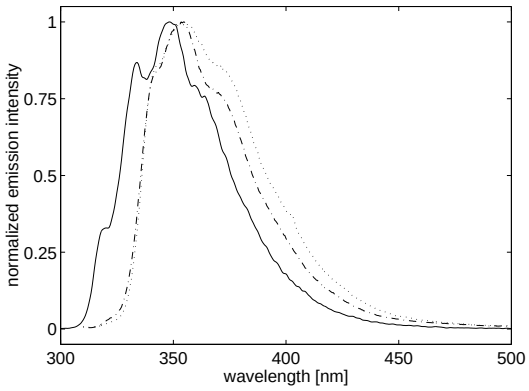

Fig. 6.11: Emission spectra of DPO in ethanol (solid curve), of DPO I crystals (dash-dotted curve), and of DPO II crystals (dotted curve).

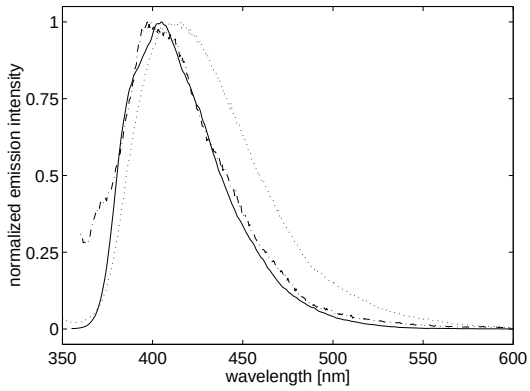

Fig. 6.12: Emission spectra of 6DPO6 in ethanol (solid curve), of 6DPO6 I crystals (dash-dotted curve), and of a mixture of 6DPO6 I and 6DPO6 II crystals (21% and 79% in mass, respectively, according to X-ray investigations) (dotted curve).

the fluorescence is significantly shorter than that of the absorption. This induces the decrease of the Stokes shift.

There are several reasons for the red shift. One of them, at the *molecular* level, is the increased conjugation of the π electron system of the molecule in the crystal compared with the dissolved molecule. It results from the nearly planar geometry that the molecule adopts in the crystal (both in S_0 and in S_1)[§]. When the wave functions of the π electrons of the molecule overlap more, i.e. when the conjugation increases, the bandwidth of the delocalized S_0 and S_1 increases, which leads to a lowering of the transition energy [115, 120, 145]. This effect may affect 6DPO6 I less than the other crystals since it is built by relatively less conjugated molecules (cf. §3.4.3).

Another cause for the red shift of the absorption spectrum is the 'gas to crystal' effect, which acts at the *super-molecular* level. Following the model explained by Birks [11], the first approximation to a molecular crystal is an 'oriented gas', that is, a system of N oriented but non interacting molecules. The state associated with the excitation of one molecule of the 'oriented gas' is N-fold degenerated because the energy of the system does not depend on which particular molecule is excited. Since in a real crystal the excited molecule interacts with its unexcited neighbours, the

[§]In fact, the dissolved molecules are not planar because their rings can rotate freely around the molecular axis.

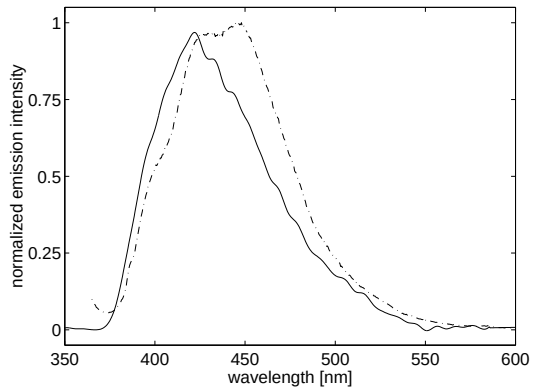

Fig. 6.13: Emission spectra of 6DPO4 in ethanol (solid curve) and in crystal state (dash-dotted curve).

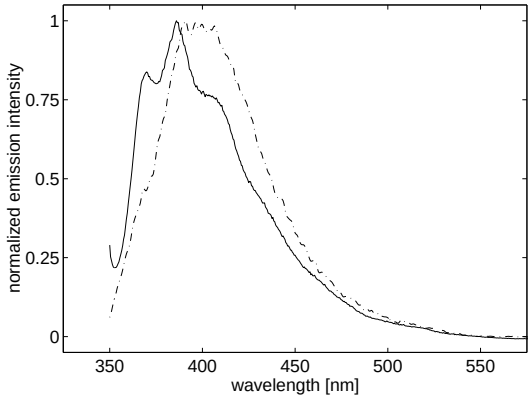

Fig. 6.14: Emission spectra of 7PO3 in ethanol (solid curve) and in crystal state (dash-dotted curve).

uncertainty principle forbids the existence of a true stationary state of the undeformed crystal with the excitation localized at only one molecule. If ΔW is the interaction energy, the lifetime of a molecular excitation against migration to another place in the crystal is of the order of $h/\Delta W$, where h is Planck's constant. The electronic excitation energy may migrate through the crystal until it is emitted or degraded radiationlessly. Therefore, the inter-molecular interactions remove the N-fold degeneracy of the system leading to delocalized states over the whole crystal.

The energy of an excited state in a crystal with two molecules in the unit cell is of the form:

$$E_c = E_0 + S + C \pm B \tag{6.1}$$

where E_0 is the energy of an isolated molecule; S is the solvent shift due to the polarizability of the environment; C is the shift due to the interactions with translationally equivalent molecules; and $2B$ is the Davidov splitting factor which results from the interactions with translationally inequivalent molecules. When there are more than two molecules per unit cell, B has to be substituted by B_j, a term which takes into account the different kinds of interactions between the molecules. Since S, C and B_j may be positive or negative, the energy of an excited state in a crystal may be higher or lower than that of an isolated molecule. This is illustrated in fig. 6.15.

Following the previous model, the super-molecular contribution to the red shift of the absorption and emission spectra of the investigated crystals results partly from the influence of the surrounding as a continuum (S) and partly from the interaction between neighbours (C and B_j). In general, the poor quality of the solid state spectra prevents to distinguish between the different terms [11].

The electronic transitions of the investigated crystals have nπ^* or $\pi\pi^*$ character (cf. §6.2.1), that is, they involve n and π electrons. Thus, they are principally influenced by those inter-molecular interactions which affect these electrons. Since n orbitals are more localized than π orbitals, nπ^* are less easily influenced than $\pi\pi^*$ transitions, in agreement with the experimental results (see table 6.2).

In all investigated crystals the molecules arrange parallel to each other (cf. §3.4). This arrangement favours a certain overlap of the wave functions of neighbouring molecules. Hence, the π electrons of the molecules which build the crystals will be further delocalized in relation to those of the dissolved molecules. The increased delocalization of the electrons implies a broadening of the energy levels, which involves a decrease of the transition energy [60]. Thus, the inter-molecular interactions imply not only the red shift of the absorption and emission spectra but also their broadening. Since there are more accessible states, many energetically different transitions may

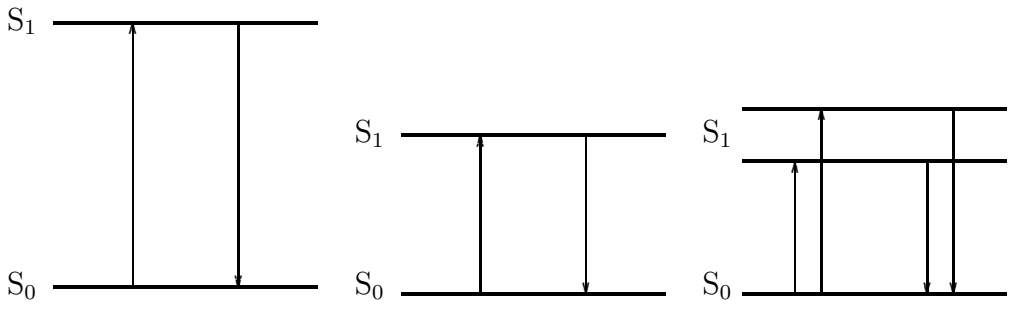

(a) Oriented gas.

(b) Crystal with one molecule per unit cell.

(c) Crystal with two molecules per unit cell.

Fig. 6.15: Energy scheme illustrating the shifts and splittings in the first excited electronic state of the crystal relative to the oriented gas. (a) Degenerated S_1 level for oriented and non interacting molecules; $E(S_1) = E_0$. (b) Shift of S_1 resulting from the environment polarizability (S) and from the interactions between the excited molecule and translationally equivalent molecules (C); $E(S_1) = E_0 + S + C$. (c) Davidov splitting of S_1 as result of the interactions between the excited molecule and translationally inequivalent molecules (B); $E(S_1) = E_0 + S + C \pm B$.

occur. The reason for the surprising behaviour of the absorption and emission spectra of 7PO3 is still not clear. One possible explanation for the blue shift of the $\pi\pi^*$ absorption band is the formation of dimers in the solution which may be more tightly bonded (energetically more stable) than those of the crystal.

The decrease of the Stokes shift of the crystal compared with the solution is caused by the absence of a strong relaxation process in the crystal. As is discussed above, the solution spectrum shows an abnormally large Stokes shift as consequence of the solvent effect and the planarization of the molecule in S_1. Since in the crystal the molecule is planar both in S_0 and in S_1, the relaxation process is weaker than in the solution. This effect also explains why the absorption band of the crystal spectrum is more red shifted in relation to the solution spectrum than the fluorescence band. Since the absorption of the solution occurs to the non relaxed Franck-Condon state, the energy difference between this state and the excited state of the crystal is large. Contrarily, the fluorescence of the solution occurs from a strongly relaxed state whose energy differs not so much from that of the excited state of the crystal . Consequently, the red shift of the absorption is larger than that of the fluorescence. Finally, the fluorescence band is not as broad as the absorption band because of the internal conversion from the high vibrational states to the lowest vibrational state prior to the emission.

Figure 6.11 compares the emission spectra of the two polymorphs of DPO. In spite of having different crystal structures, DPO I and DPO II share the same fluorescence spectra, with only small disagreements in the relative intensities of the different transitions[¶]. The molecular conformations of DPO I and of DPO II are slightly different, e.g. the inter-ring bond lengths are 0.1444(4) and 0.1459(4) nm for DPO I; and 0.1462 nm in average for DPO II (table C.3). Supposing that the inter-molecular interactions are identical, this difference in the molecular conformation may induce a red shift of the spectrum of DPO I in relation to DPO II. Since this does not occur, we believe that differences of the inter-ring bonds by 0.0011 nm scarcely influence the electronic states of the molecule. The assumption that the inter-molecular interactions are identical in both polymorphs (rigorously they are only very similar) is justified by the molecular arrangement of both crystals as commented in §3.4.1 and §3.4.2. Thus, the modifications of the band structures resulting from the

[¶]The apparent red shift of the emission band of DPO II in relation to DPO I is just the result of the intensity differences between the spectra (fig. 6.11).

inter-molecular forces may be very similar for both polymorphs, as the similarity of the spectra confirms. Although a different Davidov splitting is expected for DPO I than for DPO II, this could not be determined from the spectrum. Therefore, we conclude that the Davidov splitting factor for both crystals is very small according to the weakness of the inter-molecular interactions between molecules of different stacks (translationally inequivalent molecules).

6.5 Summary

The absorption and fluorescence investigations on the oxadiazole compounds can be summarized in the following statements.

(i) The oxadiazole compounds show two absorption bands in the UV range both in solution and in crystal state. The long-wave band corresponds to $\pi\pi^*$ transitions delocalized along the entire molecule. The short-wave band results from $n\pi^*$ transitions localized at the hetero-atoms of the oxadiazole ring and the possible substituents. The excitation at the $\pi\pi^*$ absorption band induces an intense fluorescence in the UV and blue range.

(ii) The solutions show abnormally large Stokes shifts due to the relaxation of the molecule in S_1. The most important factor contributing to this relaxation is the planarization that the molecule undergoes in S_1.

(iii) The absorption and emission spectra of the oxadiazole compounds in crystalline form do not show new bands in relation to the spectra of the solution. Therefore, the individual molecule rules to a large extent the optical properties of the crystal.

(iv) The transition from solution to crystal is accompanied by a red shift of both absorption and emission spectra and by a broadening of the absorption bands. The red shift of the absorption bands lies between 10 and 29 nm depending on the substance and on the transition: $\pi\pi^*$ transitions shift slightly larger than $n\pi^*$ transitions. Nevertheless, it should be noted that the great overlap between both bands in some cases complicates the correct estimation of the red shift for the short-wave band. The emission shows smaller red shifts than the absorption, between 4 and 10 nm. Several factors produce these red shifts: the broadening of S_0 and S_1 results from the increased conjugation of the nearly planar molecules building the crystal (molecular level); the 'gas to crystal effect' due to the environment polarizability and to the inter-molecular interactions within the crystal (super-molecular level). Precisely the inter-molecular interactions between translationally equivalent molecules (e.g. the π-π interactions within the π complexes) is believed to be the most important factor. The weak interactions between translationally inequivalent molecules may have nearly no influence on the electronic transitions since no important Davidov splitting could be observed.

Chapter 7

Electronic transitions under compression

7.1 Introduction

The basic effect of pressure is to decrease the inter-atomic spacings of a system, thus increasing the overlap between adjacent electronic orbitals. As is shown in §4.4, a molecular crystal subjected to compression may or may not undergo a phase transition. Even in the case where no phase transition occurs, drastic modifications in the electronic energy levels are induced by high pressure because the overlap of the electronic wave functions is strongly affected by small changes of the inter-atomic spacings. Since pressure affects the energy levels in a solid without introducing chemical changes, it is an attractive tool for the study of optical properties. Conversely, the study of the optical properties at high pressure is also a valuable tool to gain information about the compression mechanism.

In the previous chapter the optical properties of the oxadiazole compounds were investigated at ambient pressure. Here we focus on the effect of high pressure (up to 5-7 GPa) upon the absorption and fluorescence of the crystals.

7.2 Literature review

As we have noted in the previous chapter (§6.2), no previous publications on the electronic transitions of oxadiazole crystals apart from those connected with the present work [62, 136] are found in the literature. The same is true for the high pressure investigations in this field. As reference point for our studies, we discuss briefly those results found for other aromatic compounds.

7.2.1 Oligo(para-phenylene)s and poly(para-phenylene)s

In the last two years the groups of Puschnig, Chandrasekhar, Heimel, and Yang published several articles about the influence of high pressure on the electronic and vibrational properties of solid films of oligo(para-phenylene)s and poly(para-phenylene)s [60, 115, 118, 119, 145]. In [60] the authors deduce the nature of the geometry changes from their influence on the electronic and vibrational transitions by comparing experimental results and three-dimensional density functional calculations performed with the Wien97 code [116]. Here we focus on the results concerning the electronic structure.

The oligo(para-phenylene)s—up to a length of six phenyl groups—build polycrystalline films

while the methylated ladder-type poly(para-phenylene) (m-LPPP)—the chosen poly(para-phenylene)—is an amorphous film. For all materials, a red shift and a broadening of the absorption and fluorescence spectra with increasing pressure was observed. The absorption is much broader than the fluorescence. The pressure coefficient of the energy shift varies between 0.1 and 0.4 eV/GPa depending on the material, which corresponds well to the theoretical values.

The authors describe the red shift and broadening of the bands as the combination of two effects. Firstly, the enlargement in the conjugation of the molecule which induces a red shift but no broadening of the curves. The major conjugation results from the planarization of the molecule and from the shortening of the inter-ring bonds. And secondly, the increase in the inter-molecular interactions which induces a blue shift and a broadening of the spectra.

Although the effect of conjugation may be generalized to similar aromatic molecules such as the oxadiazole compounds, the effect of the decrease of the inter-molecular spacings depends on the molecular arrangement of the system.

7.2.2 Aromatic carbonyl derivatives in polymeric media

The group of Drickamer and Dreger has published a great number of articles about the photophysics and photo-chemistry of several organic materials under compression [146, 147, 148, 149, 150, 151, 152, 153, 154, 155]. Moreover Drickamer has authored a monograph about the high pressure chemistry and physics of solids from the point of view of their electronic transitions [156]. Because of the difference between the oxadiazole compounds and the substances studied by these authors (aromatic aldehydes, ketones and nitriles mostly dissolved in polymeric media), here we reproduce only some of their general statements.

(i) $\pi\pi^*$ emissions show significant shifts to lower energy with pressure because the molecule is much more polarizable when an electron is in the excited $\pi\pi^*$ state. Contrarily $n\pi^*$ emissions show relatively small shifts because the difference in polarizabilities of the molecule in the excited $n\pi^*$ and ground state is much smaller.

(ii) Under compression, fluorescence shifts four or five times more strongly to lower energy than phosphorescence because the repulsion between parallel spins limits the polarizability of the excited state for the triplet.

(iii) $\pi\pi^*$ emissions are much more intense under compression—often by several orders of magnitude—than the corresponding $n\pi^*$ emissions because of the poor orbital overlap in the latter case.

7.2.3 Poly(para-phenylene-vinylene)

In a very interesting article, Webster and Batchelder studied the absorption, luminescence and Raman spectra of poly(para-phenylene-vinylene) (PPV) at high pressure [157]. In this case the absorption band shows a red shift with pressure. Up to 3 GPa the shift is linear, reversible with no hysteresis and does not depend on the pressure transmitting fluid. Two factors are responsible for the red shift: the increase in the average conjugation length and the 'gas-to-crystal' shift. The second one consists in the lowering of the exciton energy as a result of the polarisation of the surrounding medium.

The luminescence also shows a red shift under compression with approximately the same rate as that observed for the absorption. Additionally, the vibronic structure of the emission band disappears and the intensity decreases strongly. Another observed effect is the slight shift to lower energies of the weighting of the intensity. The pressure transmitting fluids have no effect neither on the rate of the red shift nor on the change in the shape of the spectrum, but they have a very important effect on the rate at which the luminescence extinguishes. The authors explain

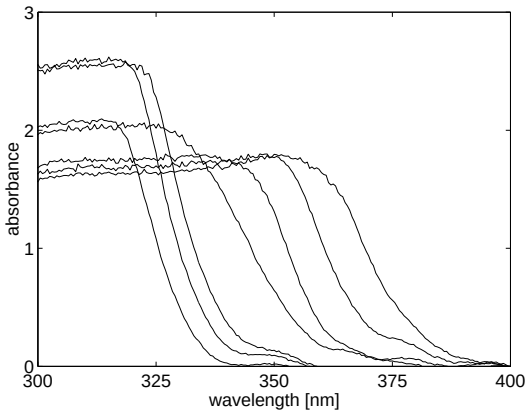

Fig. 7.1: Absorption spectra of DPO I crystals at different pressures, from left to right: 0.5, 1.5, 2.5, 3.3, 4.3, 5.8, and 7.2 GPa.

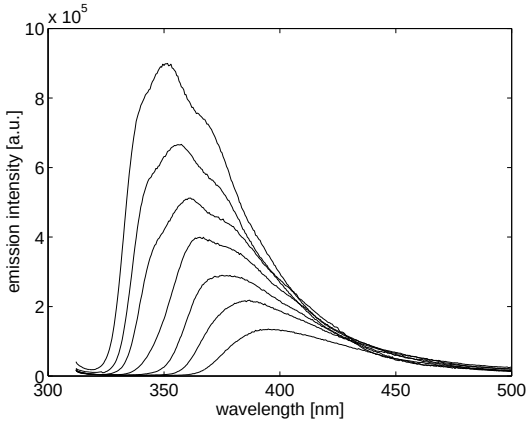

Fig. 7.2: Emission spectra of DPO I crystals at different pressures, from top to bottom: 0.5, 1.5, 2.5, 3.3, 4.3, 5.8, and 7.2 GPa.

the luminescence quenching under compression as a result of the increase of various phenomena: multi-phonon emission, defect quenching, formation of charge transfer excitons, and formation of excimers with pressure . Some of these causes can be extrapolated to monomeric crystals like the oxadiazole compounds.

7.3 Absorption and emission spectra under compression

As in the experiments at ambient pressure, the large thickness of the crystals disturbed the measurement of the absorption spectra*. Additional effects such as diffraction at small crystals, and reflection at crystal surfaces, at the gasket hole and at the diamonds surfaces disturb the signal (for a more detailed discussion see §2.3.2). Thus, only the onset of the absorption at long wavelengths could be acquired. As an example, some absorption spectra of DPO I at different pressures, up to 7.2 GPa, are shown in fig. 7.1. The behaviour of the long-wave edge suggests a red shift of the absorption spectrum under compression. This phenomenon appears in all investigated crystals.

The acquisition of the emission spectrum under compression presented smaller difficulties. In all the investigated variants of oxadiazole crystals, a red shift of the fluorescence spectrum accompanied by a decrease of the intensity occurs. The behaviour of the emission of DPO I under compression is shown in fig. 7.2. In all the investigated crystals except in 6DPO4 the shape of the emission band changes slightly under compression. The short wavelength edge looses its sharpness progressively with pressure due to the decrease of the inner filter effects. Thus, it can be concluded that the red shift of the absorption is not as large as that of the fluorescence, which implies an increase in the Stokes shift under compression. For 6DPO4 the shape of its emission band does not vary under compression because the Stokes shift is already large at ambient pressure, that is, there are nearly no inner filter effects in the whole pressure range investigated. Nevertheless, it should be remarked that the distortion of the emission band by the inner filter effects is only perceptible in the foot of the short-wave edge. Therefore it does not affect the width of the curves at e.g. 70% of its maximum, which we use as characteristic value. Taking into account this width, we conclude that the emission band does not suffer a broadening under compression unlike similar compounds (cf. §7.2.1).

In DPO I a further effect modifies the shape of its emission spectrum at high pressures. The

*The optical measurements of 6DPO6 I were performed from a crystal achieved from the sublimation.

most intense peak of the spectrum shifts slightly more rapidly than its shoulder at longer wavelengths. From 4 GPa the superposition between peak and shoulder complicates the resolution of the latter, for this reason we concentrate on the position of the peak (see fig. 7.2).

When pressure is released, the absorption and fluorescence spectra return to their initial position. Moreover, the emission bands also recover their shape and intensity (within the experimental limits).

7.4 Shift of the transition energy under compression

The red shift of the absorption and emission spectra was quantified by the position of the onset of the absorption and of the emission maximum, respectively. There are two standard manners to evaluate the position of the onset of the absorption [158]. These procedures where first introduced in semiconductor physics where they are used to determine the energy gap. One is the so called 'tangent method' which consists of determining the intersection between two tangent lines to the curve: one in the part of total or nearly total transparency and another in the part where the absorbance shows the steep slope. In the other method the position of the onset of the absorption is simply determined by the wavelength corresponding to a constant value of the absorbance (e.g. at 70% of its maximum). It is obvious that the *absolute* position of the absorption onset depends upon the applied procedure. Indeed, in the second method it additionally depends on the absorbance value chosen to determine the wavelength. However, we compared both methods for some of our spectra and realized that the magnitude of the pressure-induced shift is independent of the procedure followed for the evaluation of the onset position. We chose the second method in our studies and focus our attention only on the energy shift.

Figures 7.3 to 7.7 show the energy shifts of both the absorption onset and the fluorescence peak of the oxadiazole crystals with pressure. The experimental values[†] are well described by the following relations:

DPO I :	$E_{abs}(eV)$	=	$3.86 - 0.032p$	$p \in [0, 3.1]$ GPa
	$E_{abs}(eV)$	=	$3.84 - 0.065p$	$p \in [3.3, 7.2]$ GPa
	$E_{lum}(eV)$	=	$3.57 - 0.061p$	$p \in [0, 7.2]$ GPa
DPO II :	$E_{abs}(eV)$	=	$3.90 - 0.070p + 0.004p^2$	$p \in [0, 5.4]$ GPa
	$E_{lum}(eV)$	=	$3.55 - 0.118p + 0.008p^2$	$p \in [0, 5.4]$ GPa
6DPO6 I :	$E_{abs}(eV)$	=	$3.23 - 0.058p$	$p \in [0, 5.4]$ GPa
	$E_{lum}(eV)$	=	$3.08 - 0.063p$	$p \in [0, 5.4]$ GPa
6DPO4 :	$E_{abs}(eV)$	=	$3.22 - 0.036p$	$p \in [0, 5.7]$ GPa
	$E_{lum}(eV)$	=	$2.88 - 0.043p$	$p \in [0, 5.7]$ GPa
7PO3 :	$E_{abs}(eV)$	=	$3.50 - 0.035p$	$p \in [0, 4.8]$ GPa
	$E_{lum}(eV)$	=	$3.15 - 0.116p + 0.009p^2$	$p \in [0, 4.8]$ GPa

For the evaluation of the shift of the absorption edge of DPO I, the pressure range was divided into two intervals. One up to 3.1 GPa, where the absorbance maxima are very large and hence the curves show a sharp edge; a second range 3.1 GPa from 7.2 GPa, where the absorbance is lower and consequently the curves reproduce properly the long edge of the absorption. The reason for the difference between the pressure coefficients of the absorption edge shifts in the two intervals are not clear. We believe that they are related to the modification of the shape of the curves which may originate from experimental influences (e.g. intensity of the light source, fiber coupling).

After having observed that the absorption spectra of the crystals are broader than the spectra measured for the substances in solution (cf. §6.4), we can expect a further broadening under compression. Also, an increased band width with pressure has already been reported for phenylene

[†]The experimental absorption onsets and fluorescence maxima at high pressure of all investigated compounds are summarized in tables G.1 to G.5

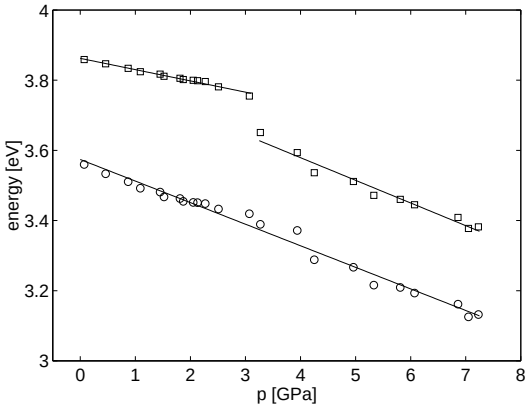

Fig. 7.3: Energy shift of the absorption (□) and emission (◯) of DPO I crystals as a function of pressure. The shift of the absorption was determined at 70% of its maximum and that of the emission at the maximum. The lines correspond to the fits described in the text.

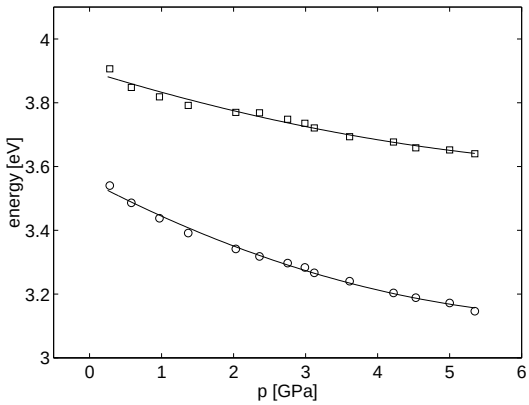

Fig. 7.4: Energy shift of the absorption (□) and emission (◯) of DPO II crystals as a function of pressure. The shift of the absorption was determined at 70% of its maximum and that of the emission at the maximum. The lines correspond to the fits described in the text.

derivatives (cf. §7.2.1). Such a broadening may imply a more intense shift of the absorption edge than of the absorption maximum. But, although the shift of the absorption edge is not a precise measure for the shift of the absorption maximum, it gives at least an idea about the order of magnitude of the real shift. On the other side, the shift of the emission band is quite well estimated. Though the experimental error in the measure of the emission spectra may be up to 2.5 nm (see §2.3.2), it should be constant for a compression run and therefore it affects only the absolute position of the emission maximum and not its shift. Nevertheless, it has to be noted that the maximum position determined for the first compression step matches up rather well with that determined at ambient pressure (compare table 6.2 for the ambient pressure data with tables G.1 to G.5 for the high pressure data). The error in the estimation of the maximum position, which affects the shift, is not larger than 1 nm.

Our interpretation of the red shift of both absorption and fluorescence spectra under compression is basically the same as that proposed for the red shift of the spectra of the crystals in relation to the solutions discussed in §6.4 which, in turn, agrees with the generally accepted argument [60, 115, 145, 146, 147, 148, 149, 150, 151, 152, 153, 154, 155, 157] (cf. §7.2). There are two causes for the decrease of the transition energy under compression. On the one hand, at the *molecular* level, a possible increase of the conjugation of the π system along the molecule may occur. On the other hand, at the *super-molecular* level, the interactions between molecules become more intense.

An increase of the conjugation may result from the planarization of the molecule and/or from the shortening of the inter-ring bonds under compression. Unfortunately, there are no data about the modification of the molecular conformation with pressure. As is pointed out in §4.5, we used the rigid body approximation for the analysis of the crystal structure under compression. Such procedure is justified by the high conjugation of the molecules of the crystals already at ambient pressure. In other words, the molecules which build the crystals show high planarity and short inter-ring bonds which yields a rigid character (see §3.3). However, although to neglect possible small modifications of the molecular conformation barely influences the results concerning the lattice parameters, such modifications should be taken into account when studying the electronic transitions of the crystals under compression. Small changes of the molecular conformation may strongly influence the absorption and emission characteristics [60, 115, 145]. In the case of all crystals investigated here, with the exception of 6DPO6 I, a possible planarization of the molecules

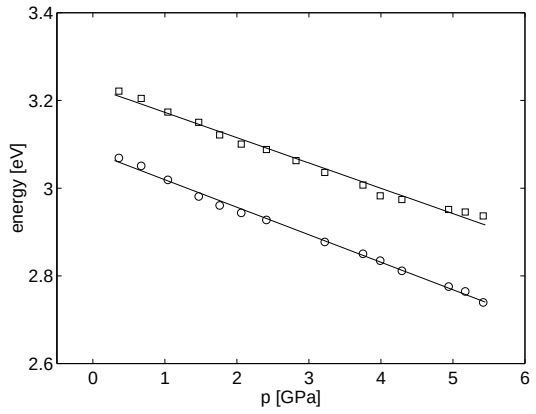

Fig. 7.5: Energy shift of the absorption (□) and emission (◯) of 6DPO6 I crystals as a function of pressure. The shift of the absorption was determined at 70% of its maximum and that of the emission at the maximum. The lines correspond to the fits described in the text.

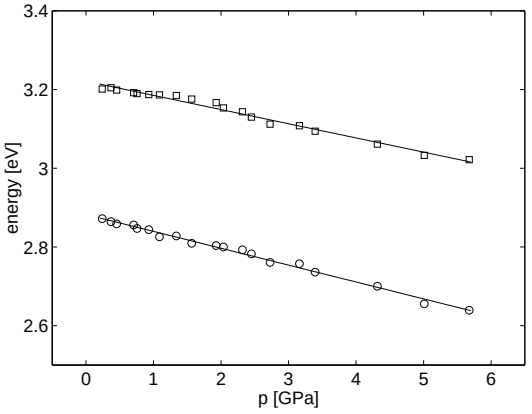

Fig. 7.6: Energy shift of the absorption (□) and emission (◯) of 6DPO4 crystals as a function of pressure. The shift of the absorption was determined at 60% of its maximum and that of the emission at the maximum. The lines correspond to the fits described in the text.

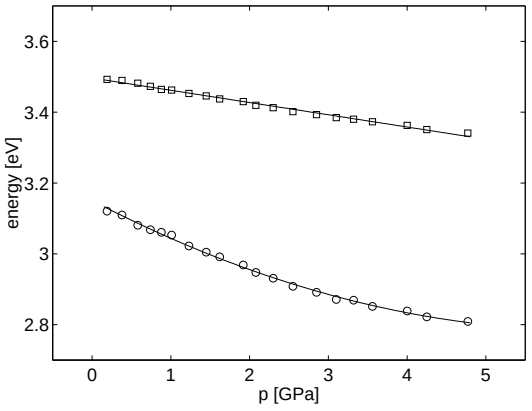

Fig. 7.7: Energy shift of the absorption (□) and emission (◯) of 7PO3 crystals as a function of pressure. The shift of the absorption was determined at 70% of its maximum and that of the emission at the maximum. The lines correspond to the fits described in the text.

under compression should be negligible since the molecules are already nearly perfectly planar at ambient pressure (cf. table C.3). Therefore, the only influence on the transition energy at the molecular level could be the shortening of the inter-ring bonds. This point deserves a deeper comment. As is indicated in §4.2.1, 1DPO1 shows a maximal modification of the inter-ring bonds of 0.005 nm among the different phases that the crystal adopts up to 2.9 GPa. The similarity between the investigated compounds and 1DPO1 leads us to expect a shortening of the inter-ring bond of our molecules of the same order of magnitude. On the other side, comparison of the emission bands of DPO I and DPO II at ambient pressure, indicates that differences of the inter-ring bonds by 0.001 nm do not modify the spectra (cf. §6.4). Thus, we believe that the possible small shortening of the inter-ring bonds under compression only lightly modifies the electronic transition energy of the oxadiazole crystals.

Across the present pressure range, the influences on the electronic transition energy at the molecular level should be small. The decisive factor inducing the red shift of the absorption and emission spectra is therefore due to the increased intensity of the inter-molecular interactions within the crystal. The lowering in the transition energy results principally from the enlarged interaction of the π systems of the molecules. In the case of DPO I, such interaction could be quantified by the distance between the molecules of a stack, that is, of an infinite π-complex. In §4.6.1 the diminution of the stack axis length under compression is approximated by a linear relation in pressure (a=0.55203-0.0077p, where a is expressed in nm and p in GPa). Assuming that the orientation of the molecules to the stack axis is preserved under compression, it suffices to multiply a by $\sin\varphi$ (φ being the herring bone angle, in this case, 41°) to obtain the inter-molecular distance within a π-complex (cf. §3.4.1). Thus, knowing the decrease of the transition energy with pressure, it is easy to calculate its dependence on the inter-molecular distance. It turns out that the transition energy of DPO I diminishes by approximately 1.2 eV when the molecules are joined by 0.1 nm. This result has to be considered just as a first approximation since: (i) the influence of the shortening of the inter-ring bonds, though small, should not be completely neglected; (ii) other super-molecular influences such as the interactions between molecules of different stacks were not considered; (iii) the herring bone angle may slightly change under compression (cf. §4.6.1).

In the discussion of the behaviour of the lattice parameters of 6DPO6 I under compression it is proposed that the molecules of the stacks slightly modify their relative position around 3.2 GPa. This involves a decrease in the overlap among their oxadiazole rings (see §4.6.3). It should be kept in mind that the stacking of 6DPO6 I only involves the oxadiazole rings and not the whole molecules (cf. §3.4.3). Thus, slight modifications of the relative position of these rings may not strongly influence the electronic transitions of the substance. The fact that the energy transition shows no discontinuities in the whole pressure range confirms that slight changes in the relative arrangement of the molecules barely influence the electronic transitions of this crystal.

From the study of the evolution of the absorption edge and the emission maximum of 6DPO4 under compression some information about the mechanisms of the phase transitions may be gained. In §4.4.1 we proposed that the close molecular packing of 6DPO4 with stacks of infinite π-complexes may only allow topotactical reactions, that is, the stacks should be maintained during the phase transitions. Since the energy decrease of the electronic transitions occurs continuously with pressure, the overlap of the π systems of adjacent molecules and hence the geometry of the π-complexes may not suffer abrupt changes under compression. Thus, from the optical investigations it can be concluded that the π-complexes are maintained through the different phases. Hence, the phase transitions are topotactical reactions.

7.5 Emission quenching under compression

As an example, the decrease of the intensity of the emission spectra with pressure of DPO I and 6DPO6 I is shown in fig. 7.8 and 7.9, respectively. For all the investigated crystals, the decrease of intensity corresponds well to an exponential decay.

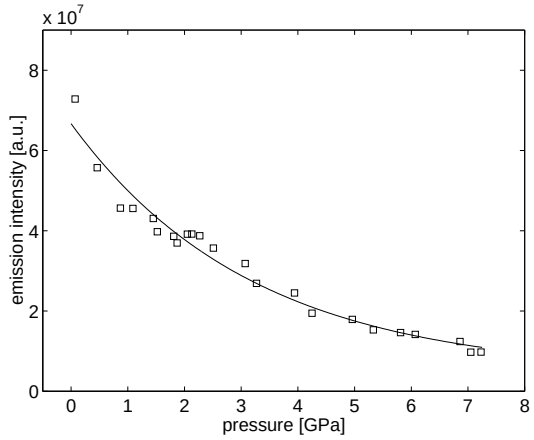

Fig. 7.8: Decrease of the emission intensity of DPO I crystals as a function of pressure. The line corresponds to an exponential decay.

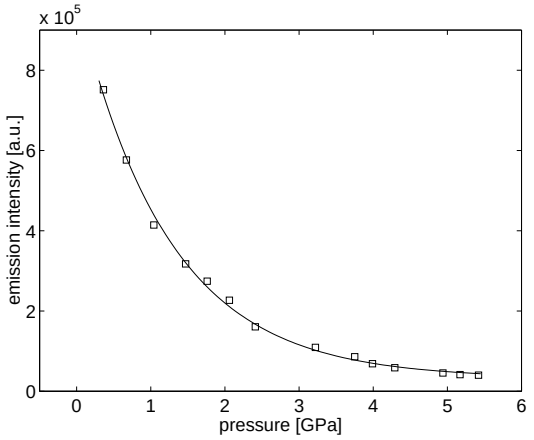

Fig. 7.9: Decrease of the emission intensity of 6DPO6 I crystals as a function of pressure. The line corresponds to an exponential decay.

One factor is the diminution of the transition energy which favours the thermal deactivation of the excited state. Two further factors connected with the presence of quenching sites are relevant. Firstly, the number of quenching sites, defects in the crystal, increases under compression. Secondly, as result of the enhanced orbital overlap, the electronic mobility increases, which leads to a mayor probability of occupation of the quenching sites. Webster and Batchelder propose similar effects to explain the luminescence quenching found in PPV under compression [157] (cf. §7.2.3). In order to determine the relative influence of the different causes time-resolved measurements are necessary.

The formation of excimers, favored at high pressure, might also influence the fluorescence quenching [157]. Excimers possess long radiative lifetimes and a broad, featureless emission that is red shifted from the emission of the isolated exciton. However, excimer emission was not observed in the oxadiazole crystals under compression.

7.6 Relations among oxadiazoles, and to other organic compounds

The decrease of the electronic transition energy due to compression is quite similar for all investigated substances (cf. §7.4). Since the different crystals are characterized by both different molecules and different crystal structures, it is not possible to compare their energy shifts with pressure in more detail. Only in the case of the two polymorphs of DPO a comparison of the shifts of the emission band is possible. Although they are built by the same molecule, the red shift of the emission of DPO II is slightly more intense than that of DPO I. This is due to the differences in the compression behaviour of these crystals (cf. §4.6.1 and §4.6.2). It seems that the overlap between the π systems of the molecules of a π-complex increases more strongly with pressure in DPO II than in DPO I. Due to the complex molecular arrangement of DPO II and to its anisotropic response to compression (cf. §3.4.2 and §4.6.2), a relation between the energy shift and the inter-molecular distance similar to that proposed for DPO I could not be determined.

The energy shift that the oxadiazole crystals suffer under compression is slightly larger, but of the same order of magnitude, than that found for other organic materials. Chandrasekhar et al. and Yang et al. reported the following pressure coefficients for the red shifts of the absorption

and the 0-0 and 0-1 luminescence of m-LPPP: −0.038, −0.027, and −0.021 eV/GPa determined up to 8 GPa [60, 145], while Puschnig et al. found an absorption shift of polycrystalline biphenyl of −0.016 eV/GPa from measurements up to 0.3 GPa [115] (see also §7.2.1). Similar values are reported by Rossi et al. for oligo(tiophene)s: −0.024 and −0.040 eV/GPa measured up to 0.4 GPa. The reason for the relatively large red shift of the oxadiazole crystals is the easy way in which their π-orbitals are influenced by pressure. This results from the particular super-molecular structure of these crystals (e.g. the stack-like arrangement of DPO I, DPO II, 6DPO6 I, and 6DPO4 and the arrangement in pairs of 7PO3).

7.7 Summary

The investigation of the absorption and emission characteristics of oxadiazole crystals under compression can be summarized as follows.

(i) The application of high pressure to the crystals induces a red shift of both absorption and emission spectra. The magnitude of the energy shift calculated for the absorption onset is rather similar to that of the emission maximum. The pressure coefficient of the shifts vary between 0.04 and 0.06 eV/GPa, depending on the crystal. There are two reasons for the decrease in the transition energy: at the molecular level, a possible increase in the conjugation of the molecule originated by the enhanced planarity of the molecules and/or the shortening of the inter-ring bonds under compression; at the super-molecular level, an increase in the inter-molecular interactions. The second cause is believed to have a greater influence than the first one due to the already partial conjugation of the molecules at ambient pressure.

(ii) The shape of the emission band is nearly not influenced by high pressure. An exception to this is DPO I where the fluorescence peak shifts stronger than its shoulder. On the other hand, in most of the investigated crystals the short-wave edge of the fluorescence band is slightly modified under compression due to the decrease of the inner filter effects, i.e. the Stokes shift increases slightly under compression. However, the width of the curves at 70% of their maximum value is maintained under compression.

(iii) The emission intensity suffers an exponential decay with pressure. The fluorescence quenching under compression is due to several factors: the promotion of the multi-phonon emission that results from the decrease in the energy difference between excited and ground state; the increase of the number of defects in the crystal which act as quenching sites; the enhanced electron mobility to quenching sites under compression resulting from the increased orbital overlap.

(iv) The previous effects seem reversible within certain experimental limits.

(v) In the case of DPO I the emission energy could be related to the inter-molecular spacing between the molecules of the infinite π-complexes. In a rough approximation, the transition energy decreases by 1.2 eV when the molecules are joined by 0.1 nm.

(vi) The oxadiazole crystals are characterized by slightly more intense shifts of the electronic transition energy with pressure than similar organic materials.

Chapter 8

Raman modes at normal conditions and under compression

8.1 Introduction

The infrared and Raman spectra of a substance give complementary information about the vibrations of the molecules within the crystal (lattice modes) and those of the atoms within the molecules (internal modes). Forbidden modes in infrared may be seen in Raman and vice versa. Vibrational spectroscopy can be used to identify and analyze substances as well as to determine molecular conformations. Additionally, when dealing with solids it gives some information about the super-molecular structure, allowing to distinguish between amorphous and crystalline solids and between different crystalline states.

The study of the response of the vibrational spectrum of a substance to pressure is a rapid and precise way to determine possible phase transitions. In addition, it gives a decisive contribution to the determination of a complete equation of state for the crystal. High pressure Raman spectroscopy is technically less complicated to perform than high pressure infrared spectroscopy and therefore it is more common. The present chapter deals with the Raman spectra of the investigated crystals and their compressional behaviour.

8.2 Literature review

Although the infrared modes of a great number of organic substances are well characterized (see for instance [159, 160]), not much is known about their Raman modes. The infrared and Raman spectra of the pure 1,3,4-oxadiazole ring (a liquid) and its deuterated species were experimentally studied by Christensen et al. and Anthonsen et al. [161, 162, 163] and theoretically by El-Azhary [164, 165]. The Raman spectra of some oxadiazole derivatives were investigated by Milone et al. [166, 167, 168, 169, 170]. The cited references helped us in assigning frequencies to our compounds.

As is pointed out above, Raman spectroscopy is a convenient technique for the determination of pressure-induced phase transitions. Most of the studies on organic substances are devoted to this task and to the characterization of the shift of the Raman lines with pressure [39, 157, 171, 172, 173]. In recent years, the combination of experimental results with lattice dynamics [90, 91, 92, 93, 97, 98] and three-dimensional band structure calculations [60, 118, 119, 145], and indeed just with density functional calculations of isolated molecules [121, 174] allowed to understand the compression process of some organic compounds, such as oligo and poly(paraphenylenes) and anthracence derivatives as well as benzene. In the following we give a more

detailed account of prior studies which regard oxadiazole compounds.

8.2.1 POD

Orgzall et al. combined infrared and Raman spectroscopy of the two modifications of poly(p-phenylene-1,3,4-oxadiazole) (POD) and some of its oligomers with molecular modeling calculations [175]. These authors showed that the α- and β-modifications result from different contents of cis- and trans-conformers in POD. Comparing the Raman and infrared modes of the oligomers with increasing chain length with the modeling results the authors could identify the most intense lines with vibrations of the oxadiazole, phenyl, and phenylene rings. In their molecular modeling calculation they assumed a planar molecular structure for the oligomer. This assumption is opposite to that proposed by Hofmann et al. which also investigated POD [176]. However, the good agreement of the experimental and calculated vibrational spectra supports the idea of planar molecules. These results constitute the base for our own investigations.

8.2.2 1DPO1

As is indicated in §4.2.1, Orgzall et al. investigated 1DPO1 up to 5 GPa [63]. They report that the spectral pattern of 1DPO1 shows remarkable changes at certain pressures. The changes are more important in the lattice than in the internal modes. The gap between lattice and internal modes becomes smaller at high pressure but it still exists.

From the study of the shift that the Raman modes experience under compression, the authors determined the following transition pressures: 0.88, 1.28 and 2.2 GPa. The different phase transitions are marked by discontinuities in the line shift. Some lines vanish and new ones appear. All transitions are reversible with only small hysteresis up to 0.2 GPa. The Raman lines of 1DPO1 show a shift to higher frequency with pressure. The shift was quantified for the internal modes in the first phase. Their pressure coefficient is between 2 and 4 cm^{-1}/GPa, as usual for organic compounds [173].

8.3 Raman spectra at normal conditions

In order to classify the vibrational modes, one can follow different ways. When dealing with simple molecules (e.g. benzol) it is possible to perform *ab initio* calculations. The vibrational frequencies obtained this way are usually in good agreement with the experimental results. Such calculations were performed by El-Azhary for the isolated 1,3,4-oxadiazole ring [164, 165]. Unfortunately, for complex molecules like those investigated here such a method provides still only approximative results.

The classification of the vibrational modes of complex compounds can only be performed as a first approximation by the comparison with analogous substances, particularly with well known model compounds. With this purpose several 1,3,4-oxadiazole derivatives were analysed in the frame of this work. Thus, for the interpretation of the Raman spectra we use the 'block' principle. It assumes that given units of the complex molecule mark through vibrations in particular and relatively well-limited intervals of frequencies. The exact position of a given mode is only slightly influenced by the specific intra- and inter-molecular interactions which result from the different chemical substitution and crystal structure.

The spectra of all the investigated compounds share principally the same structure in the finger print region below 2000 cm^{-1} (see fig. 8.1 for an example). There are strong and very strong bands in three regions. Between these regions only medium and weak lines appear. In the following only the three important regions are discussed. The first region corresponds to the lattice vibrations.

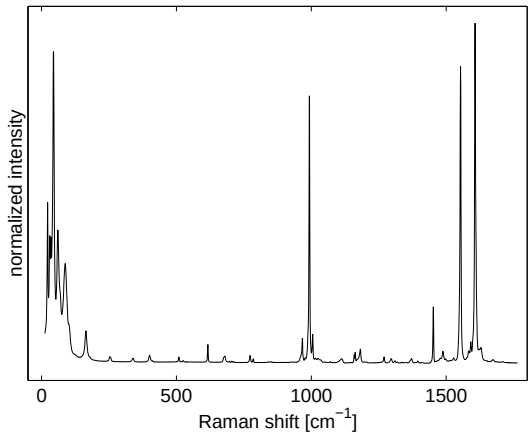

Fig. 8.1: Raman spectrum of DPO I.

It goes up to around 200 or 300 cm^{-1}, depending on the substance. The other two regions contain internal modes; one around 1000 cm^{-1} and the other between 1450 and 1650 cm^{-1}.

8.3.1 Lattice modes

As the investigated substances are crystals, they show intense and relatively sharp bands in the region of the lattice vibrations (see fig. 8.2 to 8.5). However, also rather broad structures appear which result from the superposition of several modes. In general the most sharp and intense modes appear at frequencies lower than 100 cm^{-1}. Each crystal shows a strongly different structure in this region preventing a systematic assignment of the bands. Every crystal has to be treated separately. It is precisely this feature of the lattice modes which allows to use Raman spectroscopy to discriminate between different structures, e.g. different polymorphs (DPO I and DPO II) or pseudo-polymorphs (6DPO6 I and 6DPO6 II), and indeed to determine the appearance of phase transitions under pressure or temperature (cf. §5.3.1, §5.3.2 and §8.4.1).

8.3.2 The region around 1000 cm^{-1}

The spectrum shape in the region around 1000 cm^{-1} depends strongly on the substitution of the oxadiazole ring. In substances where the 1,3,4-oxadiazole ring is substituted by two phenyl(ene) rings as DPO I, DPO II, 6DPO6 I, 6DPO6 II, and 6DPO4, this region is principally characterized by three bands (cf. fig. 8.6, 8.7, and 8.8, and table H.1). The most intense one, normally very close to 994 cm^{-1}, has strong or very strong intensity. The other bands are around 967 and 1015 cm^{-1}. When the oxadiazole ring is substituted by a phenylene ring and an alkyl group as 7PO3, the Raman spectrum in the region around 1000 cm^{-1} is characterized by three groups of lines with medium or weak intensity around 952, 974, and 1042 cm^{-1} (cf. fig. 8.9 and table H.1). Due to these differences we describe these two groups of substances separately.

8.3.2.1 DPO I, DPO II, 6DPO6 I, 6DPO6 II, and 6DPO4

As indicated above, the most intense line of this region of DPO derivatives is located at 994±2 cm^{-1}. It corresponds to a ring deformation vibration of the diaryl substituted 1,3,4-oxadiazole as can be deduced by comparison with the literature [166, 167, 168, 169, 170]. Its position remains nearly unaffected by modification of the substitution pattern at the phenylene rings. This intense band

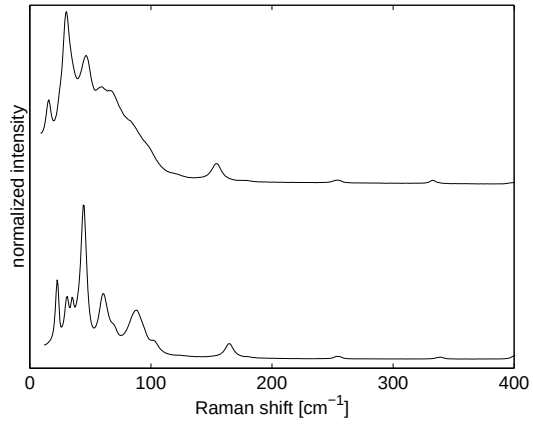

Fig. 8.2: Raman spectrum of DPO I (bottom) and DPO II (top) in the region of the lattice vibrations. There are significant differences between the spectra which indicate that the substances differ in their crystal structure.

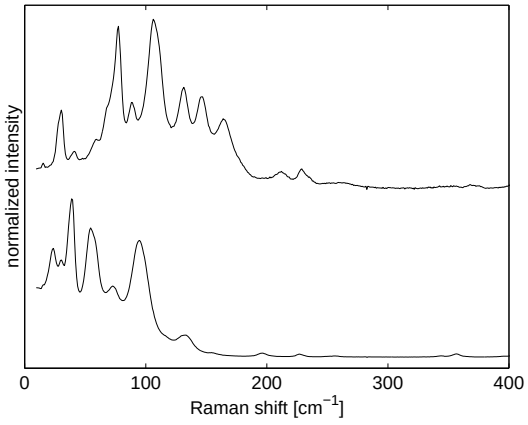

Fig. 8.3: Raman spectrum of 6DPO6 I (bottom) and 6DPO6 II (top) in the region of the lattice vibrations. There are significant differences between the spectra which indicate that the substances differ in their crystal structure.

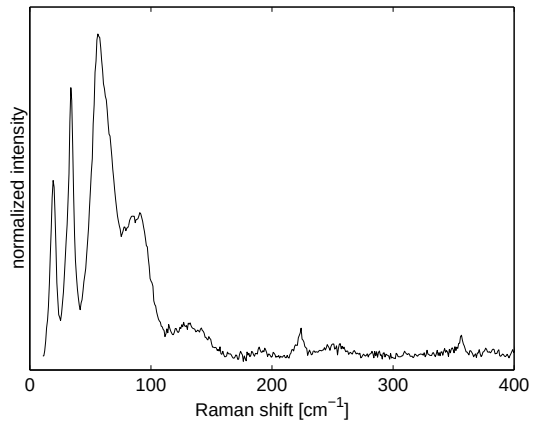

Fig. 8.4: Raman spectrum of 6DPO4 in the region of the lattice vibrations.

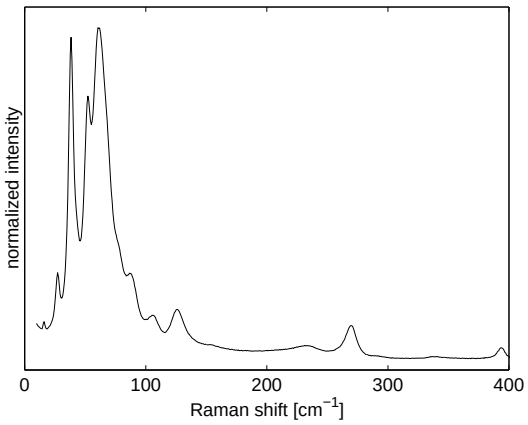

Fig. 8.5: Raman spectrum of 7PO3 in the region of the lattice vibrations.

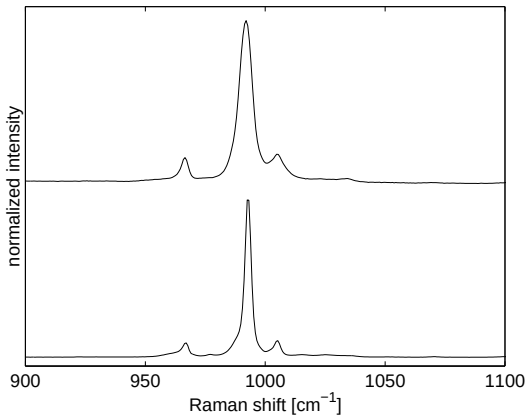

Fig. 8.6: Raman spectrum of DPO I (bottom) and DPO II (top) in the region of the internal vibrations around 1000 cm^{-1}. Both spectra are identical. This indicates that the molecular vibrations of both substances are influenced in the same way by the super-molecular arrangement.

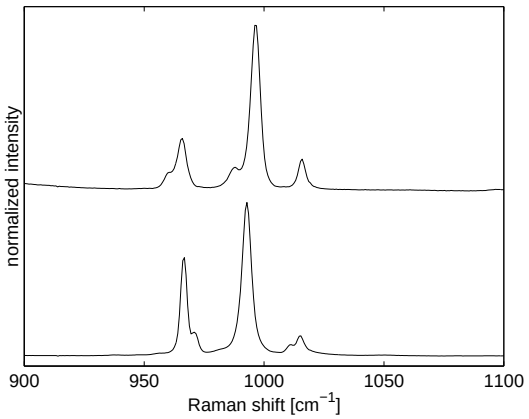

Fig. 8.7: Raman spectrum of 6DPO6 I (bottom) and 6DPO6 II (top) in the region of the internal vibrations around 1000 cm^{-1}. There are small differences between the spectra indicating that the molecular vibrations of both substances are influenced in a different way by the super-molecular arrangement.

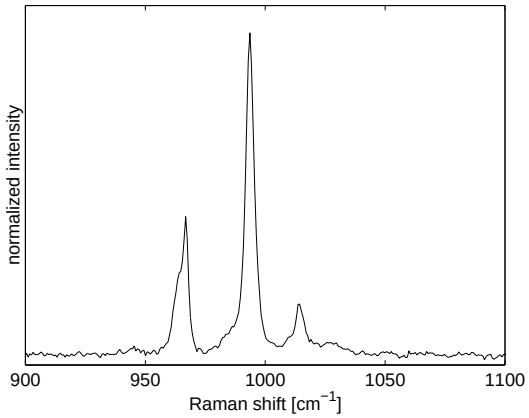

Fig. 8.8: Raman spectrum of 6DPO4 in the region of the internal vibrations around 1000 cm^{-1}.

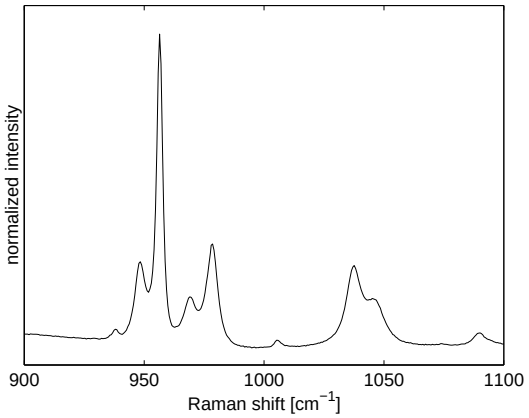

Fig. 8.9: Raman spectrum of 7PO3 in the region of the internal vibrations around 1000 cm^{-1}.

can show a weak shoulder at lower frequencies (cf. table H.1).

The other bands are identified as ring deformation vibrations of the phenyl(ene) rings and as CH out-of-plane wagging as explained in the following. From the literature it is known that the unsubstituted benzene shows two lines in this region: at 1011 and 992 cm^{-1} [160]. In the 1011 cm^{-1} mode all C atoms move radially and alternate atoms move outwards and inwards. This is the in-plane bending by sextants. In the 992 cm^{-1} mode all the C atoms move in-phase radially. This is the in-phase stretching or breathing vibration. For mono-, meta-, and 1,3,5-trisubstitution these modes belong to the same symmetry species and can mix to give a mode around 1000 cm^{-1}. Such a mode is only expected in DPO I and DPO II. Thus, the lines which these substances show at 1005 cm^{-1} is associated with this mode (cf. table H.1). Though in the literature these lines are described as strong, in DPO I and DPO II they only show weak intensity [160].

Contrarily, for ortho- and para-disubstituted phenylene rings the benzene in-plane bending by sextants and in-phase ring stretching modes at 1011 and 992 cm^{-1}, respectively, belong to different symmetry species and cannot mix. This explains why no vibration is found around 1005 cm^{-1} for the para-disubstituted phenylene rings of 6DPO6 I, 6DPO6 II, and 6DPO4 (and also 7PO3).

Substituted as well as unsubstituted phenyl(ene) rings should show lines in the regions 1012±9 and 960±30 cm^{-1}. These modes describe the CH in-plane and out-of-plane bending of the ring [160]. According to this, we propose that the weak or very weak line that our substances have at 1015±2 cm^{-1} corresponds to the CH in-plane bending of the phenyl(ene) ring (see table H.1). In the same way, the CH out-of-plane bending of the ring may be represented by the line with medium or weak intensity which appears in the region 967±2 cm^{-1} (cf. table H.1). These lines show a weak or very weak shoulder generally at lower frequencies. The shoulder may be associated with a CH out-of-plane wagging vibration which is expected at 965±10 cm^{-1} [160].

8.3.2.2 7PO3

The most intense band of 7PO3 in this region is also attributed to the oxadiazole ring. Following the literature the alkyl-aryl substituted 1,3,4-oxadiazole ring has two lines in this region: at 950±10 cm^{-1} and at 1030±10 cm^{-1} [166, 167, 168, 169, 170]. Thus, the lines at 948 and 957 cm^{-1} with weak and medium intensity, respectively, and those at 1037 and 1046 cm^{-1} with weak and very weak intensity correspond to vibrations of the oxadiazole ring. The reasons for apparition of double lines are not clear. One of the lines might result from the CH in-plane and out-of-plane bending vibrations of the phenylene ring.

The other lines of 7PO3 in this region are at 969 and 978 cm^{-1} and have very weak and weak intensity, respectively. In the same way as for the DPO derivatives explained above, these lines are identified with the CH out-of-plane bending of the phenylene ring.

8.3.3 The region around 1600 cm^{-1}

All substances show the most intense lines in the third region, between 1450 and 1650 cm^{-1} (see fig. 8.10 to 8.13, and table H.1). Typically, there are two lines with very strong intensity and the remaining ones have a medium intensity.

The literature reports two modes for the unsubstituted 1,3,4-oxadiazole ring in this region: one at 1536 cm^{-1} with very strong intensity and another at 1495 cm^{-1} with medium intensity [161, 162]. These bands shift slightly by modification of the substituents. Thus, the ring modes should be found at 1542 and 1479 cm^{-1} for diaryl substitution and at 1546 and 1482 cm^{-1} for alkyl-aryl substitution. Following this, the very strong line which DPO I and DPO II show around 1553 cm^{-1} and 6DPO6 I, 6DPO6 II, and 6DPO4 in the range 1563...1569 cm^{-1} correspond to a diaryl substituted oxadiazole ring vibration (cf. table H.1). In an analogous way, though the line that 7PO3 shows at 1557 cm^{-1} has only weak intensity, it may be a mode of the alkyl-aryl substituted oxadiazole ring.

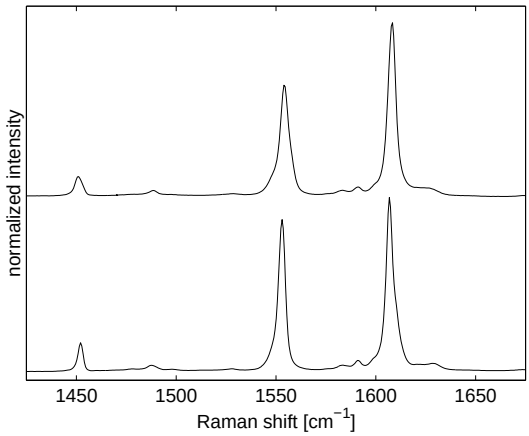

Fig. 8.10: Raman spectrum of DPO I (bottom) and DPO II (top) in the region of the internal vibrations between 1400 and 1700 cm^{-1}. Both spectra match very closely. This indicates that the molecular vibrations of both substances are influenced in the same way by the super-molecular arrangement.

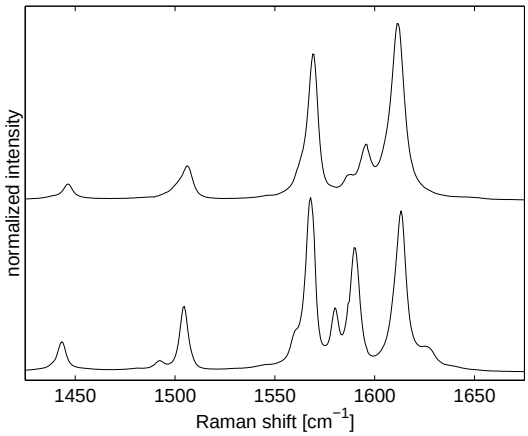

Fig. 8.11: Raman spectrum of 6DPO6 I (bottom) and 6DPO6 II (top) in the region of the internal vibrations between 1400 and 1700 cm^{-1}. There are small differences between the spectra indicating that the molecular vibrations of both substances are influenced in a different way by the super-molecular arrangement.

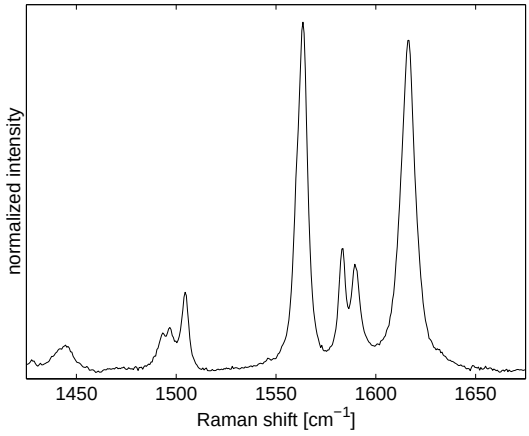

Fig. 8.12: Raman spectrum of 6DPO4 in the region of the internal vibrations between 1400 and 1700 cm^{-1}.

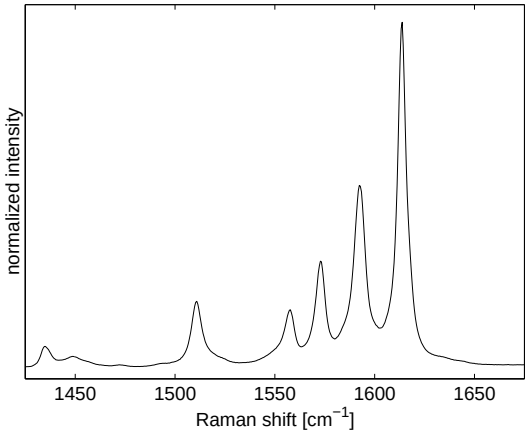

Fig. 8.13: Raman spectrum of 7PO3 in the region of the internal vibrations between 1400 and 1700 cm^{-1}.

The second expected oxadiazole vibration in this region may be the weak or very weak mode that all substances show in the range 1488...1511 cm^{-1} (cf. table H.1). However, since the semi-circle stretch vibration of the benzene ring marks at 1486 cm^{-1} [160], it cannot be excluded that the previous bands at 1488...1511 cm^{-1} originate from the phenyl(ene) ring or from both oxadiazole and phenyl(ene) rings.

The unsubstituted benzene ring has two vibrations in this region. Both are double degenerated [160]. One of them is the quadrant stretch at 1596 cm^{-1}. The other one is the semi-circle stretch at 1486 cm^{-1}, which should be only very weak in Raman. The degeneration is broken when substituents are added. The lines split more or less depending on the perturbation.

The quadrant and semi-circle stretch vibrations can be described as follows. Separating the ring into quadrants by nodal lines, in the quadrant stretch vibrations the ring C-C bonds that are predominantly in one quadrant stretch, while those in the neighbouring quadrants contract. In a similar way, the semi-circle stretch vibrations can be described tracing a nodal line which divides the ring into two semi-circles. Thus, in the semi-circle vibration the ring C-C bonds that are in one semi-circle stretch, while those in the other contract. A ring bond that is bisected by a nodal line does not change in length. The quadrant stretch modes interact with in-plane C-H bending and this interaction is strong in the two semi-circle stretch modes [160].

When the phenyl ring is mono-substituted as in DPO I and DPO II, these modes loose their degeneration splitting into two lines at approximately 1600 and 1580 cm^{-1} for the quadrant stretch modes and around 1500 and 1450 cm^{-1} for the semi-circle stretch modes. Therefore, the very strong lines of DPO I and DPO II around 1607 cm^{-1} and the weak lines at 1591 cm^{-1} correspond to the quadrant stretch modes (cf. table H.1). Both lines show very weak shoulders. Although the spectra of DPO I and DPO II show a medium line at 1452 cm^{-1} and a weak line at 1488 cm^{-1} (which could be linked to the semi-circle stretch modes), such an assignment cannot be made with security since such lines should be very weak in a Raman analysis. Additionally, as is indicated above, the line at 1488 cm^{-1} may as well be an oxadiazole ring vibration.

In the case of having para-disubstituted phenylene rings, the quadrant modes mark at approximately 1600 and 1580 cm^{-1}, while the semi-circle modes mark around 1510 and 1410 cm^{-1}. Thus, the lines of 6DPO6 I, 6DPO6 II, 6DPO4, and 7PO3 at 1590...1599 cm^{-1} with strong and medium intensity and those at 1611...1616 cm^{-1} with very strong intensity are identified as the quadrant modes (see table H.1). As previously, the identification of the group of frequencies around 1505 and 1444 cm^{-1} with the semi-circle stretch vibration cannot be given with security.

The weak line that some substances show around 1627 cm^{-1} might be associated with a CH scissoring vibration [160] (see table H.1).

8.3.4 Relations between DPO I and DPO II and between 6DPO6 I and 6DPO6 II

It is interesting to investigate the influence that the super-molecular order has on the vibrations of the molecules. To do this, we can compare the internal modes of the two polymorphs of DPO and those of the two modifications of 6DPO6.

Comparison of the internal modes of DPO I and DPO II shows a perfect agreement in the line positions and intensities (cf. fig. 8.6 and 8.10, and table H.1). This is due to the similarity of the inter-molecular interactions in both crystals. As is described in §3.4.1 and in §3.4.2, the DPO molecules of both polymorphs interact with their neighbours principally through π-π forces between the phenyl and oxadiazole rings within the infinite π-complexes and additionally through van der Waals interactions and weak H-bonds between perpendicular rings.

However, the internal modes of the water-free and water-containing modifications of 6DPO6 show slight differences (see fig. 8.7 and 8.11, and table H.1). The most intense mode of the region around 1000 cm^{-1}, the one associated with the diaryl substituted 1,3,4-oxadiazole ring, is slightly

shifted in 6DPO6 II in relation to 6DPO6 I and the remaining substances. While in 6DPO6 I this vibration marks at 993 cm^{-1}, in 6DPO6 II the corresponding line splits in a strong line at 996 cm^{-1} and a weak one at 987 cm^{-1}. Another difference between these two polymorphs occurs in one of the quadrant stretch modes of the phenylene ring. In 6DPO6 I this vibration marks at 1590 cm^{-1}, while in 6DPO6 II it marks at 1596 cm^{-1}. These differences in the location of the ring vibrations are caused by the different inter-molecular interactions to which the 6DPO6 molecules are subjected in the two crystals (see §3.4.3 and §3.4.4). Particularly, the H-bond between the NH_2 groups of 6DPO6 and the water molecules in 6DPO6 II is sufficiently strong to influence the ring vibrations. Additionally, 6DPO6 II shows a broad structure around 850 cm^{-1}, not present in 6DPO6 I.

8.4 Raman spectra under compression

Similarly as in the X-ray investigation under compression (see §4.4), we begin our study with the comparison of the Raman spectra of a given crystal at different pressures up to approximately 6 GPa. When a substance undergoes phase transitions, major differences in its vibrational spectrum occur [173]. This is a consequence of the differences between the space groups and hence between the selection rules of the two phases. The comparison shows that 6DPO4 is the only crystal which undergoes important changes in its spectrum as is commented below in more detail. Thus, the high pressure Raman investigation confirms the observation concluded from the X-ray study: among the investigated crystals only 6DPO4 undergoes pressure-induced phase transitions (see §4.4).

All studied substances show shifts of the vibrational modes to higher frequencies and a general intensity decrease and background increase under compression. The shifts are continuous for all substances with the exception of 6DPO4 which shows discontinuities in the pressure ranges where the phase transitions occur, principally in the lattice modes. The frequency shift is fully reversible and free of hysteresis, while the other effects, the intensity decrease and background increase, show just a slight irreversibility.

Figures 8.14 to 8.16 show the frequency shift of selected Raman lines of DPO I (those lines discussed in the previous sections). The other compounds which do not undergo phase transitions show a similar behaviour*. In the present pressure range most modes—especially the lattice modes—can be described by a quadratic function of pressure. Such a function reproduces well the saturation of the shift which sometimes appears in the last steps of the compression†. The increase in the vibrational frequencies can be explained by the anharmonicity of the vibrations [171, 173]. When the crystal is compressed, the inter-atomic distances decrease resulting in an increase in the effective force constants and therefore in the vibrational frequencies. The sub-linearity in the shift of the Raman modes is a consequence of the non linear compressibility of the crystal (as is explained in §4.7, the compression of the crystals is well described by the non linear MEOS). The shifts of the lattice modes are mostly one order of magnitude larger than those of the internal modes (see tables I.7 to I.12). This confirms the intuitive idea that during the compression the molecules as a whole approximate more strongly than the atoms within the molecules, e.g. the shortening of the lattice parameters is more intense than that of the molecular bonds.

The second effect, the intensity decrease with compression, results from a slight increase of the amorphous portion under compression. It turns out that at high pressure the number of defects in the crystal structure increases. In §7.5 an increased number of defects in the crystal is proposed as a possible cause for the fluorescence quenching under compression. From the Raman experiments such increment of the number of quenching sites can be confirmed.

*The experimental values of the Raman frequencies at different pressures of all crystals are reported in tables I.1 to I.6

†The pressure coefficients which describe the shift are summarized in tables I.7 to I.12

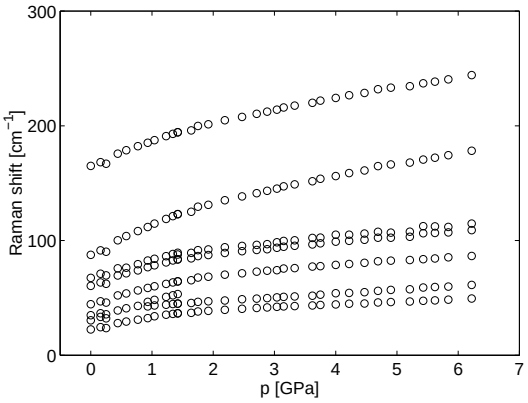

Fig. 8.14: Shift of selected Raman lattice modes of DPO I as a function of pressure. There are no discontinuities in the shifts which indicates that the crystal does not undergo phase transitions under compression.

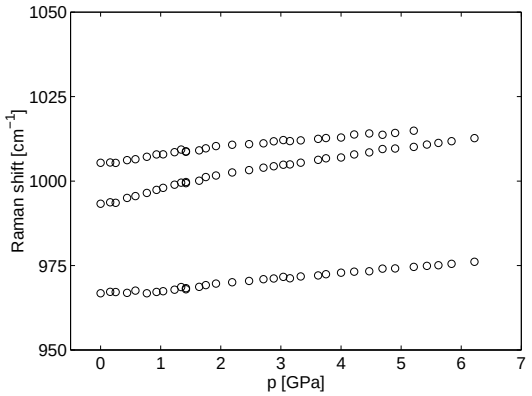

Fig. 8.15: Shift of selected Raman lines of DPO I as a function of pressure in the region around 1000 cm^{-1}.

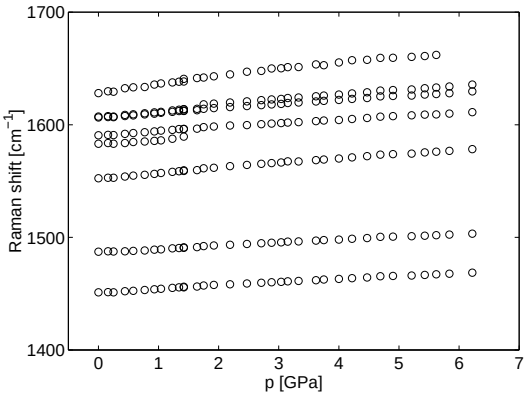

Fig. 8.16: Shift of selected Raman lines of DPO I as a function of pressure in the region between 1400 and 1700 cm^{-1}.

8.4.1 6DPO4

The presence of two phase transitions in 6DPO4 under compression up to 5.5 GPa can be visualized by the modifications of its Raman spectrum. The changes are more pronounced in the lattice than in the internal modes. This is expected because the lattice modes represent the vibrations of the molecules within the crystal. The internal modes of a given molecule depend principally on the molecular constitution and are slightly influenced by the inter-molecular interactions of the molecule with its neighbours. Figures 8.17 and 8.18 show the lattice modes of 6DPO4 in the pressure ranges where the phase transitions occur: 0.1 to 1.0 GPa and 2.2 to 3.1 GPa.

It is interesting to pay attention to the behaviour of the internal modes under compression. All modes show the typical shift to higher frequencies as it occurs in those crystals free of phase transitions. As is already commented above, these shifts result from the anharmonicity of the vibrations. Most modes of 6DPO4 have continuous shifts which indicates that the modification of the surrounding of the atoms—involved in the corresponding vibrations—occurs in a progressive way. However, the mode which is originally located at 994 cm^{-1} shows clear discontinuities between 0.2 and 0.4 GPa and between 2.5 and 2.9 GPa, i.e. in the pressure range of the phase transitions (see fig. 8.19). The modification of this mode in the first compression steps is especially strong and may give information about the phase transition mechanism. From 0 to 0.2 GPa it shows an intense shift to higher frequencies. At around 0.4 GPa this mode increases abruptly its frequency and splits clearly into two lines: a strong one and a weak one at higher frequencies (at ambient pressure it only had a shoulder, also at higher frequencies).

To interpret this effect we recall that the H-bonds in 6DPO6 II show up with a frequency increment and line-splitting of the mode associated with the diaryl substituted oxadiazole vibration around 996 cm^{-1} (cf. §8.3.4). Based on this fact we propose the following explanation for the abrupt shift and splitting of the corresponding line in 6DPO4 (the mode which marks at 994 cm^{-1} at ambient pressure) occurring during the first phase transition. The shift and splitting of the line is due to the formation of inter-molecular H-bonds within the crystal. Such H-bonds probably appear between the terminal groups (NH_2 and OCH_3) of molecules of adjacent stacks. The molecular arrangement of 6DPO4 does not need to be strongly modified to allow this H-bonding, just a small approximation of the parallel stacks along the unit cell axis b suffices (see §3.4.5).

Since the remaining internal modes are nearly not influenced by the phase transitions, we propose that at least the most important inter-molecular interactions are maintained. In 6DPO4 the π-π interactions along the π-complexes are the most intense forces within the crystal (see §3.4.5). Thus, we believe that the π-complexes and consequently the stack-like arrangement are maintained during the phase transitions. It is noteworthy that this conclusion is also deduced from the study of the absorption and emission spectra under compression (cf. §7.4).

Figure 8.20 shows the lattice modes of 6DPO4 before and after the compression. Contrarily to the high pressure X-ray investigation (see §4.4), now the total relaxation of the sample could be achieved. The similarity of the spectra of the initial and relaxed sample indicates the reversibility of the phase transitions. However, as in the other crystals, the quality of the spectrum at high pressures and after the relaxation is lower than at the beginning of the compression (see fig. 8.17, 8.18, and 8.20). This is attributable to increased disorder.

8.5 Complete equation of state

In §4.3 we pointed out that the construction of a complete equation of state for complex solids is in general not possible. One is limited to empirical equations of state which are normally valid for a given temperature like the isothermal MEOS determined for our crystals (cf. §4.7). The temperature effect is then considered as a thermal correction to the equation by means of the thermal expansion coefficient. This could also be done for some of the compounds studied here (cf. §5.4). However, the knowledge of the pressure dependence of both vibrational spectrum and

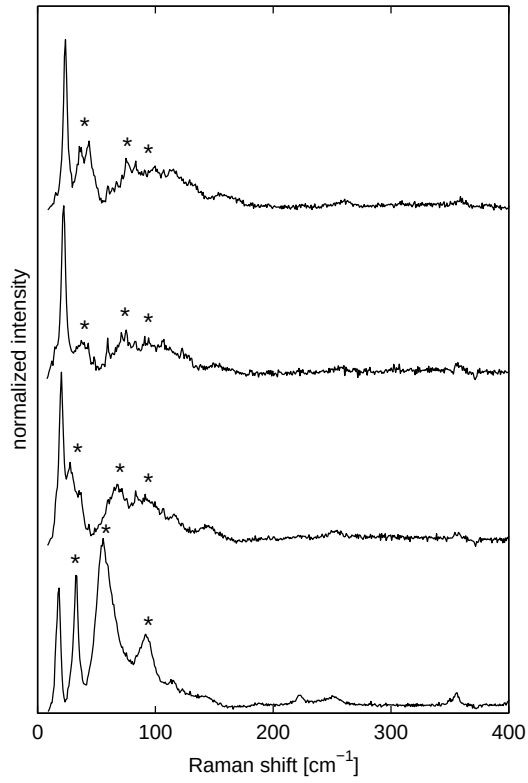

Fig. 8.17: Raman spectrum of 6DPO4 in the region of the lattice vibrations at different pressures, from bottom to top: 0.1, 0.4, 0.7, and 1.0 GPa. The differences in the spectra indicate that the crystal undergoes a phase transition in this pressure range.

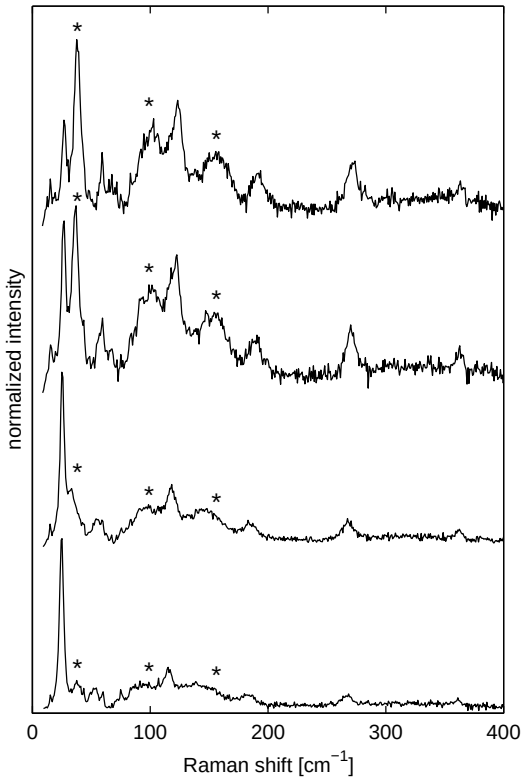

Fig. 8.18: Raman spectrum of 6DPO4 in the region of the lattice vibrations at different pressures, from bottom to top: 2.2, 2.5, 2.9, and 3.1 GPa. The differences in the spectra indicate that the crystal undergoes a phase transition in this pressure range.

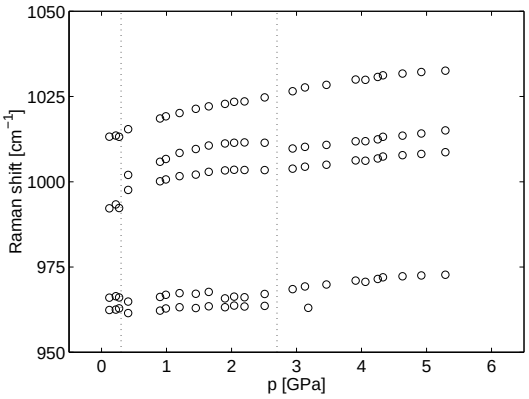

Fig. 8.19: Shift of the Raman lines of 6DPO4 as a function of pressure in the region around 1000 cm^{-1}. There are discontinuities in the shifts which indicates that the crystal undergoes phase transitions under compression. The dotted lines indicate the phase transitions pressures.

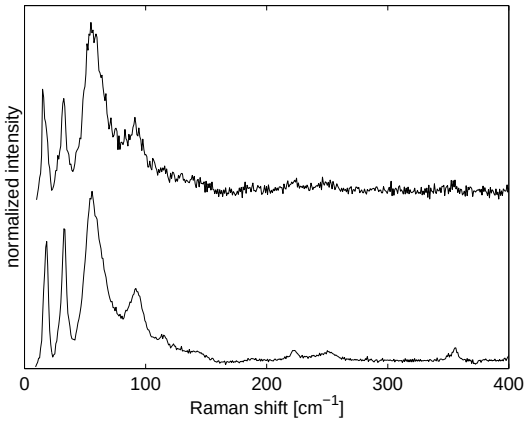

Fig. 8.20: Raman spectrum of 6DPO4 in the region of the lattice vibrations at 0 GPa before (bottom) and after the compression (top). The similarity of the spectra indicates the reversibility of the compression but with slightly increased disorder.

volume of the solid means an important contribution to the construction of a complete equation of state. It follows a description of a very approximative way to achieve a complete EOS for complex solids based on the vibrational Debye model (for a more detailed description see [83, 87, 177, 178, 179]). In spite of imposing rather restrictive assumptions, the Debye model still gives quite satisfactory results and has the advantage of being quite simple. For a discussion of the validity of the Debye model and a proposal of a less restrictive approach see [87, 177, 178, 179].

8.5.1 Debye model

In a crystal at temperatures above absolute zero, atoms vibrate about their equilibrium positions. The crystal can therefore be considered as a collection of oscillators. In the harmonic approximation the vibrations can be described by progressive plane waves like

$$\mathbf{u}(\mathbf{x}, t) = A\,\mathbf{n}\,\sin(\mathbf{k}\,\mathbf{x} - w\,t) \tag{8.1}$$

where $\mathbf{u}(\mathbf{x}, t)$ is the displacement of the medium at the point $\mathbf{x}$ and time t, A is the amplitude of the movement, $\mathbf{n}$ is the direction in which the displacement occurs, $\mathbf{k}$ is the wave vector, and w is the frequency. The frequency w is in general a function of $\mathbf{k}$. The relation between the frequency w and the wave vector $\mathbf{k}$ is called the dispersion relation. The velocity of propagation of the wave, that is, the group velocity v is

$$v = \frac{\mathrm{d}w}{\mathrm{d}k} \tag{8.2}$$

where $k = |\mathbf{k}|$.

In the approximation of Debye the possible frequencies are described by a linear dispersion relation

$$w = \begin{cases} v\,k & : \quad w \leq w_D \\ 0 & : \quad w > w_D \end{cases} \tag{8.3}$$

where $k = |\mathbf{k}|$ and $\mathbf{k}$ is a vector of the reciprocal space. Such a dispersion relation implies that all modes are acoustic ($\lim_{\mathbf{k}\to 0} w = 0$) and propagate with the same velocity v and therefore

that the crystal is elastically isotropic. Additionally, these waves are dispersion free, that is, $v_{group} = v_{phase}$.

The Debye theory also assumes that the vibrational states of the crystal correspond to wave vectors **k** whose tips are uniformly distributed in the reciprocal space. Since the available volume in the reciprocal space increases proportionally to $|k^2|\mathrm{d}k$ (a spherical shell of thickness $\mathrm{d}k$ between k and $k + \mathrm{d}k$), the density of vibrational states, $f(k)$, has the form

$$f(k)\,\mathrm{d}k = 4\pi\, d\, k^2\,\mathrm{d}k \tag{8.4}$$

where d is the density (assumed to be constant) of wave vectors in the reciprocal space.

A crystal consisting of one mole of substance contains nN_A atoms, where n is the number of atoms in the chemical formula and N_A is Avogadro's number. Therefore it has $3nN_A$ normal modes of vibration. Since the wave vectors corresponding to these normal modes span one reciprocal cell, the molar density d of vibrational states in the reciprocal space is

$$d = \frac{3n\,N_A}{V_R} = \frac{3n\,N_A\,V_L}{(2\pi)^3} = \frac{3n\,Z\,V}{(2\pi)^3} \tag{8.5}$$

where V_R is the volume of the reciprocal unit cell (Brillouin zone), V_L the volume of the real unit cell ($V_R = (2\pi)^3/V_L$), Z is the number of formula units in the unit cell, and V is the molar volume of the crystal ($V = N_A V_L/Z$).

Thus, taking into account eq. (8.4) and (8.5) the density of states $g(w)$, expressed in terms of the vibrational frequency $w = v\,k$, can be written

$$g(w)\,\mathrm{d}w = f[k(w)]\,\frac{\mathrm{d}k}{\mathrm{d}w}\,\mathrm{d}w = \frac{3n\,Z\,V}{2\pi^2\,v^3}\,w^2\,\mathrm{d}w = a\,w^2\,\mathrm{d}w \tag{8.6}$$

where a is a parameter which only depends on the propagation velocity v

$$a = \frac{3n\,Z\,V}{2\pi^2\,v^3} \tag{8.7}$$

We see that in the Debye approximation the curve of the density of states versus frequency $g(w)$, e.g. the vibrational spectrum, is parabolic.

In the Debye model, the Brillouin zone is simplified by replacing the actual zone with a sphere of the same volume in the reciprocal space, centered at the origin of the reciprocal lattice. Its radius k_{max} is thus given by

$$\frac{4}{3}\pi\,k_{max}^3 = V_R = \frac{(2\pi)^3}{V_L} \tag{8.8}$$

Corresponding to the maximum wave vector k_{max} there is a maximum frequency w_D given by the dispersion relation $w_D = v\,k_{max}$. Introducing the molar volume V ($V = N_A V_L/Z$), the cutoff frequency w_D can be expressed as

$$w_D = v\,k_{max} = v\,\left(\frac{6\pi^2\,N_A}{Z\,V}\right)^{1/3} \tag{8.9}$$

Thus, the cutoff frequency w_D only depends on the wave velocity v and the molar volume V.

In the limit of the linear continuum approximation, the normal modes are independent, hence the energy of one lattice mode depends only on its frequency w and on the number of quanta of vibration occupying that mode (phonon occupancy). In thermal equilibrium, the phonon occupancy is given by the Bose-Einstein distribution

$$< n(w,T) >= \left[\exp\left(\frac{\hbar\,w}{K_B\,T}\right) - 1\right]^{-1} \tag{8.10}$$

where $\hbar = h/2\pi$ and h is Planck's constant and K_B is Boltzmann's constant. Thus, since the energy per mode is $\hbar\, w$ and there are $g(w)\,\mathrm{d}w$ modes in the frequency range w to $w + \mathrm{d}w$, the energy due to the vibration of the crystal E_{vib} in Debye approximation is (neglecting the zero-point energy)

$$E_{vib} = \int_0^{w_D} < n(w,T) > \hbar\, w\, g(w)\,\mathrm{d}w = \frac{3n\,Z\,V\,\hbar}{2\pi^2\,v^3} \int_0^{w_D} \frac{w^3\,\mathrm{d}w}{\exp\left(\frac{\hbar\, w}{K_B\,T}\right) - 1} \tag{8.11}$$

It is convenient to introduce a non dimensional variable θ_D associated with the cutoff frequency w_D. θ_D is the elastic Debye temperature and is defined by

$$\theta_D = \frac{\hbar\, w_D}{K_B} \tag{8.12}$$

Substituting w_D from eq. (8.9), we have

$$\theta_D = \frac{\hbar\, v}{K_B} \left(\frac{6\pi^2\, N_A}{Z\,V}\right)^{1/3} = \frac{h\, v}{K_B} \left(\frac{3N_A}{4\pi\, Z\,V}\right)^{1/3} \tag{8.13}$$

Thus, defining $x = \hbar w/K_B T$ and $x_D = \theta_D/T$, the vibrational energy E_{vib} (eq. (8.11)) can be expressed as

$$E_{vib} = \frac{3n\,Z\,V\,K_B^4\,T^4}{2\pi^2\,\hbar^3\,v^3} \int_0^{x_D} \frac{x^3\,\mathrm{d}x}{\exp x - 1} = \frac{9n\,N_A\,K_B\,T}{x_D^3} \int_0^{x_D} \frac{x^3\,\mathrm{d}x}{\exp x - 1} \tag{8.14}$$

8.5.2 Mie-Grüneisen equation of state

Now that we have an approximation for the vibrational (e.g. thermal) energy of the solid, we can calculate its total energy and its equation of state. As is mentioned in §4.3, the equation of state is obtained from the thermodynamic potentials. If we choose the Helmholtz free energy F as thermodynamic potential, which has the canonical variables temperature T, volume V, and number of particles N (N is here constant), the equation of state is

$$p = -\left(\frac{\partial F}{\partial V}\right)_T \tag{8.15}$$

Helmholtz free energy F is defined as $F = E - TS$, therefore, let us start with the expression of the energy of the solid. The energy of a solid can be divided into three terms

$$E(V,T) = E_0(V) + E_{vib}(V,T) + E_{e^-}(V,T) \tag{8.16}$$

where E_0 is the cohesive energy at 0 K, that is the energy of the static lattice, E_{vib} is the vibrational energy, and E_{e^-} is the energy of the electronic gas. In our case the electronic contribution E_{e^-} is negligible since we are dealing with insulators. The cohesive energy E_0 may be approximated by a Mie potential like

$$E_0(r) = -\frac{a}{r^m} + \frac{b}{r^n} \tag{8.17}$$

with $n > m$, which can also be written as a function of volume V

$$E_0(V) = -\frac{a}{V^{m/3}} + \frac{b}{V^{n/3}} \tag{8.18}$$

Note that the Lennard-Jones potential is a particular case of the Mie potential with $n = 6$ and $m = 12$.

In the Debye approximation the vibrational energy can be described by eq. (8.14) as a function of temperature T and Debye temperature θ_D.

Thus, a static p_0 and a thermal pressure p_{th} can be defined as

$$p_0 = -\left(\frac{\partial F_0}{\partial V}\right)_T \tag{8.19}$$

where F_0 is the Helmholtz free energy associated to the cohesive energy E_0 and

$$p_{th} = -\left(\frac{\partial F_{vib}}{\partial V}\right)_T \tag{8.20}$$

where F_{vib} is the Helmholtz free energy associated to the vibrational energy E_{vib}.

Since $F_0 = E_0$, the static pressure p_0 at 0 K for a Mie potential (eq. (8.18)) is

$$p_0 = -\left(\frac{\partial E_0}{\partial V}\right)_T = -\frac{\mathrm{d}E_0}{\mathrm{d}V} = -\frac{m\,a}{3}V^{-\left(\frac{m}{3}+1\right)} + \frac{n\,b}{3}V^{-\left(\frac{n}{3}+1\right)} \tag{8.21}$$

The calculation of the thermal pressure p_{th} can be made as follows. The vibrational energy E_{vib} in the approximation of Debye is given by eq. (8.14) and can be written in the more simple form

$$E_{vib} = T\,f\left(\frac{\theta_D}{T}\right) \tag{8.22}$$

From the definition of Helmholtz free energy F ($F = E - TS$) and since the entropy can be expressed as $S = -(\partial F/\partial T)_V$, the vibrational energy E_{vib} is

$$E_{vib} = F_{vib} + T\,S_{vib} = F_{vib} - T\left(\frac{\partial F_{vib}}{\partial T}\right)_V \tag{8.23}$$

which can be demonstrated to be equivalent to

$$E_{vib} = \frac{\mathrm{d}\left(\frac{F_{vib}}{T}\right)}{\mathrm{d}\left(\frac{1}{T}\right)} \tag{8.24}$$

just applying the chain rule.

It is convenient to express F_{vib} also as a function of T and θ_D/T

$$F_{vib} = T\,g\left(\frac{\theta_D}{T}\right) \tag{8.25}$$

The previous expression (eq. (8.25)) can be substituted in eq. (8.24) giving

$$E_{vib} = \frac{\mathrm{d}g\left(\frac{\theta_D}{T}\right)}{\mathrm{d}\left(\frac{\theta_D}{T}\right)}\,\theta_D \tag{8.26}$$

On the other side, using the chain rule, the thermal pressure p_{th} (eq. (8.20)) is

$$p_{th} = -\left(\frac{\partial F_{vib}}{\partial V}\right)_T = -\frac{\mathrm{d}F_{vib}}{\mathrm{d}\theta_D}\frac{\mathrm{d}\theta_D}{\mathrm{d}V} \tag{8.27}$$

Operating on the first term, we obtain

$$\frac{\mathrm{d}F_{vib}}{\mathrm{d}\theta_D} = \frac{\mathrm{d}F_{vib}}{\mathrm{d}\left(\frac{\theta_D}{T}\right)}\frac{\mathrm{d}\left(\frac{\theta_D}{T}\right)}{\mathrm{d}\theta_D} = \frac{1}{T}\frac{\mathrm{d}\left(T\,g\left(\frac{\theta_D}{T}\right)\right)}{\mathrm{d}\left(\frac{\theta_D}{T}\right)} = \frac{\mathrm{d}g\left(\frac{\theta_D}{T}\right)}{\mathrm{d}\left(\frac{\theta_D}{T}\right)} \tag{8.28}$$

what taking eq. (8.26) into account results in

$$\frac{\mathrm{d}F_{vib}}{\mathrm{d}\theta_D} = \frac{E_{vib}}{\theta_D} \tag{8.29}$$

Introducing this in the expression of the thermal pressure p_{th} (eq. (8.27)) we get

$$p_{th} = -\frac{E_{vib}}{\theta_D}\frac{\mathrm{d}\,\theta_D}{\mathrm{d}\,V} \tag{8.30}$$

where the thermal pressure is expressed in terms of known quantities and of the variation of the Debye temperature θ_D with volume. It is convenient to introduce the Debye-Grüneisen parameter γ_D

$$\gamma_D = -\frac{\mathrm{d}\ln\theta_D}{\mathrm{d}\ln V} = -\frac{\mathrm{d}\ln w_D}{\mathrm{d}\ln V} \tag{8.31}$$

Applying the chain rule, it can be demonstrated that

$$\gamma_D = -\frac{\mathrm{d}\ln\theta_D}{\mathrm{d}\ln V} = -\frac{V}{\theta_D}\frac{\mathrm{d}\theta_D}{\mathrm{d}V} \tag{8.32}$$

Thus, the thermal pressure p_{th} is

$$p_{th} = \gamma_D \frac{E_{vib}}{V} \tag{8.33}$$

We achieve then the complete Mie-Grüneisen equation of state

$$p = p_0 + p_{th} = -\frac{\mathrm{d}E_0}{\mathrm{d}V} + \gamma_D \frac{E_{vib}}{V} \tag{8.34}$$

Let us consider separately the different terms of eq. (8.34).

(i) Static pressure $\mathrm{d}E_0/\mathrm{d}V$. This term can be calculated assuming that the crystal has a cohesive energy E_0 described by a potential with known parameters. For instance eq. (8.21) gives the static pressure which results from a Mie potential (see eq. (8.18)).

(ii) Debye-Grüneisen parameter γ_D. As is commented below, this parameter can be estimated from the shift of the Raman modes under compression when an empirical equation of state for the system is already known.

(iii) Vibrational energy E_{vib}. As shown in eq. (8.14), this energy is a function of temperature T and of Debye temperature θ_D. The Debye temperature θ_D—as well as the cutoff frequency w_D—depends on known quantities and on the wave velocity v, which is unknown (see eq. (8.13)). The wave velocity—normally, an average velocity of longitudinal and transversal sound waves—should be determined by Brillouin and neutron scattering.

From the study of the Raman modes of the investigated crystals under compression the dependence of the frequencies on pressure could be determined (see §8.4 and tables I.7 to I.12). On the other hand, from the high pressure X-ray experiments, the relation between pressure and volume could be described by the MEOS and the corresponding bulk moduli were determined (cf. §4.7). Combining these results, the dependence of the Raman frequencies on volume can be easily calculated. Thus, the mode Grüneisen parameters, that is, the analogue to the Debye-Grüneisen parameter for each mode, were determined for the investigated crystals as follows (cf. tables I.7 to I.12).

$$\gamma_i = -\left.\frac{\mathrm{d}\ln w_i}{\mathrm{d}\ln V}\right|_{V_0} = -\left.\frac{K_0}{w_i}\frac{\mathrm{d}w_i}{\mathrm{d}p}\right|_{V_0} \tag{8.35}$$

Knowing the mode Grüneisen parameters γ_i an estimation of the Debye-Grüneisen parameter γ_D should be possible (for instance as a mean value weighted by the real spectrum).

Thus, though the Raman modes only constitute a part of the total vibrational modes (they should be completed with the infrared modes), the relation of their frequencies on pressure combined with the MEOS means an important contribution to the construction of a complete equation of state for the system.

8.6 Summary

The Raman spectroscopical investigation of oxadiazole crystals can be summarized as follows.

(i) The Raman spectrum of the oxadiazole compounds has intense and relatively sharp lattice modes, mostly below 100 cm^{-1} though bands with lower intensity can be found up to 300 cm^{-1}. These modes result from the vibrations of the molecules within the unit cell, i.e. within the layers or stacks. Consequently, they depend strongly on the super-molecular arrangement and are characteristic for each crystal.

(ii) The most intense internal modes are in two regions: around 1000 cm^{-1} and between 1450 and 1650 cm^{-1}. They correspond to different vibrations of the 1,3,4-oxadiazole, phenyl, and phenylene rings. The spectral pattern of these regions varies only slightly in the diphenyl(ene) substituted oxadiazole compounds (DPO I, DPO II, 6DPO6 I, 6DPO6 II, and 6DPO4). However, it shows significantly differences between those and the alkyl-aryl substituted oxadiazole derivative (7PO3).

(iii) DPO I, DPO II, 6DPO6 I, 6DPO6 II, and 7PO3 do not undergo pressure-induced phase transitions at room temperature up to approximately 6 GPa as indicates the continuous modification of their Raman spectra under compression.

(iv) 6DPO4 is the only crystal studied which shows phase transitions under compression at room temperature. From the changes in the lattice modes two phase transitions were determined: one between 0.1 and 1.0 GPa and another between 2.2 and 3.1 GPa. The compression behaviour of the Raman mode at 994 cm^{-1} (at p=0) might indicate the presence of H-bonds between molecules of different stacks in the high pressure phases. Both phase transitions are reversible.

(v) Both lattice and internal modes show a shift to higher frequencies with pressure. It results from an increased anharmonicity of the vibrations. The shift is approximately one order of magnitude larger for the lattice (in the order of 10 cm^{-1}/GPa) than for the internal modes (in the order of 1 cm^{-1}/GPa). This effect is fully reversible.

(vi) The shifts of the Raman modes with pressure could be evaluated as a function of volume using the MEOS obtained from the X-ray studies under compression. Thus, the mode Grüneisen parameter for the Raman modes were determined.

Chapter 9

Summary and Conclusion

The objective of the present study was two-fold. On the one hand, we have attempted to characterize the structural evolution of various 1,3,4-oxadiazole compounds under compression. On the other hand, we have investigated the influence of pressure upon the spectroscopical properties of these materials. Along these lines, a number of experimental analyses was carried out.

Crystal structure

Firstly, the *crystal structure* of the substances at *ambient pressure* was studied. The knowledge of the molecular conformation and super-molecular arrangement of the crystals is of fundamental importance to understand their properties. Moreover, it constitutes the basis for all subsequent high pressure experiments.

We have observed that the 1,3,4-oxadiazole ring is always planar and that the phenyl(ene) rings only show very small deviations from planarity. Besides, the phenyl(ene) rings nearly lie in the plane defined by the oxadiazole unit. Thus, the whole molecule is generally rather close to planarity. Typical dihedral angles between the planes defined by the oxadiazole and phenyl(ene) rings are lower than 10°. This fact induces a partial conjugation of the electronic π-system along the whole molecule as is indicated by the shortness of the inter-ring bonds compared to theoretical values expected for a C(sp^2)-C(sp^2) single bond.

The systematic study, for the first time, of various 1,3,4-oxadiazole crystals (among others the six crystals which are the subject of the present document) allowed us to discover an arrangement pattern which is common to their majority: a particular type of π-complexes. In these special π-complexes the oxadiazole ring of one molecule is located between two phenyl(ene) rings of the adjacent molecules. In this way, the π-π interactions between the π-acceptor oxadiazole ring and the π-donor phenyl(ene) rings are optimized and the molecules pile in stacks. The stacks are held together through van der Waals forces and weak H-bonds, building thus the crystals. However, it should be pointed out that 6DPO6 I and 6DPO6 II show different molecular arrangements without such π-complexes.

It is noteworthy that two of the investigated compounds, DPO and 6DPO6, can crystallize in at least two different modifications. Of great interest is the surprising fact that DPO II—one of the polymorphs of DPO—has a non-centrosymmetric structure. Organic compounds usually pack in centrosymmetric arrangements. Due to its non-centrosymmetry DPO II is a potential material for non linear optical applications such as second harmonics generation. The case of 6DPO6 II is surprising as well. Here water molecules are incorporated in the crystal structure, which is found for the first time for an oxadiazole compound.

Once the *crystal structures* at ambient pressure were analyzed, we studied how they evolve *under compression*. To this end, powder X-ray diffraction experiments at high pressure were per-

formed. These experiments indicated that only one of the investigated crystals, 6DPO4, undergoes (two) pressure-induced phase transitions in the pressure ranges 0.9 to 1.7 GPa and 1.7 to 2.4 GPa. Drastic changes in its X-ray pattern led to this conclusion. Although DPO shows two polymorphs at ambient pressure and DPO I undergoes a temperature-induced phase transition into DPO II, neither DPO I nor DPO II perform phase transitions under compression. All investigated crystals showed a general shift of the X-ray patterns to larger 2θ values with pressure which results from the decrease of the lattice parameters.

The specific molecular arrangement of the crystals induces their strong anisotropic compression. For instance, there is little resistance to a lateral approach of the stacks while the compression of the stacks themselves (i.e. in the direction parallel to the stack axis) is inhibited. Especially stiff is the crystallographic axis a of the 6DPO6 II . In this crystal the molecules pack by forming rows along a. Adjacent molecules of a row are connected trough a water molecule by means of two H-bonds. Thus, it was concluded that the elastic potentials with sharper slopes at short intermolecular distances are those which describe strong H-bonds followed by those associated with π-π interactions along π-complexes. The potentials which describe weak H-bonds and van der Waals interactions may be rather shallow. Besides, from the analysis of the pressure dependence of the lattice parameters, hypotheses describing the compression mechanism of the crystals were proposed. The validity of such models should be tested in future studies either by single crystal high pressure investigations or/and by molecular modelling calculations.

The dependence of pressure upon the volume of the investigated crystals was well reproduced by Murnaghan's equation of state, which allowed the determination of a bulk modulus of compression. This parameter is an indicator for the stiffness of the material. The investigated crystals have small bulk moduli, usually around 7 GPa, and are therefore rather soft, like other organic compounds.

The *structural studies* under compression were complemented with similar investigations *under heating*. Preliminary TGA and DSC studies were performed to determine possible mass loss and phase transitions. Combining DSC analysis with Raman spectroscopy, it was found that DPO I undergoes an irreversible temperature-induced phase transition into DPO II. Another interesting result is that 6DPO6 II dehydrates into 6DPO6 I under heating. However, 6DPO4 which suffered two phase transitions under compression maintained the same structure under heating up to the melting point.

The previous results were confirmed by the X-ray diffraction experiments under heating. We have proposed that the phase transitions from DPO I to DPO II occur through an amorphous state. However, the mechanism of the 6DPO6 II dehydration into 6DPO6 I may imply the apparition of intermediate crystalline phases. In order to prove these hypotheses, single crystal X-ray analysis with a very precise temperature measurement and control is needed.

Additionally, the temperature dependence of the lattice parameters of the crystals could be determined. It turns out that the more compressible axes are those with the larger linear expansion coefficients. From the temperature dependence of the volume, the thermal expansion coefficients were found to take values of approximately $2 \cdot 10^{-4}$ K^{-1}. Thus, the isothermal MEOS could be completed with a factor which takes into account the temperature effect.

UV Vis spectroscopy

In view of potential applications of the 1,3,4-oxadiazoles in LEDs and scintillators, we studied the *absorption* and *emission* features of our compounds in solution as well as in crystalline state first at *ambient pressure* and then *under compression*.

The absorption spectra of both solutions and crystals are characterized by two bands in the UV range. The long-wave band, in the range 280 to 345 nm, corresponds to $\pi\pi^*$ transitions delocalized along the whole molecule and the short-wave band, between 230 and 303 nm, to nπ^* transitions localized at the hetero-atoms. When the substances are excited at the $\pi\pi^*$ band, they show an intense UV or blue fluorescence in the range 349 to 425 nm.

The absorption spectrum of the crystal is red shifted in relation to the solution spectrum and it is also broader. Similarly, the emission band of the crystal shows a red shift compared to the solution emission band. The red shift of the absorption spectrum is larger than that of the emission. These effects, red shift and broadening, are due to different factors. On the one hand, at the molecular level, the conjugation of the molecules which build the crystal is larger than that of the dissolved molecules. In solution the molecules are not planar, their rings can rotate freely around the molecular axis, thereby preventing the conjugation along the molecule. However, when the substance crystallizes, the molecules approach planarity which favours a partial conjugation along the whole molecule. The apparition of this partial conjugation induces the broadening of the ground and first excited electronic states and consequently a red shift of the absorption and emission spectra and the broadening of the absorption bands.

On the other hand, at the super-molecular level, the surrounding of a given molecule in solution is completely different to that in the crystals, influencing thus the electronic levels in a different way. In particular, the inter-molecular interactions within the crystals are considerably stronger than those in the solutions and may be the decisive cause for the observed red shifts.

The red shift effect becomes more pronounced when the crystal is compressed. We can follow the previous distinction between causes at the molecular and super-molecular levels to explain these shifts. The compression of the crystal may force the molecules to get closer to planarity, increasing thus their partial conjugation and inducing this way a further red shift. However, since at ambient pressure the crystals are already built by molecules very close to planarity this factor might not have an important effect. The decisive influence is at the super-molecular level. During the compression process the molecules approach each other, which implies an increase of the inter-molecular interactions. This induces the reduction of the electronic transition energy, i.e. a red shift of the spectrum.

Another effect which occurs when the crystals are compressed is the decay of their emission intensity. This is due to the combination of several processes. One is the increased radiation-less deactivation of the excited state which is favoured by the decrease of the transition energy. Two further causes involve the loss of energy in quenching sites. On the one hand, the number of defects in the crystal, which act as quenching sites, increases under compression. The increase of defects in the crystal structure could be confirmed by Raman investigations. On the other hand, the approach of the molecules enhances the mobility of the electrons and thus the probability that an electron finds a quenching site. From the previous effects, the red shift is fully reversible and the emission intensity decay is reversible to a great extent.

The combination of the emission investigations under compression with the high pressure structural studies allowed to relate the emission energy of DPO I to the inter-molecular spacing within the π-complexes. The emission energy decreases approximately by 1.2 eV when the inter-molecular distance is reduced by 0.1 nm. Such a relation may have interesting applications for the construction of super-molecular architectures (e.g. thin films) with the desired emission wavelength.

The continuous shift of the emission energy of 6DPO4 with pressure was interpreted as an indicator for the conservation of the stack-like arrangement during the phase transitions.

Raman spectroscopy

Finally, we have performed a *Raman spectroscopical* investigation at *ambient* and *high pressure*. The analysis of the ambient pressure spectra allowed the identification of the most intense internal modes with vibrations of the 1,3,4-oxadiazole and phenyl(ene) rings. In addition to the internal modes, the finger print region contains relatively sharp lattice modes at low frequencies. The study of the lattice modes under compression is a rapid and exact method to determine possible phase transitions. It was concluded—in agreement with the X-ray diffraction studies—that 6DPO4 is the only investigated crystal which undergoes pressure-induced phase transitions. The pressure

intervals where the two phase transitions of 6DPO4 occur were determined from the evolution of the Raman spectrum as: 0.1 to 1.0 GPa and 2.2 to 3.1 GPa.

Typically, the Raman lines move to higher frequencies with pressure. This effect is due to the anharmonicity of the vibrations. In addition to this shift, the general intensity of the spectra decreases under compression which is interpreted as an increment of the amorphous content in the sample. This effect is not fully reversible. Thus, a certain amorphous content is retained in the relaxed sample. Contrarily, the Raman lines return to their original position after the relaxation.

The inspection of the internal modes of 6DPO4 in the range of its first phase transition indicates a possible H-bond formation during the phase transition. These H-bonds should occur between molecules of adjacent stacks.

Combining the high pressure Raman investigations with the MEOS obtained from the X-ray studies under compression, we have calculated the mode Grüneisen parameter for the Raman modes. These parameters can be used to estimate the Debye-Grüneisen parameter. Thus, an important contribution to a complete equation of state of these crystals in the frame of the Debye model was made. The parameters of the cohesive potential as well as the wave velocity should be determined in the future.

Bibliography

[1] S. Schrader, M.B. Casu, Y. Kaminorz, O. Franco, B. Schulz, and G. Leising. In *45th SPIEs Annual Meeting*, San Diego, California, 2000. 1, 55

[2] S. Hoshino, K. Ebata, and K. Furukawa. *J. Appl. Phys.*, 87(4):1968–1973, 2000. 1

[3] G. Giro, M. Cocchi, J. Kalinkowski, P. Di Marco, and V. Fattori. *Chem. Phys. Lett.*, 318:137–141, 2000. 1

[4] R. Antony, B. Ratier, and A. Moliton. *Opt. Mater.*, 12:291–294, 1999. 1

[5] Z. Bao, J.A. Rogers, A. Dodabalapur, A.J. Lovinger, H.E. Katz, V.R. Raju, Z. Peng, and M.E. Galvin. *Opt. Mater.*, 12:177–182, 1999. 1

[6] J.P. Chen, D. Markiewicz, V.Y. Lee, G. Klaerner, R.D. Miller, and J.C. Scott. *Synth. Met.*, 107:203–207, 1999. 1

[7] J.F. Wang, G.E. Jabbour, E.A Mash, J. Anderson, Y. Zhang, P.L Lee, N.R Armstrong, N. Peyghambarian, and B. Kippelen. *Adv. Mater.*, 11(15):1266–1269, 1999. 1

[8] Z. Peng, Z. Bao, and M.E. Galvin. *Adv. Mater.*, 10:680–684, 1998. 1

[9] B. Schulz, Y. Kaminorz, and L. Brehmer. *Synth. Met.*, 84:449–450, 1997. 1, 55

[10] R.A. Anderson, K. Davidson, I. McInally, I. Soutar, D.J.S. Birch, and R.E. Imhof. *J. Photochem. and Photobiol. A: Chem.*, 45:123–133, 1988. 1

[11] J.B. Birks. *Photophysics of aromatic molecules*. John Wiley and Sons, New York, 1970. 1, 57, 58, 61, 62, 111

[12] H. Lami and G. Laustriat. *J. Chem. Phys.*, 48:1832–1840, 1968. 1

[13] D.L. Horrocks. *J. Chem. Phys.*, 50(11):4962–4966, 1969. 1, 55

[14] D.L. Horrocks. *J. Chem. Phys.*, 47:3089–3091, 1967. 1, 55

[15] W. Huang, H. Meng, W.L. Yu, J. Gao, and A.J. Heeger. *Adv. Mater.*, 10(8):593–596, 1998. 1, 55

[16] N. Tamoto, C. Adachi, and K. Nagai. *Chem. Mater.*, 9:1077ff, 1997. 1

[17] Q. Pei and Y. Yang. *Chem. Mater.*, 7:1568–1575, 1995. 1, 55

[18] Q. Pei and Y. Yang. *Adv. Mater.*, 7:559–561, 1995. 1, 55

[19] T. Tsutsui, E.I. Aminaka, and H. Tokuhisa. *Synth. Met.*, 85:1201ff, 1993. 1

[20] H. Tokuhisa, M. Era, and T. Tsutsui. *Synth. Met.*, 85:1161–1162, 1997. 1

[21] O. Franco, S. Katholy, K. Morawetz, J. Reiche, A. Freydank, L. Brehmer, and J.A. de Saja. *Colloids and Surfaces A: Physicochem. Eng. Aspects*, 198:119–126, 2002. 1

[22] J. Reiche, A. Freydank, A. Helms, T. Geue, B. Schulz, L. Brehmer, B. Stiller, and G. Knochenhauer. *Mater. Sci. Eng. C*, 8-9:237–242, 1999. 1

[23] S. Katholy. *Strukturaufklärung von Langmuir-Filmen mittels Reflexionsisothermen.* PhD thesis, Universität Potsdam, 1999. 1

[24] R. Giebler, B. Schulz, J. Reiche, M. Wühn, Ch. Wöll, A.P. Smith, S.G. Urquhart, H.W. Ade, and W.E.S. Unger. *Langmuir*, 15:1291–1298, 1999. 1

[25] Y. Kaminorz. *Charakterisierung und Optimierung von Leuchtdioden auf der Basis niedermolekularer und polymerer Heterozyklen.* PhD thesis, Universität Potsdam, 1998. 1, 55, 113

[26] A. Freydank. *Synthese neuer amphililer aromatischer 1,3,4-Oxadiazole und ihre Anwendung zum Aufbau supramolecularer Architekturen.* PhD thesis, Universität Potsdam, 1997. 1, 55, 113

[27] S. Janietz, A. Wendel, and R. Friedrich. *Synth. Met.*, 84:381–382, 1997. 1

[28] B. Schulz, M. Bruma, and L. Brehmer. *Adv. Mater.*, 9(8):601–613, 1997. 1

[29] H. Liszkiewicz, T. Glowiak, M.W. Kowalska, M. Rutkowska, A. Szeląg, J. Barczyńska, L. Kędzierska-Goździk, F. Blasczyk, and W. Dziewiszek. *Polish. J. Chem.*, 73:321–332, 1999. 1

[30] A.R. Katrizky. *Compr. Heterocyc. Chem.*, 6:426ff, 1984. 1

[31] B. Schulz, L. Brehmer, and G. Knochenhauer. *Mater. Sci. Eng. C*, C3:169–173, 1995. 1

[32] B. Schulz. *Mol. Crys. Liq. Crys.*, 240:135–141, 1994. 1

[33] B. Schulz and E. Leibnitz. *Acta Polymer.*, 43:343–347, 1992. 1

[34] J.B. Parise, D.J. Weidner, J. Chen, R.C. Liebermann, and G. Chen. *Ann. Rev. Sci.*, 28:349–374, 1998. 1

[35] R.J. Hemley and N.W. Ashcroft. *Phys. Today*, 51(8):26–32, 1998. 1

[36] J.V. Badding. *Ann. Rev. Mater. Sci.*, 28:631–658, 1998. 1

[37] J.V. Badding, L.J. Parker, and D.C. Nesting. *J. Solid State Chem.*, 117:229–235, 1995. 1

[38] H. Ito, Y. Tsutsumi, K. Minagawa, J. Takimoto, and K. Koyama. *Colloid. Polym. Sci.*, 273:811–815, 1995. 1

[39] F. Cansell, D. Fabre, J.P. Petitet, and A. Fontaine. *J. Phys. Chem.*, 99:13109–13114, 1995. 1, 75

[40] L.R. Benedetti, J.H. Nguyen, W.A. Caldwell, H. Liu, M. Kruger, and R. Jeanloz. *Science*, 286:100–102, October 1999. 1

[41] I. Nakabata, N. Matsui, Y. Akahama, and H. Kawamura. *Chem. Phys. Lett.*, 302:359–362, 1999. 1

[42] R. Stolle. *J. Prakt. Chem.*, II(68):137ff, 1903. 3

[43] R. Stolle. *J. Prakt. Chem.*, II(69):481ff, 1904. 3

[44] R. Stolle and L. Gutmann. *J. Prakt. Chem.*, II(69):509ff, 1904. 3

[45] O. Franco, G. Reck, I. Orgzall, and B. Schulz. *J. Phys. Chem. Solids*, 2002. in press. 3, 11, 118, 120, 122

[46] I. Orgzall, O. Franco, G. Reck, and B. Schulz. *J. Mol. Struct.*, 2002. submitted. 3, 11

[47] G. Reck, B. Schulz, I. Orgzall, and B. Schulz. CCDC 152152. Cambridge Crystallographic Data Center. 3, 11, 118, 120, 122

[48] G. Reck, B. Schulz, I. Orgzall, and B. Schulz. CCDC 160022. Cambridge Crystallographic Data Center. 3, 11, 118, 120, 122

[49] G. Reck. Personal communication. 3, 118, 120, 122

[50] S. Stockhause and B. Schulz. CCDC 151852. Cambridge Crystallographic Data Center. 3, 11, 118, 120, 122

[51] V.P. Kuznetsov, L.D. Patsenker, A.I. Lokshin, and A.V. Tolmachev. *Crystallog. Reports*, 43(3):430–438, 1998. 3, 11, 46, 118, 120, 122

[52] G. Sheldrick. University of Göttingen, Göttingen, 1997. 3

[53] O. Shimomura, S. Yamaoka, T. Yagi, M. Wakatsuki, K. Tsuji, H. Kawamura, N. Hamaya, O. Fukunaga, K. Aoki, and S. Akimoto. *Solid State Physics under Pressure*. Dordrecht: D. Reidel, 1985. 3

[54] J.E. Nickels, M.A. Fineman, and W.E. Wallace. *J. Phys. Chem.*, 53:625–628, 1949. 4

[55] D.L. Decker. *J. Appl. Phys.*, 42:3239ff, 1971. 5

[56] J.M. Brown. *J. Appl. Phys.*, 86(10):5801–5808, November 1999. 5, 23

[57] A. Jayaraman. *Rev. Modern Phys.*, 55(1):65–108, January 1983. 6

[58] G.J. Piermarini, S. Block, and J.S. Barnett. *J. Appl. Phys.*, 44:5377ff, 1973. 6

[59] R.A. Forman, G.J. Piermarini, J.S. Barnett, and S. Block. *Science*, 176:284ff, 1972. 6

[60] M. Chandrasekhar, S. Guha, and W. Graupner. *Adv. Mater.*, 13(8):613–918, 2001. 7, 62, 65, 69, 73, 75

[61] S. Stockhause, M.S. Wickleder, M. Meyer, I. Orgzall, and B. Schulz. *J. Mol. Structure*, 561:175–183, 2001. 11

[62] J. Mikat, O. Franco, W. Regenstein, G. Reck, G. Knochenhauer, B. Schulz, and I. Orgzall. *High Press. Res.*, 18:311–318, 2000. 11, 55, 65

[63] I. Orgzall, B. Lorenz, J. Mikat, G. Reck, G. Knochenhauer, and B. Schulz. *J. Phys. Chem. Solids*, 60:1949–1965, 1999. 11, 24, 30, 31, 76, 108, 119, 121

[64] G. Reck, B. Schulz, I. Orgzall, and B. Schulz. CCDC 152146. Cambridge Crystallographic Data Center. 11, 105, 119, 121, 123

[65] G. Reck, B. Schulz, I. Orgzall, and B. Schulz. CCDC 152147. Cambridge Crystallographic Data Center. 11, 105, 119, 121, 123

[66] G. Reck, B. Schulz, I. Orgzall, and B. Schulz. CCDC 152148. Cambridge Crystallographic Data Center. 11, 105, 119, 121, 123

[67] G. Reck, B. Schulz, I. Orgzall, and B. Schulz. CCDC 152149. Cambridge Crystallographic Data Center. 11, 105, 123

[68] G. Reck, B. Schulz, I. Orgzall, and B. Schulz. CCDC 152150. Cambridge Crystallographic Data Center. 11

[69] G. Reck, B. Schulz, I. Orgzall, and B. Schulz. CCDC 152151. Cambridge Crystallographic Data Center. 11

[70] B. Schulz, B. Stiller, T. Zetzsche, G. Knochenhauer, R. Dietel, and L. Brehmer. *Chem. Mater.*, 7:1041–1044, 1995. 11

[71] B. Schulz, B. Stiller, T. Zetzsche, G. Knochenhauer, R. Dietel, and L. Brehmer. *Mol. Cryst. Liq. Cryst.*, 248:35–42, 1994. 11

[72] R.W. Saalfrank, B. Weiss, K. Peters, and H.G. von Schnering. *Chem. Ber.*, 118:4026–4034, 1985. 11

[73] M.R. Caira. Crystalline polymorphism of organic compounds. In E. Weber, editor, *Design of organic solids*, volume 198 of *Topics in Current Chemistry*, pages 163–208. Springer, 1998. 12

[74] A. Nangia and G.R. Desiraju. Supramolecular synthons and pattern recognition. In E. Weber, editor, *Design of organic solids*, volume 198 of *Topics in Current Chemistry*, pages 57–96. Springer, 1998. 12, 21

[75] H.G.O. Becker. *Einführung in die Elektronentheorie organisch-chemischer Reaktionen*. VEB Deutscher Verlag der Wissenschaften, Berlin, third edition, 1974. 13

[76] J.P. Glusker, M. Lewis, and M. Rossi. *Crystal structure analysis for chemists and biologists*. VCH, 1994. 13, 14

[77] J.P. Glusker. Directional aspects of intermolecular interactions. In E. Weber, editor, *Design of organic solids*, volume 198 of *Topics in Current Chemistry*, pages 1–56. Springer, 1998. 14, 19

[78] R.E. Meléndez. Hydrogen-bonded ribbons, tapes and sheets as motifs for crystal engineering. In E. Weber, editor, *Design of organic solids*, volume 198 of *Topics in Current Chemistry*, pages 97–130. Springer, 1998. 15

[79] S. Stockhause. Personal communication. 17

[80] G.R. Desiraju. *Crystal engineering, the design of organic solids*. Elsevier, Amsterdam, 1989. 21

[81] G.R. Desiraju. *Angew. Chem.*, 107:2541–2558, 1995. 21

[82] J. Leliwa-Kopystiński and R. Teisseyre. *Constitution of the Earth's Interior*, volume 1 of *Physics and Evolution of the Earth's Interior 1*. Elsevier, 1984. 23

[83] J.P. Poirier. *Introduction to the Physics of the Earth's Interior*. Cambridge University Press, 1980. 23, 26, 87

[84] W.B. Holzapfel. *High Press. Res.*, 16(2):81–126, 1998. 23

[85] W.B. Holzapfel, M. Hartwing, and W. Sievers. *J. Phys. Chem. Ref. Data*, 30:515ff, 2001. 23

[86] M. Kumar. *Indian J. Pure Appl. Phys.*, 36:119–124, March 1998. 23

[87] S.W. Kieffer. *Rev. Geophys. Space Phys.*, 17(1):1–19, 1979. 23, 87

[88] A. Brillante, R.G. Della Valle, and K. Syassen. *J. Chem. Phys.*, 89:3163ff, 1988. 23, 25, 31

[89] A. Brillante, K. Reimann, and K. Syassen. *Chem. Phys. Lett.*, 151:243ff, 1988. 23, 25, 31

[90] A. Brillante, R.G. Della Valle, R. Farina, and E. Venuti. *Chem. Phys.*, 2191:177–184, 1995. 23, 25, 31, 75

[91] A. Brillante, R.G. Della Valle, C. Ulrich, and K. Syassen. *J. Chem. Phys.*, 107(12):4628–4634, 1997. 23, 25, 31, 75

[92] A. Brillante, R.G. Della Valle, C. Polizzi, and K. Syassen. *Physica B*, 265:199–202, 1999. 23, 25, 31, 75

[93] A. Brillante, R.G. Della Valle, and E. Venuti. *Chem. Phys. Lett.*, 246:619–625, 1995. 23, 75

[94] R.G. Della Valle, D. Gazzillo, R. Frattini, and G. Pastore. *Phys. Rev. B*, 49(18):625–632, 1994. 23

[95] R.G. Della Valle and E. Venuti. *Phys. Rev. B*, 54(6):3809–3816, 1996. 23

[96] R.G. Della Valle and E. Venuti. *Phys. Rev. B*, 58(1):206–212, 1998. 23

[97] R.G. Della Valle, E. Venuti, and A. Brillante. *Chem. Phys.*, 198:79–89, 1995. 23, 75

[98] R.G. Della Valle, E. Venuti, and A. Brillante. *Chem. Phys.*, 202:231–241, 1996. 23, 75

[99] M. Bernasconi, M. Benoit, M. Parinello, G.L. Chiarotti, P. Focher, and E. Tosatti. *Physica Scripta*, 66:falta, 1996. 23

[100] B. Holm, R. Ahuja, A. Belonoshko, and B. Johansson. *Phys. Rev. Lett.*, 85(6):1258–1261, August 2000. 23

[101] M.S. Miao, V.E. Van Doren, R. Keuleers, H.O. Desseyn, C. Van Alsenoy, and J.L. Martins. *Chem. Phys. Lett.*, 316:297–302, January 2000. 23

[102] J.W. Schroer and P.A. Monson. *J. Chem. Phys.*, 112(20):8950–8957, May 2000. 23

[103] R.J. Roberts, R.S. Payne, and R.C. Rowe. *Eur. J. Pharm. Sci.*, 9(3):277ff, 2000. 23

[104] K. Ghandehari, J. Akella, S.T. Weir, and C.A. Ruddle. *J. Phys. Chem. Solids*, 61:1883–1887, 2000. 23

[105] K. Knorr, C.M. Braunbarth, G. van de Goor, P. Behrens, C. Griewatsch, and W. Depmeier. *Solid State Comm.*, 113:503–507, 2000. 23

[106] J.L. Burris, L. Tereshchenko, P. Kabos, H.D. Hochheimer, Y. Luspin, C.R. Evenson, and P.K. Dorhout. *J. Phys. Chem. Solids*, 61:719–726, 2000. 23

[107] A. Lucas, M. Mouallem-Bahout, C. Carel, J. Gaudé, and M. Matecki. *J. Solid State Chem.*, 146:73–78, 1999. 23

[108] R.K. Pandey. *J. Phys. Chem. Solids*, 59(6-7):993–996, 1998. 23

[109] E. Grechnev, H.W. Hugosson, R. Ahuja, and O. Eriksson. *High Press. Phys. Technol.*, 10:100ff, 2000. 23

[110] P. Söderlind and O. Eriksson. *Phys. Rev. B*, 60:9372ff, 1999. 23

[111] R. Ahuja, O. Eriksson, and B. Johansson. *Phys. Rev. B*, 60:14475ff, 1999. 23

[112] R. Ahuja, O. Eriksson, and B. Johansson. *Physica B*, 265:87ff, 1999. 23

[113] R. Ahuja, B. Johansson, J.M. Wills, and O. Eriksson. Structural phase transformations in alkaline-earth oxides and chalcogenides at high pressure: theory. In S.K. Sikka, S.C. Gupta, and B.K. Godwal, editors, *Advances in High Pressure Research in Condensed Matter*, page 250ff. National Institute of Science Communication, New Delhi, 1997. 23

[114] Molecular Simulations Inc., Burlington MA. 1994. Cerius2 Handbook. 24

[115] P. Puschnig, C. Ambrosch-Draxl, G. Heimel, E. Zojer, R. Resel, G. Leising, M. Kriechbaum, and W. Graupner. *Synt. Met.*, 116:327–331, 2001. 24, 31, 43, 61, 65, 69, 73

[116] P. Blaha, K. Schwarz, and J. Luitz. Technische Universität Wien, Wien, 1999. 24, 65

[117] G.P. Charbonneau and Y. Delugeard. *Acta Cryst. C*, 33:1586ff, 1977. 25

[118] G. Heimel, P. Puschnig, Q. Cai, C. Martin, E. Zojer, W. Graupner, M. Chandrasekhar, H.R. Chandrasekhar, C. Ambrosch-Draxl, and G. Leising. *Synt. Met.*, 116:163–166, 2001. 25, 65, 75

[119] G. Heimel, Q. Cai, C. Martin P. Puschnig, S. Guha, W. Graupner, C. Ambrosch-Draxl, and G. Leising. *Synt. Met.*, 119:371–372, 2001. 25, 65, 75

[120] P. Puschnig and C. Ambrosch-Draxl. *Phys. Rev. B*, 60(11):7891–7898, 1999. 25, 61

[121] S. Guha, W. Graupner, R. Resel, M. Chandrasekhar, H.R. Chandrasekhar, R. Glaser, and G. Leising. *Phys. Rev. Lett.*, 82(18):3625–3628, May 1999. 25, 75

[122] R.J. Angel. Equations of state. In R.M. Hazen, editor, *Comparative Crystal Chemistry*, volume 39 of *Reviews in Mineralogy*. MSA, 2001. 27

[123] W. Kraus and G. Nolze. BAM, Berlin, 1999. 30, 45

[124] J. Shen, J.B. Parise, R. Li, D.J. Weidner, and M. Vaughan. *Properties of Earth and Planetary Materials at High Pressure and Temperature*, volume 101 of *Geophysical Monograph Series*. American Geophysical Union, Washington D.C., 1998. 31

[125] G. Beggerow. Eigenschaften der Materie bei hohen Drücken. In *Zahlenwerte und Funktionen aus Naturwissenschaften und Technik. Gruppe IV: Makroskopische und Technische Eigenschaften der Materie.*, Landolt-Börnstein. Neue Serie. Springer, 1980. 41, 50, 113

[126] H. Yamawaki, M. Sakashita, K. Aoki, and K. Takemura. *Phys. Rev. B*, 53(17):403–407, 1996. 42

[127] I.B. Berlman. *Handbook of Fluorescence Spectroscopy of Organic Molecules*. Academy Press, second edition, 1971. 55

[128] J.R. Lakowicz, I. Gryczynski, H. Malak, and Z. Gryczynski. *J. Phys. Chem.*, 100:19406–19411, 1996. 55, 57, 58

[129] N.A. Popova, E.G. Yushko, B.M. Krasovitskii, V.I. Minkin, A.E. Lyubarskaya, and M.L. Goldberg. *Khim. Geterotsiklich. Soed.*, 1:26–32, 1983. 55, 56, 112, 129

[130] R.E. Trifonov, N.I. Rtishchev, and V.A. Ostrovskii. *Spectrochim. Acta*, 52:1875–1882, 1996. 55

[131] X.C. Li, A.B. Holmes, A. Kraft, S.C. Moratti, G.C.W. Spencer, F. Cacialli, J. Gruener, and R.H. Friend. *J. Chem. Soc. Chem. Commun.*, 21:2211–2212, 1995. 55

[132] E. Buchwald, M. Meier, S. Karg, P. Pösch, H.W. Schmidt, P. Strohriegl, W. Riess, and M. Schwoerer. *Adv. Mater.*, 7(10):839–842, 1995. 55

[133] M. Berggren, G. Gustafsson, O. Inganäs, M.R. Andersson, T. Hjertberg, and O. Wennerström. *J. Appl. Phys.*, 76(11):7530–7534, 1994. 55

[134] S. Lunak, M. Nepras, A. Kufuerst, and J. Kuthan. *J. Chem. Phys.*, 170:67–76, 1993. 55, 56, 112, 130

[135] P. Lhoták, A. Kufuerst, and P. Nádeník. *Collect. Cech. Chem. Commun.*, 57:385–392, 1992. 55

[136] O. Franco, W. Regenstein, I. Orgzall, and B. Schulz. *High Press. Res.*, 22:131–134, 2002. 55, 65

[137] V.F. Pedash and Y.F. Pedash. *Zh. Prikladnoi Spekt.*, 46(4):624–628, 1987. 56

[138] B.M. Krasovitskii, L.D. Pchelinova, L.Sh. Afanasiadi, A.E. Shevchenko, and L.A. Kutulya. *Bull. Acad. Sci. USSR, Phys. Series*, 42(3):640–644, 1978. 56

[139] V.V. Gruzinskii, M.A. Senyuk, O.L.Ñeyra Bueno, and L.S. Afanasiadi. *J. Appl. Spectroscopy*, 57:593–596, 1992. 56

[140] V.M. Feygelman, J.K. Walker, A.R. Katrizky, and Z. Dega-Szafran. *Chem. Scripta*, 29:241–243, 1989. 56, 58

[141] H. Gebert. Personal communication. 57, 58

[142] A.V. Kirichenko, A.O. Doroshenko, and V.M. Shershukov. *Chem. Phys. Reports*, 17(9):1643–1651, 1998. 58

[143] A.O. Doroshenko, A.V. Kirichenko, V.G. Mitina, and O.L. Ponomaryov. *J. Photochem. Photobiol. A: Chemistry*, 94:15–26, 1996. 58

[144] J.R. Lakowicz. *Principles of Fluorescence Spectroscopy*. Kluwer Academic / Plenum Publishers, New York, second edition, 1999. 59, 111, 113

[145] S.C. Yang, W. Graupner, S. Guha, P. Puschnig, C. Martin, H.R. Chandrasekhar, M. Chandrasekhar, G. Leising, C. Ambrosch-Draxl, and U. Scherf. *Phys. Rev. Lett.*, 85(11):2388–2391, 2000. 61, 65, 69, 73, 75

[146] Z.A. Dreger, J.O. White, and H.G. Drickamer. *Chem. Phys. Lett.*, 290:399–404, 1998. 66, 69

[147] Z.A. Dreger, G. Yang, J.O. White, Y. Li, and H.G. Drickamer. *J. Phys. Chem. B*, 102:4380–4385, 1998. 66, 69

[148] H.G. Drickamer, Z.A. Dreger, J.M. Lang, and G. Yang. *Pol. J. Chem.*, 71:1647–1660, 1997. 66, 69

[149] Z.A. Dreger and H.G. Drickamer. *J. Phys. Chem. A.*, 101:1422–1428, 1997. 66, 69

[150] Z.A. Dreger and H.G. Drickamer. *J. Phys. Chem. A.*, 101:1429–1440, 1997. 66, 69

[151] Z.A. Dreger, J.M. Lang, and H.G. Drickamer. *J. Phys. Chem. A.*, 100:4637–4645, 1996. 66, 69

[152] Z.A. Dreger, J.M. Lang, and H.G. Drickamer. *J. Phys. Chem. A.*, 100:4646–4653, 1996. 66, 69

[153] H.G. Drickamer. High pressure luminescence spectroscopy in polymers. In J.F. Rabek, editor, *Photochemistry and Photophysics*, volume I, pages 137–175. CRC Press, 1990. 66, 69

[154] H.G. Drickamer. *Ann. Rev. Phys. Chem*, 33:25–47, 1982. 66, 69

[155] H.G. Drickamer. *Science*, 156(3779):1183–1189, 1967. 66, 69

[156] H.G. Drickamer and C.W. Frank. *Electronic transitions and the high pressure chemistry and physics of solids*. Fletcher & Son Ltd, 1973. 66

[157] S. Webster and D.N. Batchelder. *Polymer*, 37(22):4961–4968, 1996. 66, 69, 72, 75

[158] B. Lorenz, I. Orgzall, P.K. Dorhout, C.C. Raymond, K. Weishaupt, R. D'Adamo, and H.D. Hochheimer. *Phys. Rev. B*, 22:2800ff, 1997. 68

[159] D.O. Hummel and F. Scholl. *Altas der Polymer- und Kunststoffanalyse*, volume 2b/I. Carl Hanser, München, second edition, 1988. 75

[160] D. Lin-Vien, N.B. Colthup, W.G. Fateley, and J.G. Grasselli. *The handbook of infrared and Raman characteristic frequencies of organic molecules.* Academic Press, New York, 1991. 75, 80, 82

[161] D.H. Christensen, J.T. Nielsen, and O.F. Nielsen. *J. Mol. Spectrosc.*, 24:225–234, 1967. 75, 80

[162] D.H. Christensen, J.T. Nielsen, and O.F. Nielsen. *J. Mol. Spectrosc.*, 25:197–204, 1968. 75, 80

[163] J.W. Anthonssen, D.H. Christensen, J.T. Nielsen, and O.F. Nielsen. *Spectrochim. Acta*, 32A:971–982, 1976. 75

[164] A. El-Azhary. *Spectrochim. Acta Part A*, 52A:33–44, 1996. 75, 76

[165] A. El-Azhary. *Spectrochim. Acta*, 51A:995–1003, 1995. 75, 76

[166] M. Milone and G. Müller. *Gazz. Chim. Ital.*, 63:334ff, 1933. 75, 77, 80

[167] M. Milone and G. Müller. *Gazz. Chim. Ital.*, 63:456ff, 1933. 75, 77, 80

[168] M. Milone and G. Müller. *Gazz. Chim. Ital.*, 65:241ff, 1935. 75, 77, 80

[169] M. Milone and E. Borello. *Gazz. Chim. Ital.*, 81:368ff, 1951. 75, 77, 80

[170] M. Milone and E. Borello. *Gazz. Chim. Ital.*, 81:677ff, 1951. 75, 77, 80

[171] S. Webster and D.N. Batchelder. *Macromol. Symp.*, 87:177ff, 1994. 75, 83

[172] F. Cansell, J.P. Petitet, and D. Fabre. *Polym. Commun.*, 30:234–236, August 1989. 75

[173] J.R. Ferraro. *Vibrational spectroscopy at high external pressures.* Academic Press, Orlando, 1984. 75, 76, 83

[174] S. Guha, W. Graupner, R. Resel, M. Chandrasekhar, H.R. Chandrasekhar, R. Glaser, and G. Leising. *Synth. Met.*, 101:180–181, 1999. 75

[175] I. Orgzall, J. Mikat, B. Lorenz, R. Dietel, G. Knochenhauer, and B. Schulz. *Polymer*, 38(7):1537–1543, 1997. 76

[176] D. Hofmann, E. Leibnitz, R. Schmolke, and B. Schulz. *Angew. Makromol. Chem.*, 204:111–118, 1993. 76

[177] S.W. Kieffer. *Rev. Geophys. Space Phys.*, 17(1):20–34, 1979. 87

[178] S.W. Kieffer. *Rev. Geophys. Space Phys.*, 17(1):35–59, 1979. 87

[179] S.W. Kieffer. *Rev. Geophys. Space Phys.*, 17(1):862–886, 1979. 87

[180] G. Reck. Personal communication. 105, 119, 121, 123

[181] A. Kawski. *Acta Phys. Polon.*, 29(4):507–518, 1966. 113

[182] P.W. Atkins. *Physikalische Chemie.* VCH, Weinheim, 1996. 113

[183] M. Grobys and K.A. Zachariasse. *J. Inf. Recording.*, 24:405–413, 1998. 115

Appendix A

Crystal structure of similar compounds at normal conditions

For the purpose of comparison, we briefly describe the crystal structures of some oxadiazole compounds similar to those featured in the present study [64, 65, 66, 67, 180]. All of them are symmetrically substituted DPO derivatives: in 3DPO3 both substituents are CH_3, in 5DPO5 $COOCH_3$, in 1DPO1 NO_2, and in 7DPO7 $N(CH_3)_2$ (see fig. 1 for a schema of their chemical structure).

The data concerning the molecular conformation, the crystallographic data, and inter-molecular interactions of the following structures are summarized in the tables C.4, C.2 and C.6. Most of the compounds described here—3DPO3, 5DPO5 I, 5DPO5 II, and 1DPO1—build long needles with dimensions of the order of some millimeters in the longest direction and tens of micrometer in the other two. Only 7DPO7 crystallizes in prismatic form with lengths of several hundreds of micrometers. All these crystals are colourless, except 1DPO1 which is light yellow.

A.1 Molecular conformation

The molecules which form the crystals are quite planar (except 7DPO7 as commented below). The oxadiazole unit is perfectly planar and the phenylene rings are nearly planar. The phenylene rings are slightly inclined to the oxadiazole unit (less than 10°). This small deviation from planarity does not hinder the conjugation of the π system along the molecule as indicates the shortness of the inter-ring bonds (cf. table C.4 for details about the molecular conformations).

The 7DPO7 molecule adopts a rather non planar conformation in the crystal. Though the three rings are nearly planar, the phenylene rings are twisted with respect to the oxadiazole ring (7° and 18°, table C.4). The bond that the oxadiazole unit forms with the most twisted phenylene ring is longer than the other inter-ring bond due to the slight decrease of the conjugation (cf. table C.4).

A.2 Molecular arrangement

A.2.1 3DPO3

The molecular packing of 3DPO3 in the crystal is very similar to that of 6DPO4 (§3.4.5). Stacks of molecules pile along c (fig. A.1). Within a stack, the molecules are connected by π-π interactions which leads to the building of π-*complexes*, such as those reported for similar oxadiazole compounds in §3.4 (fig. 3.2). The inter-planar spacing in the π-complex amounts to 0.371 nm. All molecules of a stack are arranged parallel to each other but show alternating orientation regarding the

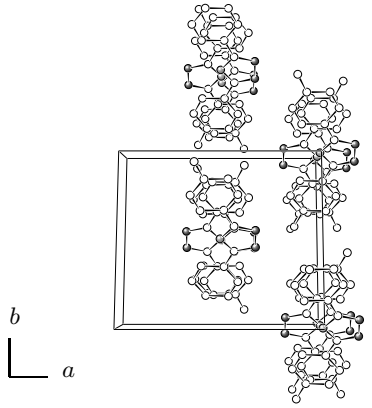

(a) Top view of the stacks.

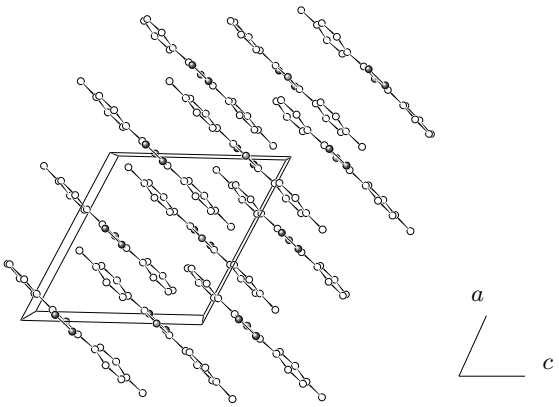

(b) Lateral view of the stacks. Adjacent stacks in the figure lie in different depths.

Fig. A.1: Molecular arrangement of 3DPO3.

oxadiazole unit (fig. A.1(a)). The molecular planes form an angle of approximately 43° with the stack axis.

The stacks are parallel to each other. The forces between stacks are weak *van der Waals* interactions. *Adjacent* stacks *along a* are principally connected through the N atom of the oxadiazole ring and the phenylene ring. *Contiguous* stacks *regarding the b-direction* interact mostly through the CH_3 groups (cf. table C.6 for details about inter-atomic distances).

A.2.2 5DPO5 I

The crystal structure of 5DPO5 I shows the herring bone packing found in other oxadiazole compounds (fig. A.2). The stack axis is *a* and the molecular planes are tilted by ±45° w.r.t. it. Within the stack, the molecules arrange in a sandwich motif with *π-complexes* of the type represented in fig. 3.2. The inter-planar spacing between the molecules of a stack is 0.333 nm.

Neighbouring stacks *regarding to c* are connected by *weak H-bonds* between the $COOCH_3$ groups. A $COOCH_3$ group has one H-bond acceptor (the O bonded to C by a double bond) and one H-bond donor (the CH_3 group). In 5DPO5 I, every H-bond acceptor of the $COOCH_3$ groups is bonded to two CH_3 groups (H-bond donors) of two molecules of the adjacent stack. Consequently, also every H-bond donor of a molecule is connected to two H-bond acceptors of two neighbouring molecules. The two bonds that every H-bond acceptor (and every H-bond donor, respectively) builds differ slightly (cf. table C.6). Thus, a $COOCH_3$ group builds four weak H-bonds with two molecules of two adjacent stacks. Similar *weak H-bonds* serve as connection between *adjacent* stacks *along b*. Now they occur between an N atom of the oxadiazole ring and a CH group of the phenylene ring (cf. table C.6).

A.2.3 5DPO5 II

The second crystal structure of 5DPO5 is shown in fig. A.3. The molecules arrange in layers parallel to the *bc*-plane. Within a layer, two orientations of the molecular planes are found, with a relative inclination of 26°. This forms a zig-zag arrangement (fig. A.3(b)). The minimum distance inside a layer occurs between the N and O atoms of the oxadiazole rings of molecules with different orientation (cf. table C.6). This spacing and the relative orientation of the molecules indicate the

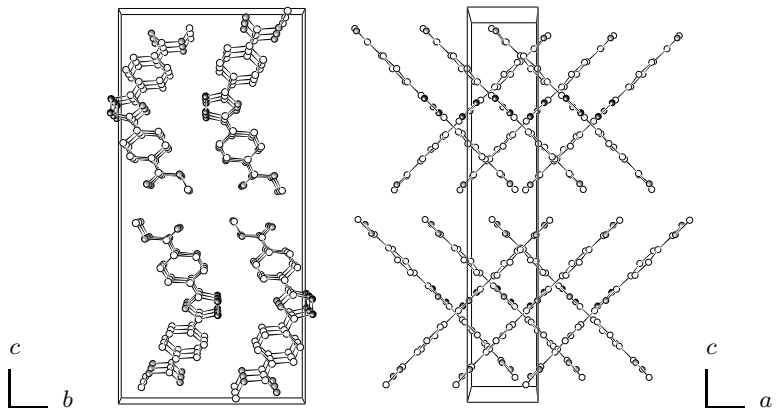

(a) Top view of the stacks. (b) Lateral view of the stacks.

Fig. A.2: Molecular arrangement of 5DPO5 I.

existence of strong *van der Waals* interactions. Besides, a net of *weak H-bonds* holds the layer together. The $COOCH_3$ groups of a molecule build two H-bonds with molecules of their same layer. Depending on whether the molecules are parallel or tilted in relation to each other, the H-bonds are slightly different (cf. table C.6). Consequently, every $COOCH_3$ group builds four weak H-bonds, two with a molecule of a different layer and two with two different molecules of the same layer.

The layers interact through *weak H-bonds* between the $COOCH_3$ groups. Every $COOCH_3$ group participates in two H-bonds with one molecule of the contiguous layer. The H-bond acceptors of the two molecules (the O atom bonded to C by a double bond) are bonded to the H-bond donors (the CH_3 groups) (cf. table C.6).

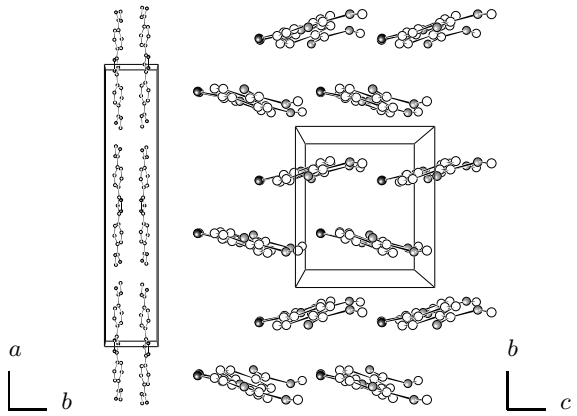

(a) Unit cell (b) Lateral view of a layer

Fig. A.3: Molecular arrangement of 5DPO5 II.

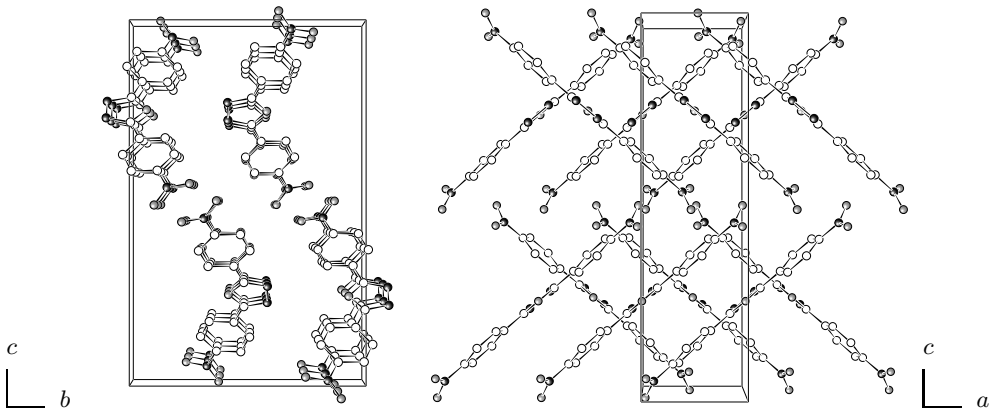

(a) Top view of the stacks.

(b) Lateral view of the stacks.

Fig. A.4: Molecular arrangement of 1DPO1.

A.2.4 1DPO1

The crystal packing of 1DPO1 is also a herring bone arrangement (fig. A.4). The stack axis is *a*. The molecules of a stack are arranged parallel to each other and oriented in the same direction. The molecular plane is tilted by $\pm 40°$ to the stack axis. Like in crystals of similar compounds, the molecules of a stack are displaced in such a way that they form *π-complexes* (fig. 3.2). The distance between the molecular planes amounts to 0.353 nm.

There are several interactions between stacks. Firstly, stacks which appear to be *adjacent along c* are connected by strong *van der Waals* interactions between the O atoms of the NO_2 groups of neighbouring molecules (cf. table C.6). Besides these van der Waals forces, the stacks are connected through *weak H-bonds*. There are two different weak H-bonds in 1DPO1 between stacks *adjacent along b*. Those between the CH groups of the phenylene rings and the O atoms of the NO_2 groups (cf. table C.6). Every molecule is linked by two of these H-bonds with one of its neighbours. The other kind of H-bonds appears between one of the CH groups of the phenyl rings and one N atom of the oxadiazole ring (cf. table C.6).

As we comment in §4.2, Orgzall et al. showed that 1DPO1 undergoes several phase transitions under compression [63]. Moreover, with the help of molecular modelling simulations, they were able to assign appropriate crystal structures to the high pressure phases.

A.2.5 7DPO7

The three-dimensional packing of 7DPO7 is very complex (fig. A.5). It consists of an intertwine of all the molecules, where no special motif appears. This results from the fact, that the interactions between a given molecule and *all* its neighbours are similar. A molecule interacts with the adjacent molecules by *van der Waals* interactions and by *weak H-bonds*. The shortest distance between molecules occurs between a C atom of one phenylene ring and an N atom of one $N(CH_3)_2$ group and is associated with a *van der Waals* interaction (not with a *weak H-bond* because the H atom bonded to the C atom lies too far away from N). There are also *weak H-bonds* between the same group of atoms of different molecules (cf. table C.6).

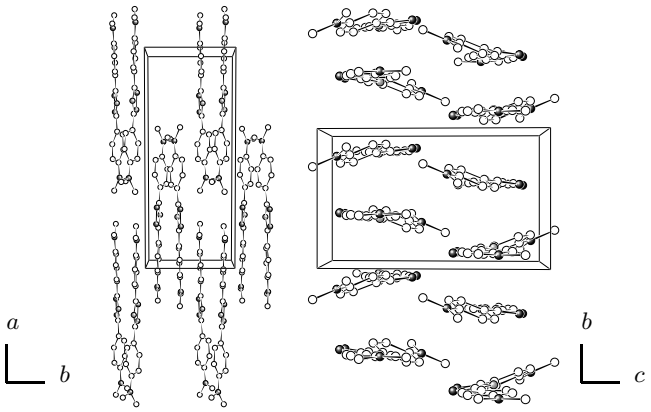

(a) View of the unit cell. (b) View of the zig-zag structure.

Fig. A.5: Molecular arrangement of 7DPO7.

Appendix B

Influence of the substituents of DPO derivatives on their electronic transitions

B.1 Introduction

Usually, the study of the optical properties of a substance, strictly spoken, of a family of substances, is carried out in solution. In this case, changes at the *molecular* level are normally created by the addition of substituents to the basic molecular unit. This may lead to changes in the electronic structure of the molecule, e.g. to a charge transfer along the molecule. Another way to influence the electronic structure is the alteration of the molecular conformation. For instance, placing substituents in different positions of the aromatic rings, a modification of the molecular geometry can also be attained. When dealing with solutions, the influences at the *super-molecular* level are those originated by the inter-molecular interactions solute-solvent and solute-solute. The first of these interactions may be parameterized by the dielectric constant of the solvent (solvatochromic effect), and the second one by the concentration of the solution [11, 144]. Of course, the modification of the electron distribution of the molecule by the addition of substituents or by the modification of the molecular conformation (molecular level) also influences the interactions of the molecule with its environment (super-molecular level).

In this appendix we first show a study of the modification of the electronic transitions of DPO derivatives caused by the introduction of substituents (molecular level), and then present some preliminary results which indicate the convenience of using high pressure to modify the dielectric constant of the solvent and therefore the interactions solute-solvent (super-molecular level).

B.2 Influence of the substituents of DPO derivatives on their electronic transitions

In §6.3 the long-wave band is identified with a $\pi\pi^*$ transition delocalized along the entire molecule and the short-wave band with an $n\pi^*$ transition localized at the hetero-atoms of the oxadiazole ring and of the possible substituents. Such an assignment results from the comparison among several oxadiazole compounds in solution and with literature data (cf. §6.2). We investigated two families of para-substituted DPO derivatives: one with NO_2, a strong electron acceptor, as fixed substituent (1DPO family); and another with NH_2, an electron donor, as fixed substituent (6DPO family). The results are summarized in table B.1.

	R_1	R_2	$\lambda^{abs}_{n\pi^*}$ (nm)	$\lambda^{abs}_{\pi\pi^*}$ (nm)	$\lambda^{lum}_{\pi\pi^*}$ (nm)
DPO	H	H	230	280	349
1DPO	NO_2	H	246	308	–
1DPO3	NO_2	CH_3	252	313	–
1DPO4	NO_2	OCH_3	–	337*	–
1DPO6	NO_2	NH_2	297	357	–
1DPO7	NO_2	$N(CH_3)_2$	311	383	–
1DPO1	NO_2	NO_2	217	313	–
6DPO3	NH_2	CH_3	–	324	437
6DPO4	NH_2	OCH_3	264	324	425
6DPO6	NH_2	NH_2	285	336	405
6DPO7	NH_2	$N(CH_3)_2$	295	347	405
6DPO1	NH_2	NO_2	297	357	–

Tab. B.1: Absorption and emission maxima of DPO derivatives in ethanol solution. R_1 and R_2 correspond to fig. 1. The compounds which contain the NO_2 group show no fluorescence. *From [129] in toluene.

The substitution of DPO with NO_2, leading to 1DPO induces a red shift of the absorption spectrum, particularly large for the long-wave band. The red shift increases when a second substituent is added and its magnitude is directly related to the donor character. When the electronic nature of the substituents is very different (1DPO6 and 1DPO7), the shift is very large. It results from the charge transfer which occurs along the molecule, inducing an important increase in the conjugation of the π system [134].

The variation of the second substituent in the 1DPO family influences as well the relative intensity of the bands. When it is an electron acceptor (1DPO1) or just an H atom (1DPO), the long-wave band is much more intense than the short-wave band. The addition of a weak electron donor (1DPO3), still preserves this relation between the two bands, but not somewhat weakened. By increasing the donor nature of the second substituent (1DPO6), an inversion in the intensity relation occurs. From this behaviour, the $n\pi^*$ character of the short-wave band can be deduced as follows. Transitions of $n\pi^*$ type are localized at the hetero-atoms, therefore an increase in the electron density around these atoms enhances the transition probability. In the previous compounds, the oxadiazole ring and the NO_2 group are possible centers for this kind of transition. The strong electron acceptor group NO_2 may enhance its electron density at expense of the donor groups placed at the other end of the molecule. The larger the donor nature of the second substituent is, the larger the electron density around NO_2 will be and therefore the larger the probability of an $n\pi^*$ transition localized at this group. Thus, the progressive increment of the intensity of the short-wave band with increase of the donor characteristics of the second substituent suggests the identification of this band with an $n\pi^*$ transition. Although the oxadiazole moiety may be as well center for $n\pi^*$ transitions, its contribution to the short-wave band is very small as is indicated by the absorption spectrum of DPO (fig. 6.2).

The introduction of a donor substituent (like NH_2 in the family 6DPO) influences in a similar way the absorption properties. The systematic variation of the second substituent in the family 6DPO shows also an increase in the red shift value with increment of the donor properties of the substituents. In comparison with the shifts observed for the 1DPO derivatives, the 6DPO derivatives show slightly larger shifts, expected in the case of having a strong donor as second substituent.

The addition of substituents contributing to increase the conjugation of the π system is expected to induce a red shift of the $\pi\pi^*$ band. Since in all cases, the long-wave band suffers a more intense red shift than the short-wave band, it is associated with a $\pi\pi^*$ transition.

The fluorescence of the 6DPO derivatives shows an opposite response to the addition of substituents. Now an increment in the donor character of the second substituent involves a blue shift

of the spectrum. The addition of donor substituents increments the conjugation along the molecule and therefore the planarity of the molecule in S_0. Thus, the observed blue shift corresponds with the decrease of relaxation in S_1 and the consequent diminishing of the Stokes shift.

B.3 Absorption and fluorescence of solutions under compression

The optical properties of a substance are dramatically influenced by its surroundings. In § 6.4 and § 7.3 it is shown how modifications of the inter-molecular interactions affect the absorption and fluorescence characteristics of the material. When dealing with solutions, inter-molecular interactions between solute and solvent can be varied by changes in the dielectric constant of the solvent. It is well known, that increases in the solvent permeability, i.e. in its dielectric constant imply red shifts in the absorption and emission spectra of the solutions [144]. This effect (solvatochromy) is due to the enhanced delocalization of the outer shell electrons in a polar medium. From the study of the red shift upon the polarizability of the medium, the permanent dipole moment of the excited state can be calculated, if that of the ground state is known [181]. Additionally, the second hyper-polarizability can be derived from the study of the solvatochromic effect, which is of great interest for possible applications in non-linear optic [144].

The standard method for the study of the solvatochromy is the use of solvents with different dielectric constants. This procedure shows an important disadvantage: by changing the solvent, not only the dielectric constant of the medium varies but also its chemical characteristics. Different solvents have different chemical structure which influences the inter-molecular interactions solute-solvent. To solve this problem we propose an alternative technique: the compression of solutions. The permeability of a solvent can be increased in a controlled way by the application of high pressure. In this way only the permeability of the solvent is varied without the introduction of new chemical parameters into the system.

To show the advantages of this method, we chose 6DPO7 (the DPO derivative with R_1=NH_2, R_2=$N(CH_3)_2$) because of its intense photo- and electro-luminescence which makes it interesting for technological applications as LED material [25] and because it constitutes the basic unit for many amphiphilic compounds used to build Langmuir-Blodgett films [26]. We investigated a concentrated solution of 6DPO7 in ethanol (c=10^{-2} mol/l). Such a high concentration is required due to the small thickness of the sample chamber (approximately 70 μm) in order to achieve good signals. Absorption and emission spectra were taken at different pressures up to 3.3 GPa (see fig. B.1 and B.2). Further compression of the solution leads to the solidification of the solvent. The absorption spectrum shifts to lower energies with increasing pressure. The shape of the bands remains unaltered while its intensity increases. In the emission spectra a red shift together with a large decrease of the intensity occurs.

Experimental data of the relative dielectric constant (ε) of ethanol under compression [125] were satisfactorily adjusted to a parabola, allowing the determination of the relative dielectric constant in the whole pressure range. Up to 3.3 GPa, the relative dielectric constant of ethanol varies from 27 to 42, covering a broad field. From the Clausius-Mosotti equation, the polarizability of the solvent is proportional to $(\varepsilon - 1)/(\varepsilon + 2)$ [182]. In this way, changes of the polarizability of the solvent with pressure can be quantified. Figures B.3 and B.4 represent the red shift of the two absorption bands and of the fluorescence band as a function of pressure and of $(\varepsilon - 1)/(\varepsilon + 2)$, respectively. In this second case the typical linear relation for the solvatochromic effect is found [144, 181]. The experimental values are reported in table G.6.

It is not the aim of this section to describe the complex solvatochromic effect. We just want to show that the application of pressure is an advantageous method to modify strongly and in a controlled way the permeability of the solvent. Although the compression of the solvent influences as well its viscosity, this factor may have a negligible influence in systems like ours where there

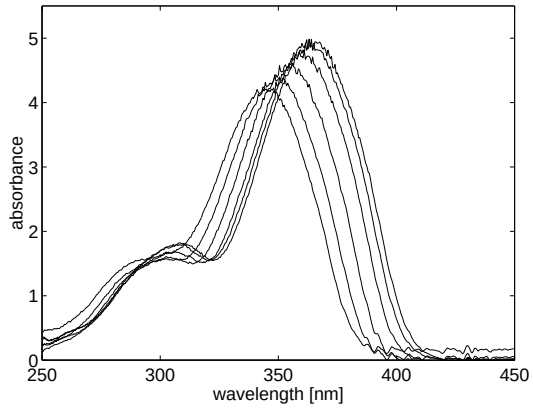

Fig. B.1: Absorption spectra of 7DPO6 in ethanol solution at different pressures, from left to right: 0.2, 0.5, 1.2, 1.9, 2.6, and 3.3 GPa.

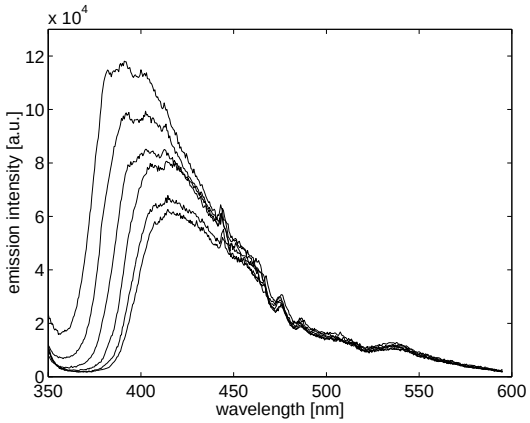

Fig. B.2: Emission spectra of 7DPO6 in ethanol solution at different pressures, from left to right: 0.2, 0.5, 1.2, 1.9, 2.6, and 3.3 GPa.

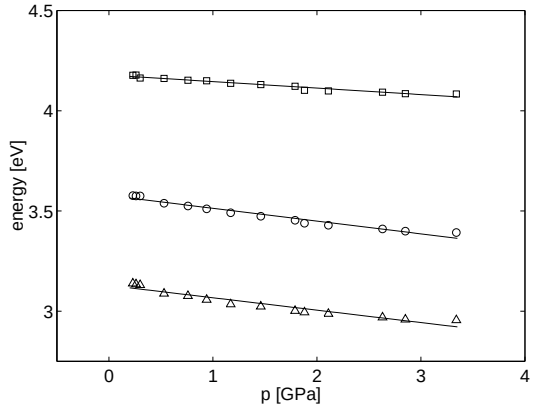

Fig. B.3: Energy shift of the nπ^* (□) and $\pi\pi^*$ (◯) absorption and emission bands (△) of 7DPO6 in ethanol solution as a function of pressure.

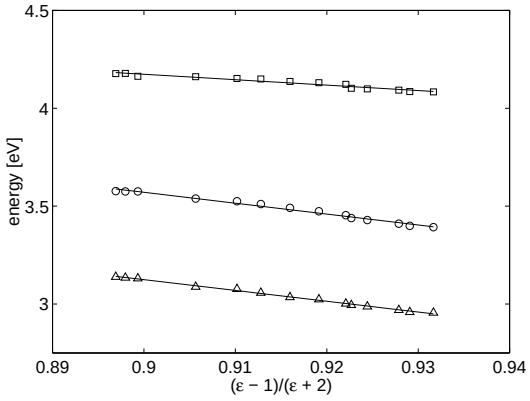

Fig. B.4: Energy shift of the nπ^* (□) and $\pi\pi^*$ (◯) absorption and emission bands (△) of 7DPO6 in ethanol solution as a function of the solvent polarity.

are no transport processes—those which can be influenced by variation of the viscosity [183].

Appendix C

Supplementary crystallographic data of the investigated and similar oxadiazole compounds

	Crystal system	Space group	Cell parameters (nm, °)	A*	Z†	ρ_{X-ray} (g/cm^3)	Packing motif	Ref.
DPO I	monoclinic	$P2_1/c$	$a = 0.55203(2)$ $b = 1.8143(6)$ $c = 1.2814(4)$ $\beta = 93.24(3)$	1/2	4	1.285	π-complexes, herring bone	[51]
DPO II	monoclinic	Cc	$a = 2.41334(4)$ $b = 2.4099(3)$ $c = 1.2879(2)$ $\beta = 110.048(3)$	6	24	1.259	π-complexes, stacks, layers	[48]
6DPO6 I	orthorhombic	$Pbca$	$a = 1.34694(2)$ $b = 0.79683(10)$ $c = 2.28927(10)$	1	8	1.364	herring bone	[49]
6DPO6 II	orthorhombic	$Cmcm$	$a = 1.6330(4)$ $b = 1.2307(2)$ $c = 0.6998(1)$	1/2 + 1‡	2+4§	1.362	rows, layers	[50]
6DPO4	monoclinic	$P2_1/c$	$a = 1.10287(7)$ $b = 1.26293(8)$ $c = 1.03608(6)$ $\beta = 113.5330(10)$	1	4	1.342	π-complexes, stacks	[47]
7PO3	monoclinic	$P2_1/c$	$a = 1.02997(6)$ $b = 0.64840(4)$ $c = 1.58117(10$ $\beta = 99.4820(10)$	1	4	1.296	π-complexes, layers	[45]

Tab. C.1: Crystallographic data of the investigated oxadiazole compounds. *Number of molecules per asymmetric unit. †Number of molecules per unit cell. ‡1/2 6DPO6 molecule and 1 water molecule. §2 6DPO6 molecules and 4 water molecules

	Crystal system	Space group	Cell parameters (nm, °)	A*	Z†	ρ_{X-ray} (g/cm^3)	Packing motif	Ref.
3DPO3	monoclinic	$C2/c$	$a = 1.1404(2)$ $b = 1.1751(2)$ $c = 1.08700(10)$ $\beta = 116.62(5)$	1/2	4	1.277	π-complexes, stacks	[65]
5DPO5 I	orthorhombic	$Pbcn$	$a = 0.47350(10)$ $b = 1.2516(2)$ $c = 2.6480(3)$	1/2	4	1.432	π-complexes, herring bone	[64]
5DPO5 II	orthorhombic	$Cmc2_1$	$a = 3.6708(4)$ $b = 0.69740(10)$ $c = 0.60300(10)$	1/2	4	1.456	layers, zig-zag	[66]
1DPO1	orthorhombic	$Pbcn$	$a = 0.54480(10)$ $b = 1.27580(10)$ $c = 1.97200(10)$	1/2	4	1.513	π-complexes, herring bone	[63]
7DPO7	monoclinic	$P2_1/c$	$a = 1.8097(4)$ $b = 0.7327(2)$ $c = 1.2325(3)$ $\beta = 99.620(5)$	1	4	1.172	zig-zag	[180]

Tab. C.2: Crystallographic data of other oxadiazole compounds. *Number of molecules per asymmetric unit. †Number of molecules per unit cell.

	Torsion angle* (°)					Dihedral angle (°)		Bond length† (nm)				Ref.
	R_1-ph_1	ph_1	oxa	ph_2	ph_2-R_2	ph_1-oxa	oxa-ph_2	R_1-ph_1	ph_1-oxa	oxa-ph_2	ph_2-R_2	
DPO I	–	1	1	1	–	2	2	–	0.1444(4)	0.1459(4)	–	[51]
DPO II‡	–	2	1	2	–	6	-6	–	0.1462	0.1462	–	[48]
6DPO6 I	1	1	0	1	0	15	-14	0.1399(2)	0.1461(2)	0.1462(2)	0.1387(2)	[49]
6DPO6 II	–	–	–	–	–	–	–	0.1409(10)	0.1442(12)	0.1442(12)	0.1409(10)	[50]
6DPO4	1	1	0	0	3	0	5	0.1385(3)	0.1447(3)	0.1449(3)	0.1371(2)	[47]
7PO3§	4	1	0	–	1	2	–	0.1376(2)	0.1451(2)	–	0.1468(3)	[45]

Tab. C.3: Molecular conformation data of the investigated oxadiazole compounds. *The torsion angle between four points—in our case, atoms—is the dihedral angle between the plane containing the first, second and third points and the plane containing the second, third and fourth points. †Bond distances are always accompanied by their standard deviation in brackets. The standard deviation indicates the significance of the last decimal figure. 90% of the bond distances are included in the values which result from the variation of the given value in an amount equivalent to its standard deviation. The origin of this deviation lies in part in the experimental error of the measurement and in part in the structure determination analysis. To cover a probability of 99% for the bond distances, the standard deviation should be multiplied by 3. ‡The values for DPO II are the mean values obtained for the six molecules of the asymmetric unit. §As 7PO3 does not posses the second phenyl ring, the values concerning to the torsion angle and bond length between the oxadiazole ring and the $N(CH_3)_2$ group are placed in the columns ph_2-R_2.

	Torsion angle* (°)					Dihedral angle (°)		Bond length† (nm)				Ref.
	R_1-ph_1	ph_1	oxa	ph_2	ph_2-R_2	ph_1-oxa	oxa-ph_2	R_1-ph_1	ph_1-oxa	oxa-ph_2	ph_2-R_2	
3DPO3	2	1	0	1	2	9	-9	0.1500(4)	0.1454(4)	0.1454(4)	0.1500(4)	[65]
5DPO5 I	3	1	0	1	3	4	-4	0.1479(10)	0.1464(10)	0.1464(10)	0.1479(10)	[64]
5DPO5 II	4	1	0	1	4	9	9	0.1477(4)	0.1457(4)	0.1457(4)	0.1477(4)	[66]
1DPO1	13	2	0	2	13	10	-10	0.1426(10)	0.1461(12)	0.1461(12)	0.1426(10)	[63]
7DPO7	4	0	0	1	1	7	18	0.1371(3)	0.1437(3)	0.1452(2)	0.1372(2)	[180]

Tab. C.4: Molecular conformation data of other oxadiazole compounds. *The torsion angle between four points—in our case, atoms—is the dihedral angle between the plane containing the first, second and third points and the plane containing the second, third and fourth points. †Bond distances are always accompanied by their standard deviation in brackets. The standard deviation indicates the significance of the last decimal figure. The 90% of the bond distances are included in the values which result from the variation of the given value in an amount equivalent to its standard deviation. The origin of this deviation lies in part in the experimental error of the measurement and in part in the structure determination analysis. To cover a probability of 99% for the bond distances, the standard deviation should be multiplied by 3.

	Atoms involved	Type of interaction	Inter-atomic distance (nm)*	Ref.
DPO I	whole molecules within a stack	π-π	0.344	
	C(ph)-C(ph) of adjacent stacks along b	van der Waals	0.321	
	C(ph)-N(oxa) of adjacent stacks along c	weak H-bond	0.342 (0.273; 124°)	[51]
DPO II	whole molecules within a stack	π-π	0.338†; 0.355‡	
	C(ph)-C(ph) of adjacent stacks of the same layer	van der Waals	0.383	
	C(ph)-N(oxa) of adjacent layers along c	weak H-bond	0.345 (0.267; 143°)	[48]
6DPO6 I	oxadiazole rings within a stack	π-π	0.325	
	C(ph)-C(ph) of adjacent stacks along a	van der Waals	0.363	
	$N(NH_2)$-N(oxa) of adjacent stacks along c	weak H-bond	0.341 (0.218; 168°)	[49]
6DPO6 II	$N(NH_2)$-$O(H_2O)$ within a row	H-bond	0.300 (0.187; 176°)	
	C(ph)-N(oxa) of adjacent layers along c	van der Waals	0.352	
	C(ph)-C(ph) of adjacent layers along c	van der Waals	0.355	[50]
	$N(NH_2)$-N(oxa) of adjacent layers along c	weak H-bond	0.313 (0.216; 159°)	
6DPO4	whole molecules within a stack	π-π	0.348	
	$C(OCH_3)$-N(oxa) of adjacent stacks along b	van der Waals	0.385	
	C(ph)-$O(OCH_3)$ of adjacent stacks along a	van der Waals	0.364	[47]
7PO3	whole molecules of a pair	π-π	0.347	[45]
	$C(CH_3)$-$N(NH_2)$ of adjacent layers along a	van der Waals	0.360	

Tab. C.5: Characteristics of the inter-molecular interactions in the investigated crystals. When referring to interacting atoms, no H atoms are considered, except when dealing with H-bonds. *When dealing with H-bonds the H-bond distance and the H-bond angle are indicated in parentheses. ‡Molecules with the same orientation. ‡Molecules with the opposite orientation.

.

	Atoms involved	Type of interaction	Inter-atomic distance (nm)*	Ref.
3DPO3	whole molecules within a stack	π-π	0.371	
	C(ph)-N(oxa) of adjacent stacks along a	van der Waals	0.350	
	$C(CH_3)$-$C(CH_3)$ of adjacent stacks along b	van der Waals	0.390	[65]
5DPO5 I	whole molecules within a stack	π-π	0.333	
	C(ph)-N(oxa) of adjacent stacks along b	weak H-bond	0.335 (0.265; 133°)	
	$C(COOCH_3)$-$O(COOCH_3)$ of adjacent layers along c	weak H-bond	0.328 (0.285; 109°)	[64]
	$C(COOCH_3)$-$O(COOCH_3)$ of adjacent layers along c	weak H-bond	0.369 (0.291; 140°)	
5DPO5 II	O(oxa)-N(oxa) within a layer	van der Waals	0.329	
	$CH_3(COOCH_3)$-$O(COOCH_3)$ within a layer†	weak H-bond	0.359 (0.285; 140°)	
	$CH_3(COOCH_3)$-$O(COOCH_3)$ within a layer‡	weak H-bond	0.356 (0.281; 132°)	[66]
	$CH_3(COOCH_3)$-$O(COOCH_3)$ of adjacent layers along a	weak H-bond	0.317 (0.281; 106°)	
1DPO1	whole molecules within a stack	π-π	0.353	
	$O(NO_2)$-$O(NO_2)$ of adjacent stacks along c	van der Waals	0.312	
	C(ph)-$O(NO_2)$ of adjacent stacks along b	weak H-bond	0.330 (0.240; 162°)	[67]
	C(ph)-N(oxa) of adjacent stacks along b	weak H-bond	0.341 (0.274; 130°)	
7DPO7	C(ph)-$N(N(CH_3)_2)$	van der Waals	0.355	
	C(ph)-$N(N(CH_3)_2)$	weak H-bond	0.357 (0.278; 136°)	[180]

Tab. C.6: Characteristics of the inter-molecular interactions in some similar oxadiazole crystals. For caption see table C.5.

.

Appendix D

Supplementary data of lattice parameters under compression

p(GPa)	a/a_0	b/b_0	c/c_0	β/β_0
0.0	1.000	1.000	1.000	1.000
0.0	1.001	1.001	1.000	0.999
0.1	1.004	0.994	0.994	1.001
0.1	1.002	0.991	0.992	1.002
0.2	1.001	0.988	0.988	1.001
0.4	0.995	0.975	0.980	1.003
0.6	0.988	0.966	0.976	1.004
0.7	0.990	0.958	0.971	1.003
0.9	0.987	0.953	0.968	1.003
1.1	0.983	0.950	0.965	1.004
1.2	0.980	0.948	0.963	1.004
1.3	0.983	0.945	0.961	1.006
1.6	0.976	0.941	0.957	1.006
1.8	0.972	0.937	0.954	1.005
2.0	0.970	0.933	0.952	1.005
2.1	0.967	0.929	0.950	1.004
2.3	0.965	0.926	0.947	1.004
2.5	0.962	0.924	0.945	1.004
2.7	0.960	0.922	0.943	1.004
2.9	0.958	0.918	0.941	1.004
3.1	0.955	0.915	0.939	1.002
3.3	0.954	0.911	0.937	1.001
3.5	0.951	0.909	0.935	1.000
3.7	0.949	0.906	0.933	0.999
3.9	0.947	0.904	0.932	1.000
4.1	0.944	0.901	0.931	0.999
4.3	0.942	0.900	0.929	0.998
4.4	0.940	0.897	0.928	0.998
4.6	0.939	0.895	0.927	0.998
4.8	0.936	0.893	0.926	0.998

Tab. D.1: High pressure lattice parameters of DPO I.

p(GPa)	a/a_0	b/b_0	c/c_0	β/β_0
0.0	1.000	1.000	1.000	1.000
0.2	0.994	0.996	0.995	1.004
0.3	0.992	0.990	0.991	1.008
0.5	0.991	0.984	0.989	1.014
0.7	0.988	0.977	0.986	1.019
1.0	0.985	0.973	0.984	1.023
1.2	0.981	0.967	0.980	1.028
1.3	0.978	0.960	0.978	1.033
1.5	0.977	0.956	0.980	1.038
1.8	0.976	0.952	0.980	1.041
1.9	0.977	0.949	0.978	1.043
2.2	0.976	0.946	0.976	1.044
2.4	0.976	0.938	0.971	1.044
2.8	0.973	0.934	0.967	1.044
3.1	0.971	0.929	0.960	1.040
3.3	0.972	0.922	0.957	1.043
3.5	0.972	0.923	0.958	1.044
3.7	0.972	0.922	0.957	1.045
3.8	0.968	0.920	0.953	1.045
4.1	0.967	0.917	0.950	1.044
4.2	0.966	0.915	0.946	1.043
4.6	0.965	0.913	0.942	1.044
4.8	0.963	0.912	0.942	1.044
4.9	0.963	0.908	0.944	1.046

Tab. D.2: High pressure lattice parameters of DPO II.

p(GPa)	a/a_0	b/b_0	c/c_0
0.0	1.000	1.00	1.000
0.1	0.998	0.991	0.996
0.2	0.998	0.980	0.991
0.4	0.992	0.969	0.986
0.6	0.986	0.961	0.979
0.9	0.978	0.951	0.974
1.1	0.970	0.942	0.972
1.3	0.963	0.934	0.972
1.5	0.957	0.927	0.970
1.8	0.953	0.921	0.968
2.2	0.946	0.914	0.965
2.5	0.942	0.913	0.963
2.6	0.939	0.911	0.962
2.8	0.936	0.910	0.961
2.9	0.934	0.910	0.961
3.2	0.931	0.911	0.960
3.5	0.931	0.908	0.959
3.7	0.928	0.896	0.959
4.0	0.929	0.894	0.959
4.2	0.927	0.886	0.960
4.5	0.927	0.875	0.960
4.7	0.928	0.870	0.955
4.9	0.926	0.860	0.958

Tab. D.3: High pressure lattice parameters of 6DPO6 I.

p(GPa)	a/a_0	b/b_0	c/c_0
0.0	1.000	1.000	1.000
0.4	0.976	1.003	0.989
1.0	1.001	0.973	0.969
1.5	1.000	0.965	0.952
1.8	1.001	0.963	0.942
2.3	1.001	0.953	0.932
2.8	0.999	0.948	0.924
3.3	0.861	1.000	0.942
3.9	0.997	0.932	0.910
4.4	0.833	0.994	0.925

Tab. D.4: High pressure lattice parameters of 6DPO6 II.

p(GPa)	a/a_0	b/b_0	c/c_0	β/β_0
0.0	1.000	1.000	1.000	1.000
0.1	0.991	0.994	0.991	0.999
0.3	0.961	0.986	0.968	0.993
0.9	0.906	0.963	0.945	0.984
1.4	0.874	0.951	0.928	0.981
1.8	0.853	0.944	0.915	0.978
2.1	0.838	0.939	0.906	0.973
2.9	0.816	0.927	0.896	0.966
3.5	0.796	0.923	0.882	0.960
4.1	0.780	0.919	0.871	0.959

Tab. D.5: High pressure lattice parameters of 7PO3.

Appendix E

Supplementary data of lattice parameters under heating

T(K)	a/a_0	b/b_0	c/c_0
293	1.000	1.000	1.000
303	1.004	0.999	0.998
333	1.003	1.002	0.999
363	1.004	1.006	1.000
393	1.004	1.010	1.000
423	1.005	1.014	1.001
453	1.005	1.020	1.000
483	1.006	1.024	1.001

Tab. E.1: High temperature lattice parameters of 6DPO6 I.

T(K)	a/a_0	b/b_0	c/c_0	β/β_0
293	1.000	1.000	1.000	1.000
300	1.005	0.993	1.004	0.994
320	1.006	0.990	1.009	0.994
340	1.011	0.988	1.015	0.992
360	1.014	0.988	1.019	0.994
380	1.017	0.988	1.022	0.998
400	1.020	0.987	1.023	0.998
420	1.023	0.983	1.028	1.001
440	1.029	0.984	1.034	1.003

Tab. E.2: High temperature lattice parameters of 6DPO4.

T(K)	a/a_0	b/b_0	c/c_0	β/β_0
293	1.000	1.000	1.000	1.000
303	1.001	0.999	1.001	1.000
323	0.999	1.003	1.002	1.000
343	1.004	1.001	1.004	1.002
363	1.003	1.002	1.010	1.001
383	1.003	1.001	1.011	1.001

Tab. E.3: High temperature lattice parameters of 7PO3.

Appendix F

Supplementary data concerning optical properties

R_1	R_2	$\lambda^{abs}_{\pi\pi^*}$ (nm)	$\lambda^{lum}_{\pi\pi^*}$ (nm)
H	H	284	365
H	OCH_3	298	360; 365
H	$N(CH_3)_2$	335	395
OCH_3	OCH_3	300	355; 370
OCH_3	$N(CH_3)_2$	335	390
$N(CH_3)_2$	$N(CH_3)_2$	350	400
H	$COOCH_3$	300	365
$COOCH_3$	$COOCH_3$	300	360
H	COCl	312	375
COCl	COCl	315	395
H	NO_2	317	–
NO_2	NO_2	320	–
H	SO_2CHF_2	300	weak
NO_2	SO_2CHF_2	310	–
OCH_3	$COOCH_3$	310	380
OCH_3	COOH	315	387
OCH_3	COCl	330	415
OCH_3	3,4-$(CO_2)O$	338	440
OCH_3	NO_2	337	–
$N(CH_3)_2$	$COOCH_3$	297; 355	450
$N(CH_3)_2$	3,4-$(CO_2)O$	310; 360	500
$N(CH_3)_2$	NO_2	307; 390	565

Tab. F.1: Absorption and emission maxima of DPO derivatives in toluene solution. R_1 and R_2 correspond to fig. 1. The compounds which contain the NO_2 group show no fluorescence. From [129].

R_1	R_2	$\lambda^{abs}_{\pi\pi^*}$ (nm)	$\lambda^{lum}_{\pi\pi^*}$ (nm)
H	H	303	358
H	CN	306	369
H	COOH	305	367
H	$COOCH_3$	306	368
H	$CONH_2$	305	366
H	COPh	308	–
H	$COCH_3$	310	–
H	NO_2	320	–
NO_2	H	327	–
H	$CSNH_2$	312	–
NH_2	H	329	–
H	NH_2	340	449
H	$NHCOCH_3$	323	392

Tab. F.2: Absorption and emission maxima of PBO derivatives in 2-methyl-tetrahydrofuran solution. R_1 and R_2 correspond to fig. 6.1. From [134].

Appendix G

Supplementary data concerning optical properties under compression

p(GPa)	λ_{edge}^{abs} (nm)	E_{edge}^{abs} (eV)	λ_{max}^{lum} (nm)	E_{max}^{lum} (eV)
0.1	323	3.84	348	3.56
0.5	324	3.83	351	3.53
0.9	324	3.82	353	3.51
1.1	325	3.81	355	3.49
1.5	326	3.80	356	3.48
1.5	327	3.80	358	3.47
1.8	327	3.79	358	3.46
1.9	327	3.79	359	3.45
2.1	327	3.79	359	3.45
2.1	328	3.79	359	3.45
2.3	328	3.78	360	3.45
2.5	329	3.77	361	3.43
3.1	332	3.74	363	3.42
3.3	343	3.61	366	3.39
3.9	348	3.56	368	3.37
4.3	353	3.51	377	3.29
5.0	356	3.49	380	3.27
5.3	360	3.45	386	3.22
5.8	361	3.44	386	3.21
6.1	362	3.42	388	3.19
6.9	367	3.38	392	3.16
7.2	369	3.36	396	3.13
7.1	370	3.35	397	3.13

Tab. G.1: Wavelength and energy of the absorption at 70% of the maximum value and of the luminescence maximum of DPO I crystals at high pressure.

p(GPa)	λ_{edge}^{abs} (nm)	E_{edge}^{abs} (eV)	λ_{max}^{lum} (nm)	E_{max}^{lum} (eV)
0.3	317	3.91	350	3.54
0.6	322	3.85	356	3.49
1.0	325	3.82	361	3.44
1.4	327	3.79	366	3.40
2.0	329	3.77	371	3.34
2.4	329	3.77	374	3.32
2.8	331	3.75	376	3.30
3.0	332	3.74	378	3.28
3.1	333	3.72	380	3.27
3.6	336	3.69	383	3.24
4.2	337	3.68	387	3.20
4.5	339	3.66	389	3.19
5.0	340	3.65	391	3.17
5.4	341	3.64	394	3.15

Tab. G.2: Wavelength and energy of the absorption at 70% of the maximum value and of the luminescence maximum of DPO II crystals at high pressure.

p(GPa)	λ_{edge}^{abs} (nm)	E_{edge}^{abs} (eV)	λ_{max}^{lum} (nm)	E_{max}^{lum} (eV)
0.4	385	3.22	404	3.07
0.7	387	3.21	406	3.05
1.0	391	3.17	411	3.02
1.5	394	3.15	416	2.98
1.8	397	3.12	419	2.96
2.1	400	3.10	421	2.94
2.4	402	3.09	424	2.93
2.8	405	3.06	–	–
3.2	408	3.04	431	2.88
3.8	412	3.01	435	2.85
4.0	416	2.98	437	2.83
4.3	417	2.97	441	2.81
4.9	420	2.95	447	2.78
5.2	421	2.95	449	2.76
5.4	422	2.94	453	2.74

Tab. G.3: Wavelength and energy of the absorption at 70% of the maximum value and of the luminescence maximum of 6DPO6 I crystals at high pressure.

p(GPa)	λ_{edge}^{abs} (nm)	E_{edge}^{abs} (eV)	λ_{max}^{lum} (nm)	E_{max}^{lum} (eV)
0.4	367	3.38	433	2.87
0.2	367	3.38	432	2.87
0.5	368	3.37	434	2.86
0.7	368	3.37	434	2.86
0.8	369	3.36	436	2.85
0.9	369	3.36	436	2.84
1.1	369	3.36	439	2.83
1.3	369	3.36	438	2.83
1.6	370	3.35	441	2.81
1.9	372	3.34	442	2.80
2.0	373	3.32	443	2.80
2.3	374	3.31	444	2.79
2.5	376	3.30	446	2.78
2.7	378	3.28	449	2.76
3.2	379	3.27	450	2.76
3.4	381	3.26	453	2.74
4.3	385	3.22	459	2.70
5.0	389	3.19	467	2.66
5.7	390	3.18	470	2.64

Tab. G.4: Wavelength and energy of the absorption at 60% of the maximum value and of the luminescence maximum of 6DPO4 crystals at high pressure.

p(GPa)	λ_{edge}^{abs} (nm)	E_{edge}^{abs} (eV)	λ_{max}^{lum} (nm)	E_{max}^{lum} (eV)
0.2	355	3.49	397	3.12
0.4	355	3.49	399	3.11
0.6	356	3.48	403	3.08
0.7	357	3.47	404	3.07
0.9	358	3.46	405	3.06
1.0	358	3.46	406	3.05
1.2	359	3.45	410	3.02
1.5	360	3.45	413	3.01
1.6	361	3.44	415	2.99
1.9	362	3.43	418	2.97
2.1	363	3.42	421	2.95
2.3	363	3.41	423	2.93
2.6	365	3.40	426	2.91
2.9	365	3.39	429	2.89
3.1	366	3.39	432	2.87
3.3	367	3.38	432	2.87
3.6	368	3.37	435	2.85
4.0	369	3.36	437	2.84
4.3	370	3.35	439	2.82
4.8	371	3.34	441	2.81

Tab. G.5: Wavelength and energy of the absorption at 70% of the maximum value and of the luminescence maximum of 7PO3 crystals at high pressure.

p(GPa)	ε	$\lambda^{abs}_{n\pi^*}$ (nm)	$\lambda^{abs}_{\pi\pi^*}$ (nm)	$\lambda^{lum}_{\pi\pi^*}$ (nm)	$E^{abs}_{n\pi^*}$ (eV)	$E^{abs}_{\pi\pi^*}$ (eV)	$E^{lum}_{\pi\pi^*}$ (eV)
0.2	27.1	297	347	395	4.18	3.58	3.14
0.3	27.4	297	347	396	4.18	3.58	3.13
0.3	27.8	298	347	396	4.16	3.58	3.13
0.5	29.8	297	350	402	4.16	3.54	3.09
0.8	31.4	299	352	403	4.15	3.52	3.08
0.9	32.4	299	353	406	4.15	3.51	3.06
1.2	33.7	300	355	409	4.14	3.49	3.04
1.5	35.1	300	357	410	4.13	3.47	3.02
1.8	36.5	301	359	413	4.12	3.45	3.00
1.9	36.8	302	361	414	4.10	3.44	3.00
2.1	37.7	303	362	415	4.10	3.43	2.99
2.6	39.6	303	364	418	4.09	3.41	2.97
2.9	40.3	304	365	419	4.09	3.40	2.96
3.3	41.9	304	365	420	4.08	3.39	2.96

Tab. G.6: Wavelength and energy of the absorption and luminescence maxima of 7DPO6 in ethanol solution at high pressure.

Appendix H

Supplementary data of Raman modes at ambient pressure

Raman frequency (cm^{-1})						tentative assignement
DPO I	DPO II	6DPO6 I	6DPO6 II	6DPO4	7PO3	
–	–	–	–	–	948 w	alkyl-aryl substituted
–	–	–	–	–	957 m	oxadiazole deformation
962 vw(sh)	966 vw(sh)	–	960 w(sh)	963.8 w(sh)	–	phenyl(ene)
967w	967 w	967 m	966 m	967 m	969 vw	CH out-of-plane
–	–	972 w(sh)	–	–	978 w	bending
–	–	–	987 w	984 vw(sh)	–	diaryl substituted
993 vs	992 s	993 s	996 s	994 vs	–	oxadiazole deformation
1005 w	1005 w	–	–	–	–	phenyl bending by sextants and breathing
1015 vw	–	1015 w	1016 w	1014 w	–	phenyl(ene) CH in-plane bending
–	–	–	–	–	1037 w	alkyl-aryl substituted
–	–	–	–	–	1046 vw	oxadiazole deformation
1452 m	1451 m	1443 m	1446 vw	1444 w	–	alkyl-aryl and diaryl substituted
1488 w	1488 w	1492 vw	1502 vw(sh)	1496 w(sh)	–	oxadiazole deformation;
–	–	1505 m	1506 w	1505 m	–	phenyl(ene)
–	–	–	–	–	1511 w	semi-circle stretching
–	1548 w(sh)	1544 vw(sh)	–	–	–	diaryl substituted
–	–	1560 w(sh)	1565 w(sh)	–	–	oxadiazole
1553 vs	1554 vs	1568 vs	1569 vs	1563 vs	–	deformation
–	–	–	–	–	1557 w	alkyl-aryl substituted oxadiazole deformation
1584 vw	1584 w	1580 m	1587 w(sh)	1583 m	–	phenyl(ene)
1591 w	1591 w	1590 s	1596 m	1599 m	1593 s	quadrant stretching
–	1598 vw(sh)	–	–	–	–	phenyl(ene)
1607 vs	1608 vs	1613 vs	1611 vs	1616 s	1614 vs	quadrant
1610 w(sh)	–	–	–	–	–	stretching
1628 w	1626 vw	1627 w	–	–	–	CH scissoring (?)

Tab. H.1: Most important Raman modes in the regions around 1000 cm^{-1} and between 1450 and 1650 cm^{-1}. The intensity of the lines is characterized as usually following the notation: very weak (vw), weak (w), medium (m), strong (s), and very strong (vs). Shoulders are marked with (sh).

Appendix I

Supplementary data of Raman modes under compression

p (GPa)	Raman frequencies (cm^{-1})																	
0.0	23	31	35	45	61	68	165	967	993	1005	1451	1487	1552	1583	1591	1606	1607	1628
0.3	24	32	36	46	62	70	167	967	994	1005	1451	1487	1553	1583	1591	1607	1607	1629
0.4	28	39	–	52	70	76	176	967	995	1006	1452	1488	1554	1584	1592	1608	1609	1632
0.6	29	41	–	54	71	76	179	968	996	1006	1453	1488	1555	1585	1593	1608	1609	1633
0.8	31	43	–	57	74	79	182	967	996	1007	1453	1488	1556	1585	1593	1609	1610	1634
0.9	32	43	47	59	77	83	185	967	997	1008	1454	1489	1556	1586	1594	1610	1611	1636
1.0	34	43	48	60	78	84	188	967	998	1008	1454	1489	1557	1586	1595	1611	1611	1637
1.2	35	44	51	62	81	86	191	968	999	1009	1455	1490	1558	1588	1595	1611	1613	1638
1.3	36	45	52	63	83	88	193	969	1000	1009	1456	1491	1559	–	1596	1612	1613	1638
1.4	36	45	53	64	84	89	194	968	999	1009	1456	1491	1559	1590	1596	1612	1614	1638
1.4	37	45	54	65	84	88	108	123	968	1000	1009	1456	1491	1560	1596	1612	1614	1641
1.6	37	46	55	65	85	89	108	125	969	1000	1009	1456	1491	1560	1597	1613	1614	1641
1.8	38	47	57	68	87	92	113	130	969	1001	1010	1457	1492	1561	1598	1614	1618	1642
1.9	39	47	58	68	87	92	114	131	970	1002	1010	1458	1493	1562	1598	1615	1619	1643
2.2	40	48	60	70	89	94	117	135	970	1003	1011	1458	1493	1563	1599	1616	1620	1645
2.5	41	49	61	71	91	95	119	138	970	1003	1011	1459	1494	1564	1600	1617	1621	1647
2.7	41	49	62	73	92	96	121	141	971	1004	1011	1460	1495	1565	1601	1617	1622	1648
2.9	42	50	63	74	92	97	122	143	971	1004	1012	1460	1495	1566	1601	1618	1622	1650
3.0	42	50	64	74	94	99	124	145	972	1005	1012	1461	1496	1567	1602	1619	1623	1650
3.2	43	51	65	76	95	100	125	147	971	1005	1012	1461	1496	1567	1602	1619	1624	1651
3.3	43	51	65	76	95	100	127	149	972	1005	1012	1461	1496	1567	1602	1620	1624	1651
3.6	43	52	66	77	97	102	129	152	972	1006	1012	1462	1497	1569	1603	1621	1625	1654
3.8	44	53	67	78	98	103	130	154	972	1007	1013	1463	1498	1569	1604	1621	1626	1653
4.0	44	54	68	79	99	105	133	156	973	1007	1013	1463	1498	1570	1604	1622	1627	1655
4.2	45	54	69	80	100	105	134	159	973	1008	1014	1464	1499	1571	1605	1623	1628	1657
4.5	45	55	69	81	101	106	136	161	973	1009	1014	1464	1499	1572	1606	1624	1629	1658
4.7	46	56	70	82	102	108	139	165	974	1009	1014	1465	1500	1573	1607	1625	1630	1659
4.9	46	57	70	82	102	107	139	166	974	1010	1014	1466	1501	1574	1608	1626	1631	1659
5.2	47	58	71	83	103	108	141	168	975	1010	1015	1466	1501	1574	1608	1626	1631	1660
5.4	47	59	71	84	106	112	143	171	975	1011	–	1467	1501	1575	1609	1627	1632	1661
5.6	48	60	72	84	107	112	145	172	975	1011	–	1467	1502	1576	1609	1627	1633	1662
5.8	48	60	72	85	107	112	145	174	975	1012	–	1468	1502	1577	1610	1628	1634	–
6.2	49	61	73	87	109	115	148	178	976	1013	–	1469	1503	1578	1611	1630	1636	–

Tab. I.1: Frequencies of selected Raman modes of DPO I at high pressure.

p (GPa)	Raman frequencies (cm^{-1})																		
0.0	16	–	31	45	59	70	95	–	155	967	993	1007	1453	1491	1557	1585	1593	1610	1627
0.2	16	–	30	45	59	69	81	–	155	967	993	1006	1451	1488	1554	1583	1591	1608	1624
0.3	17	–	36	50	60	78	102	–	162	967	994	1007	1451	1489	1556	1584	1592	1609	1628
0.2	16	–	31	46	59	70	95	–	155	967	993	1006	1452	1490	1556	1585	1592	1609	1627
0.4	17	–	35	49	62	71	85	–	159	967	993	1007	1452	1490	1556	1585	1592	1609	1627
0.6	18	–	39	52	64	75	87	–	163	968	994	1008	1454	1492	1559	1587	1595	1612	1630
0.4	18	–	37	51	64	75	84	–	162	968	994	1007	1454	1492	1558	1587	1595	1612	1631
0.6	18	–	40	53	66	76	90	103	164	968	995	1007	1454	1492	1559	1589	1595	1613	1633
0.8	20	32	43	56	69	77	93	–	167	968	995	1008	1455	1493	1561	1590	1596	1614	1634
1.0	20	33	45	59	71	80	96	106	171	968	996	1009	1456	1494	1561	1590	1597	1615	1634
1.2	21	35	47	61	73	81	100	105	174	969	997	1009	1457	1495	1563	1591	1598	1616	1636
1.4	22	37	49	63	76	82	105	112	178	970	998	1010	1457	1496	1564	–	1599	1617	1638
1.7	23	37	51	65	77	85	108	–	182	970	1000	1010	1458	1497	1565	–	1600	1619	1640
1.8	23	37	52	66	78	86	109	122	184	970	1000	1011	1459	1497	1566	–	1600	1619	–
2.0	24	39	55	69	–	85	113	127	187	971	1001	1012	1459	1497	1567	–	1600	1620	–
2.1	24	39	55	69	–	87	115	128	189	970	1001	1011	1460	1498	1568	–	1602	1619	–
2.2	25	39	56	70	–	87	116	128	191	971	1001	1012	1460	1499	1569	–	1602	1620	–
2.5	25	40	57	71	–	89	119	132	193	971	1003	1013	1461	1499	1570	–	1603	1621	–
2.7	25	41	59	72	–	90	–	133	195	972	1003	1013	1461	1499	1570	–	1603	1622	–
2.9	26	42	59	74	–	92	127	138	199	972	1004	1014	1462	1500	1572	–	1605	1623	–
3.0	26	43	60	75	–	92	128	139	199	972	1004	1016	1462	1500	1572	–	1605	1624	–
3.3	26	46	61	79	–	93	126	140	203	973	1006	1016	1463	1501	1573	–	1606	1626	–
3.6	27	44	62	81	–	96	130	143	206	973	1007	1019	1462	1501	1574	–	1607	1627	–
3.8	26	45	63	81	–	96	–	143	–	973	1007	1019	1463	1501	1575	–	1607	1627	–
3.9	27	46	63	82	–	97	–	145	–	973	1007	–	1464	1502	1575	–	1608	1628	–
4.0	27	45	66	82	–	99	–	146	–	973	1008	–	1463	1503	1576	–	1609	1629	–
4.3	27	47	69	84	–	101	–	148	–	974	1009	–	1464	1503	1577	–	1611	1630	–
4.6	27	46	69	84	–	101	–	151	–	974	1010	–	1465	1503	1578	–	1612	1630	–
4.7	28	50	70	85	–	104	–	151	–	975	1010	–	1465	1503	1579	–	–	1631	–
4.9	28	50	70	85	–	104	–	154	–	975	1011	–	1466	1503	1580	–	1612	1632	–
5.2	28	51	75	89	–	105	–	156	–	975	1012	–	1466	1504	1580	–	–	1632	–

Tab. I.2: Frequencies of selected Raman modes of DPO II at high pressure.

p (GPa)	Raman frequencies (cm^{-1})																
0.1	24	33	40	56	77	96	967	972	994	1015	1446	1507	1570	1582	1592	1614	1628
0.3	25	33	41	57	79	100	967	973	995	1016	1446	1507	1571	1582	1592	1613	1628
0.6	26	35	42	60	82	106	968	974	996	1017	1446	1507	1571	1583	1592	1614	1628
0.8	27	36	43	62	85	110	968	975	997	1018	1448	1508	1572	1583	1593	1614	1628
1.1	29	38	43	64	89	114	969	976	997	1018	1449	1509	1574	1584	1594	1614	1628
1.4	30	39	43	66	92	118	969	977	999	1019	1450	1509	1575	1585	1596	1613	1629
1.4	30	40	44	66	93	119	969	977	999	1019	1451	1510	1576	1586	1597	1614	1629
1.6	31	–	43	67	94	121	970	978	1000	1020	1451	1510	1577	1586	1597	1614	1629
2.0	33	–	44	69	97	124	970	979	1001	1021	1452	1511	1577	1586	1597	1614	1630
2.2	33	–	45	70	99	126	971	979	1001	1021	1452	1511	1577	1586	1597	1614	1631
2.5	35	–	46	72	102	128	971	980	1002	1022	1453	1512	1578	1587	1598	1615	1631
2.7	36	–	47	73	104	130	971	981	1003	1022	1454	1512	1580	1588	1600	1616	1632
2.8	36	–	48	73	105	131	972	981	1003	1022	1455	1513	1580	1589	1600	1615	1633
3.0	36	–	48	73	105	131	972	981	1004	1022	1456	1513	1582	1590	1601	1614	1633
3.3	42	–	50	75	108	134	972	982	1005	1023	1457	1514	1582	1590	1602	1614	1635
3.6	46	–	51	76	110	135	973	983	1006	1023	1458	1515	1583	1591	1603	1614	1636
3.9	43	–	52	77	110	137	973	983	1006	1023	1458	1515	1584	1592	1603	1615	1636
4.1	47	–	52	77	111	138	973	984	1007	1023	1459	1516	1585	1593	1604	1616	1638
4.3	46	–	53	78	114	140	974	984	1008	1023	1461	1516	1586	1594	1605	1616	1638
4.5	–	–	53	78	115	140	974	985	1008	1024	1461	1517	1587	1594	1606	1616	1639
5.2	–	–	55	80	116	141	974	985	1009	1024	1462	1517	1587	1595	1607	1617	1639
5.5	–	–	56	80	119	143	975	986	1009	1025	1463	1518	1589	1596	1608	1618	1640
5.6	–	–	58	81	121	143	975	986	1010	1025	1463	1518	1589	1596	1608	1616	1640
6.3	–	–	58	81	121	144	975	987	1010	1025	1463	1518	1589	1596	1608	1617	1640
7.6	–	–	60	82	123	146	976	988	1011	1025	1465	1520	–	1598	1610	1619	1640

Tab. I.3: Frequencies of selected Raman modes of 6DPO6 I at high pressure.

p (GPa)	Raman frequencies (cm^{-1})																		
0.1	–	–	74	80	92	109	115	137	–	151	167	966	990	998	1017	1450	1509	1572	1598	1614
0.3	–	–	76	82	95	111	117	140	–	156	171	966	989	999	1017	1450	1510	1573	1598	1614
0.4	–	71	79	85	98	113	120	145	–	161	176	966	991	1001	1017	1451	1510	1574	1599	1615
0.7	–	73	80	87	101	115	123	149	–	168	179	966	993	1002	1018	1452	1511	1575	1600	1616
1.0	–	74	82	90	107	118	126	156	–	174	187	967	995	1004	1019	1454	1512	1576	1602	1617
1.3	67	75	84	93	109	120	129	160	–	179	193	967	995	1006	1019	1455	1512	1577	1603	1618
1.6	–	78	85	95	112	123	132	166	178	185	198	967	996	1008	1020	1456	1513	1579	1604	1619
1.7	69	78	87	97	113	124	134	169	180	187	201	968	998	1009	1021	1456	1513	1579	1605	1619
2.1	72	81	89	99	115	127	137	172	183	199	209	968	998	1011	1022	1458	1515	1581	1606	1620
2.4	74	82	90	100	116	129	139	175	185	204	213	969	1000	1012	1023	1459	1515	1582	1607	1621
2.5	75	82	90	101	117	130	140	176	187	205	215	969	1000	1012	1023	1459	1516	1583	1608	1621
2.8	75	83	91	102	118	131	142	179	189	210	218	969	1000	1013	1024	1460	1516	1584	1609	1622
3.0	75	84	93	103	119	133	144	181	192	208	221	969	1000	1014	1025	1461	1517	1585	1609	1623
3.2	75	84	93	105	121	134	146	184	195	213	224	969	999	1014	1025	1462	1517	1585	1610	1623
3.5	76	85	94	105	123	136	147	184	196	215	227	970	1002	1015	1026	1462	1517	1586	1611	1624
3.7	76	85	94	106	122	137	148	184	197	219	229	970	1007	1015	1026	1463	1518	1587	1611	1625
4.1	76	86	96	109	124	139	151	185	201	221	232	970	1010	1016	1028	1464	1520	1588	1612	1626
4.3	76	88	97	110	125	140	153	187	204	226	234	971	1011	1017	1029	1465	1520	1589	1613	1627
4.9	76	87	97	112	127	141	154	–	207	227	237	971	1013	1017	1030	1466	1519	1590	1614	1628
5.2	76	88	97	114	129	143	155	–	211	233	–	972	1014	1018	1031	1466	1521	1591	1615	1629
5.6	76	89	97	115	130	144	156	–	213	241	–	972	1012	1018	1031	1467	1521	1592	1615	1630
5.6	76	88	96	117	134	145	154	–	216	240	–	972	1011	1018	1032	1468	1520	1594	1617	1631
6.0	76	–	97	115	129	142	154	–	211	242	–	973	1012	1018	1033	1469	–	1595	1618	1632
6.0	78	–	96	118	134	146	153	–	218	241	–	966	992	997	1016	1449	1509	1571	1597	1613

Tab. I.4: Frequencies of selected Raman modes of 6DPO6 II at high pressure.

p (GPa)	Raman frequencies (cm^{-1})								
0.3	963	966	992	1013	1505	1563	1583	1590	1616
0.1	962	966	992	1013	1505	1564	1584	1590	1617
0.2	963	966	993	1014	1505	1564	1584	1590	1617
0.4	961	965	998	1015	1505	1561	1586	1591	1618
0.9	962	966	1000	1019	1509	1566	1591	1596	1623
1.0	963	967	1001	1019	1510	1567	1591	1596	1623
1.2	963	967	1002	1020	1510	1567	1592	1597	1624
1.5	963	967	1002	1021	1510	1569	1594	1598	1625
1.6	963	968	1003	1022	1511	1570	1595	1599	1626
1.9	963	966	1003	1023	1512	1571	1596	1600	1627
2.0	964	966	1004	1023	1512	1572	1596	1601	1627
2.2	963	966	1003	1024	1512	1572	1596	1601	1628
2.5	964	967	1003	1025	1513	1574	1598	1602	1629
2.9	–	969	1004	1027	1515	1577	1599	1604	1631
3.1	–	969	1004	1028	1516	1578	1601	1605	1632
3.5	–	970	1005	1028	1517	1579	1601	1606	1633
3.9	–	971	1006	1030	1519	1582	1603	1608	1635
4.1	–	971	1006	1030	1519	1582	1604	1608	1635
4.3	–	972	1007	1031	1520	1583	1605	1609	1636
4.3	–	972	1007	1031	1519	1583	1605	1609	1636
4.6	–	972	1008	1032	1519	1583	1604	1609	1635
4.9	–	973	1008	1032	1519	1584	1605	1609	1636
5.3	–	973	1009	1033	1520	1585	1606	1610	1637

Tab. I.5: Frequencies of selected Raman modes of 6DPO4 at high pressure.

p (GPa)	Raman frequencies (cm^{-1})														
0.0	27	38	52	–	62	269	949	956	978	1046	1511	1557	1573	1592	1614
0.3	28	39	53	–	65	269	947	956	978	1046	1511	1557	1572	1592	1614
0.3	29	42	56	–	69	272	949	957	979	1048	1512	1558	1573	1593	1614
0.6	30	44	58	66	74	273	950	957	980	1049	1512	1559	1574	1594	1615
0.5	30	45	58	66	74	274	950	958	980	1049	1513	1559	1574	1594	1616
0.7	31	46	59	68	77	275	951	958	981	1050	1513	1560	1575	1595	1616
0.8	32	49	60	70	81	277	951	959	982	1051	1515	1561	1576	1596	1617
1.0	32	49	61	71	82	277	952	959	982	1052	1515	1561	1576	1596	1618
1.2	33	51	62	73	83	278	953	959	982	1052	1515	1562	1577	1597	1618
1.3	34	52	63	74	86	280	954	960	983	1053	1516	1563	1577	1597	1619
1.4	35	54	65	76	89	281	954	960	983	1054	1517	1564	1578	1598	1620
1.6	35	55	65	76	89	282	955	961	984	1054	1517	1564	1579	1599	1620
1.8	35	57	67	79	90	283	956	961	985	1056	1518	1565	1580	1600	1621
2.2	36	58	68	81	92	284	957	962	986	1057	1519	1566	1581	1601	1622
2.4	37	60	69	83	95	286	957	962	986	1057	1520	1567	1581	1602	1622
2.6	38	62	71	86	99	288	958	963	987	1059	1522	1569	1583	1603	1624
2.8	38	62	71	86	98	288	960	964	988	1059	1522	1569	1583	1604	1624
2.9	40	64	74	89	102	290	961	964	989	1060	1524	1570	1584	1605	1625
3.1	40	64	74	89	103	291	961	964	988	1060	1524	1571	1584	1605	1625
3.4	39	66	74	90	102	291	962	965	989	1061	1525	1571	1585	1607	1627
3.5	40	67	75	92	105	293	963	966	990	1063	1526	1573	1587	1608	1627
3.7	41	68	77	94	107	295	964	966	991	1063	1527	1574	1587	1609	1628
3.9	44	71	79	97	111	298	965	967	993	1065	1529	1576	1589	1611	1630
4.2	43	71	79	98	111	298	965	967	993	1065	1529	1576	1589	1612	1630
4.4	45	72	81	99	116	300	–	–	–	1066	1530	1577	1590	1613	1631
4.7	45	73	81	100	116	301	–	–	–	1067	1531	1578	1591	1614	1632
5.0	47	75	83	104	119	304	–	–	–	1068	1533	1580	1592	1616	1633
5.3	48	77	84	106	122	307	–	–	–	1069	1534	1581	1594	1617	1634
5.7	49	78	86	108	124	309	–	–	–	1070	1535	1583	1595	1619	1635
6.1	52	80	88	111	127	313	–	–	–	1072	1537	1584	1596	1621	1636

Tab. I.6: Frequencies of selected Raman modes of 7PO3 at high pressure.

ν_0 (cm^{-1})	dν/dp (cm^{-1}/GPa)	γ
23	8.1	2.64
31	5.4	1.30
35	14.8	3.11
45	12.6	2.08
61	13.4	1.63
68	12.4	1.34
88	13.1	1.10
165	19.5	0.87
967	1.6	0.01
993	3.1	0.02
1005	1.8	0.01
1452	2.9	0.02
1488	2.7	0.01
1553	4.3	0.02
1584	4.1	0.02
1591	3.3	0.02
1607	3.8	0.02
1610	4.8	0.02
1628	6.1	0.03

Tab. I.7: Frequencies at ambient pressure, their pressure derivatives and their mode-Grüneisen parameters of selected Raman modes of DPO I.

ν_0 (cm^{-1})	dν/dp (cm^{-1}/GPa)	γ
16	5.4	2.91
32	5.0	1.34
31	13.3	3.69
45	14.1	2.66
59	16.7	2.45
70	9.1	1.12
95	22.6	2.05
103	22.1	1.85
155	20.7	1.15
192	12.0	0.54
967	1.7	0.02
992	3.9	0.03
1005	3.3	0.03
1451	2.8	0.02
1488	3.0	0.02
1554	5.0	0.03
1584	6.6	0.04
1591	4.2	0.02
1608	4.7	0.03
1626	9.3	0.05

Tab. I.8: Frequencies at ambient pressure, their pressure derivatives and their mode-Grüneisen parameters of selected Raman modes of DPO II.

ν_0 (cm^{-1})	dν/dp (cm^{-1}/GPa)	γ
24	3.4	0.78
33	5.5	0.95
40	3.2	0.45
65	7.5	0.64
77	11.5	0.83
96	14.4	0.84
967	1.9	0.01
972	3.6	0.03
993	3.9	0.02
1015	2.7	0.02
1443	5.1	0.02
1505	1.9	0.01
1568	9.0	0.03
1580	3.7	0.01
1590	4.5	0.02
1613	4.5	0.02
1627	2.8	0.01

Tab. I.9: Frequencies at ambient pressure, their pressure derivatives and their mode-Grüneisen parameters of selected Raman modes of 6DPO6 I.

ν_0 (cm^{-1})	dν/dp (cm^{-1}/GPa)	γ
67	6.8	1.50
71	6.7	1.39
74	8.6	1.70
80	9.4	1.73
92	12.4	1.97
109	10.6	1.42
115	13.6	1.73
137	24.8	2.66
178	12.3	1.02
151	24.4	2.37
167	25.6	2.24
960	3.1	0.05
966	1.2	0.02
987	5.0	0.07
996	7.4	0.11
1016	2.9	0.04
1446	4.7	0.05
1506	3.3	0.03
1569	4.7	0.04
1596	4.4	0.04
1611	2.8	0.03

Tab. I.10: Frequencies at ambient pressure, their pressure derivatives and their mode-Grüneisen parameters of selected Raman modes of 6DPO6 II.

ν_0 (cm^{-1})	dν/dp (cm^{-1}/GPa)
964	0.7
967	0.2
994	6.0
1014	6.3
1444	4.3
1505	4.9
1563	5.7
1583	8.0
1599	7.0
1616	7.1

Tab. I.11: Frequency at ambient pressure and its pressure derivative of chosen Raman modes of 6DPO4. Due to the apparition of phase transitions, only internal modes are reported.

ν_0 (cm^{-1})	dν/dp (cm^{-1}/GPa)	γ
27	3.8	0.89
38	6.8	1.13
52	5.7	0.70
66	10.8	1.03
62	15.2	1.54
269	6.9	0.16
948	4.5	0.03
957	2.3	0.02
978	3.7	0.02
1046	4.3	0.03
1511	4.5	0.02
1557	4.7	0.02
1593	4.9	0.02
1614	3.9	0.02

Tab. I.12: Frequencies at ambient pressure, their pressure derivatives and their mode-Grüneisen parameters of selected Raman modes of 7PO3.

Selbständigkeitserklärung

Hiermit erkläre ich, die vorliegende Arbeit selbständig ohne fremde Hilfe verfaßt zu haben und nur die angegebene Literatur und Hilfsmittel verwendet zu haben. Überdies erkläre ich hiermit, daß diese Arbeit an keiner anderen Hochschule eingereicht worden ist.

Olga Franco González

15. April 2002